INFORMATION TO USERS

This manuscript has been reproduced from the microfilm master. UMI films the text directly from the original or copy submitted. Thus, some thesis and dissertation copies are in typewriter face, while others may be from any type of computer printer.

The quality of this reproduction is dependent upon the quality of the copy submitted. Broken or indistinct print, colored or poor quality illustrations and photographs, print bleedthrough, substandard margins, and improper alignment can adversely affect reproduction.

In the unlikely event that the author did not send UMI a complete manuscript and there are missing pages, these will be noted. Also, if unauthorized copyright material had to be removed, a note will indicate the deletion.

Oversize materials (e.g., maps, drawings, charts) are reproduced by sectioning the original, beginning at the upper left-hand corner and continuing from left to right in equal sections with small overlaps.

Photographs included in the original manuscript have been reproduced xerographically in this copy. Higher quality 6" x 9" black and white photographic prints are available for any photographs or illustrations appearing in this copy for an additional charge. Contact UMI directly to order.

Bell & Howell Information and Learning
300 North Zeeb Road, Ann Arbor, MI 48106-1346 USA
800-521-0600

UMI®

DISSERTATION

CHARACTERIZATION OF CADMIUM TELLURIDE GRAIN BOUNDARIES IN CADMIUM TELLURIDE/CADMIUM SULFIDE SOLAR CELLS

Submitted by

Lawrence M. Woods

Department Electrical and Computer Engineering

In partial fulfillment of the requirements for the

Degree of Doctor of Philosophy

Colorado State University

Fort Collins, Colorado

Fall 2000

COLORADO STATE UNIVERSITY

November 3, 2000

WE HEREBY RECOMMEND THAT THE DISSERTATION PREPARED UNDER OUR SUPERVISION BY LAWRENCE M. WOODS ENTITLED "CHARACTERIZATION OF CADMIUM TELLURIDE GRAIN BOUNDARIES IN CADMIUM TELLURIDE/CADMIUM SULFIDE SOLAR CELLS" BE ACCEPTED AS FULFILLING IN PART REQUIREMENTS FOR THE DEGREE OF DOCTOR OF PHILOSOPHY.

Committee on Graduate Work

Advisor

Department Head

ABSTRACT OF DISSERTATION

CHARACTERIZATION OF CADMIUM TELLURIDE GRAIN BOUNDARIES
IN CADMIUM TELLURIDE/CADMIUM SULFIDE SOLAR CELLS

The in-plane electrical properties of polycrystalline CdTe have been evaluated at various stages in the processing of CdTe/CdS solar cells. This was made feasible by a new lift-off technique, which separates the CdTe layer. In addition, the theory for electrical conduction across grain-boundaries has been extended in that an analytical solution was developed for both one-step and two-step, thermally-assisted tunneling mechanisms. When compared to other conduction mechanisms, it was found that the thermally-assisted tunneling conduction mechanisms gave the best fits to in-plane current versus temperature data for most of the lift-off CdTe samples herein. Values for the grain-boundary barrier height, the barrier height inhomogeneity, and the doping within the vicinity of the grain boundary were determined from the fits.

The $CdCl_2$ treatment was found to increase the hole grain-boundary barrier height by about 37%, and the doping in the vicinity of the grain boundary was found to increase by about 0.5 - 1 order of magnitude. Also shown was a non-uniform doping level in the grains all samples, with the doping near the grain boundary several orders of magnitude higher than the bulk concentration. The bulk concentration was determined from a high-frequency, in-plane impedance measurement. This information has allowed a detailed development of the grain-boundary band diagram, which predicts an electron, or minority-carrier barrier due to the variable p-type doping. This barrier may act to reflect

the minority carriers before the grain boundary, and reduce minority-carrier recombination.

It was also shown that the Nitric-Phosphoric (NP) etching reduces the grain-boundary barrier heights to a value that correlates with the valence-band offsets between CdTe and Te. This effect of the NP-etch on grain boundaries extends down a minimum of 2.5 μm from the etched back contact surface. The effects of the NP-etch are also shown to be unstable and could translate to severe increases in the back-contact series resistance of devices.

Finally, it was shown that there was no significant effect of the CdTe source plate usage on the in-plane electrical properties, and that there is no indication of any grain-boundary barrier height inhomogeneity in any of the samples.

Lawrence M. Woods
Dept. of Electrical and Computer Engineering
Colorado State University
Fort Collins, Colorado
Fall 2000

ACKNOWLEDGEMENTS

I would like to thank Dr. Dean Levi and Dr. Gary Robinson for their technical support and guidance through the drawn out time period of this dissertation. In addition, their unwavering willingness to help me finish, and support through out new and unfamiliar working arrangements, is greatly appreciated. This latter support was crucial for assuring completion of this dissertation. I am especially grateful to Dean for his many proof readings of the manuscript, additional moral support, and friendship.

I would also like to acknowledge my wife, Lisa, for "sticking it out" with me, and who has had to live with this since we have been together. The additional responsibilities she undertook, and the moral support she provided was also crucial to the completion of this dissertation. I don't know if I could ever properly thank her.

Lawrence Woods

November 6, 2000

"Characterization of CdTe Grain Boundaries in CdTe/CdS Solar Cells"

Table of Contents

Page

Chapter 1

INTRODUCTION

This dissertation is ultimately about improving the current state of the art of solar cells. Herein, the understanding of one particular technology will be extended, so that one day it may be cost competitive with non-renewable resources for generation of terrestrial electric power. This is not a new goal, as researchers have been pursuing this goal for over 40 years after the first solar cell with a reasonable efficiency was produced.[1] However, at this time, as we start the new millennium, it appears as if this goal is more tangible than ever. Several private companies (albeit mostly owned by gas and oil companies) are currently making a profit by manufacturing solar panels for third world countries that have no national infrastructure for providing electrical power. Thus, solar panels are already cost effective in these countries. Additionally, aside from the ever looming threat of gas and oil depletion,[2] there is pressure on industrialized nations to curtail the emissions from the burning of fossil fuels. These emissions are believed to contribute to global warming. Recently, governments around the world have responded by encouraging renewable energy through government sponsored programs and tax breaks.[3] The sum of the above has resulted in over 30% annual growth in the worldwide sales of solar cell power for the last couple of years.[4] Currently, companies are building larger manufacturing plants, which should result in lower priced solar cells due to the economy of scale. This fact, combined with emergence of companies producing thin film

solar cells, which have potential for high efficiency yet low manufacturing costs, give new hope that solar cells may soon be cost competitive everywhere.

1.1 Solar Cells

Solar cells produce electrical power by absorbing sunlight and are based on the photovoltaic effect originally observed by Becquerel in 1839.[5] In semiconductor devices, electron-hole pairs are generated from a quantum mechanical process that occurs when photons with energies greater than the bandgap of the semiconductor are absorbed in the device. These photo-generated charges are separated by the presence of a built-in electric field. This results in an electric current, which can be extracted by forming contacts with the device. The built-in electric field is created by forming a p-n junction in the material,[6] and is usually located within the area of photo-absorption.

Historically, the material most often used to make solar cells has been crystalline silicon, as it was the first material to achieve a high conversion efficiency in 1954.[1] The high conversion efficiency was achieved by breakthroughs in the purification of silicon material, by growing crystals using the Czochralski method, and by forming p-n junctions by high-temperature vapor diffusion.[7] However, crystalline silicon is relatively expensive to manufacture into solar cells. Also, it has an indirect bandgap and therefore requires the aid of phonons to create electron-hole pairs. Consequently, a thicker layer of material is needed to absorb all the sunlight. This increases the cost of the solar cell. Thus, there is an opportunity for lower cost materials and technologies to develop and enter the solar cell market. Some well known direct gap materials, such as GaAs or InP, can be much thinner due to the shorter absorption length, and have demonstrated efficiencies greater than 30%.[8] However, these devices are complicated, and the materials

are more expensive on a per unit weight basis.[9] However, these devices may prove cost effective in concentrator systems where less photovoltaic material is required. Other direct gap materials, such as thin-film, polycrystalline CdTe, polycrystalline $CuInGaSe_2$, and amorphous silicon, have recently achieved a level of technical maturity that has demonstrated highly efficient and stable devices.[10] The thin-film devices show promise for having the best cost versus efficiency trade-off for terrestrial and space applications when compared against crystalline Si, GaAs and InP. This has sent many solar cell manufactures into the production of solar cell modules based on thin-film, polycrystalline materials.

1.2 Thin-film Polycrystalline CdTe based Solar Cells

Thin-film solar cells, which work well in the polycrystalline form, have the advantage over their crystalline counterparts in that they can be deposited with cheaper techniques. CdTe-based devices have demonstrated this capability. In addition to its short absorption length and nearly ideal bandgap (1.5 eV) for solar energy conversion,[11] high efficiency devices have been grown from a variety of deposition techniques.[12] The best devices have achieved nearly 16% efficiency.[13] A cross-sectional schematic showing the different layers in a typical solar cell device is shown in Figure 1.1. The cell is made on a transparent glass superstrate. The first layer deposited is a transparent conducting oxide (TCO), which acts as the front (sun side) contact and is transparent to the solar spectrum. This is followed by a thin layer of CdS, which acts as the n-type material for the built in electric field and is also mostly transparent to the solar spectrum due to its large bandgap of 2.4 eV. Then the light-absorbing, unintentionally-doped, p-type CdTe is deposited at a thickness of 2-10 μm. Following the film depositions, a post deposition $CdCl_2$ heat

treatment is required for high efficiency devices. For small grained CdTe, the $CdCl_2$ heat treatment has been shown to increase the average grain size after treatment.[14] Additionally, it is thought to passivate grain boundaries.[15,16]

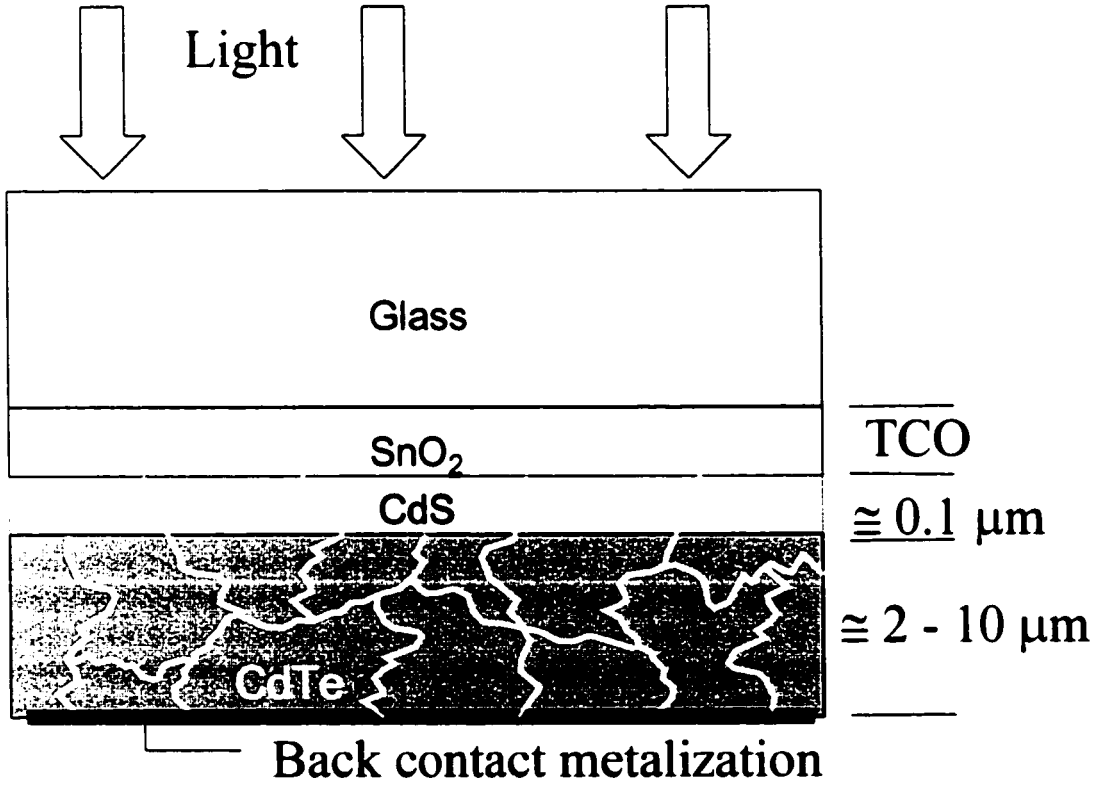

Figure 1.1 **CdTe/CdS solar cell device in cross-section showing the individual layers. White lines denote grain boundaries and the material polycrystallinity.**

The final layer to be applied is the back contact metalization. This final step is not trivial, as a Schottky barrier tunneling contact must be formed due to CdTe's high electron work function.[17] CdTe material suffers further in that it is a self-compensated material, meaning that it is difficult to introduce a high level of electrically active dopants into the material without the material counteracting with neutralizing defects. This effect is pronounced in polycrystalline material.[18,19] This fact, coupled with CdTe's high electron work function, makes it difficult to form Schottky barrier tunneling contacts

between p-type CdTe and the back contact metalization. However, this difficulty has been mostly overcome in recent years. The current standard practice is to use an etchant, which creates a tellurium-rich p+ CdTe layer, prior to the back contact metalization.[20,21] This step in the processing has proven that it contributes to the formation of stable, low resistance back contacts.

1.3 Grain Boundary Origins and Definition

Inherent in the thin film polycrystalline materials are grain boundaries, which form the interfaces between the individual crystallites. This is depicted in Figure 1.1 by the jagged lines criss-crossing the CdS and CdTe layers. Figure 1.2 shows the difference between fine-grained polycrystalline material, large-grained polycrystalline material, and columnar grains where the grain diameters are on the same order as the film thickness.

The grain boundaries form during the growth of the film and arise from misorientation of adjacent crystallites during the coalescence stages of growth. Fahrenbruch and Bube[22] have previously categorized the grain boundaries into three classes, which are paraphrased as follows:

(1) *Coherent twins.* These have negligible electrical activity.

(2) *Low-angle grain boundaries.* These include a net of edge dislocations accompanied by lattice strain fields. Electrical activity is moderate.

(3) *High-angle grain boundaries and incoherent twinning.* Includes high densities of dislocations, much lattice strain, and considerable impurity segregation. They show strong electrical activity.

The grain boundaries described in (2) and (3) above are a source of intra-gap defect states due to dangling bonds, impurity segregation, and/or an interruption in the periodicity of the lattice. A high density of intra-gap defect states, such as those from (3) above, can

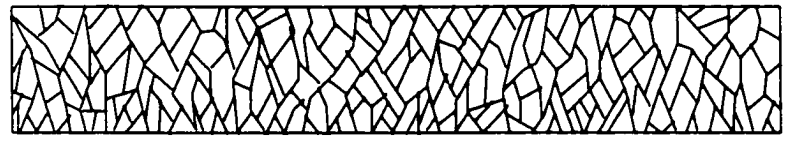

(a) Fine Grain Structure

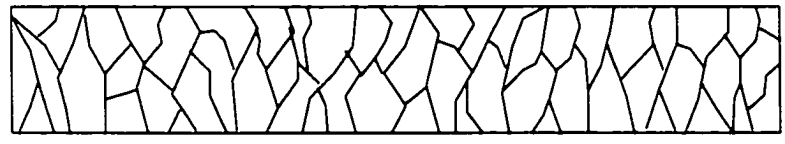

(b) Large Grain Structure

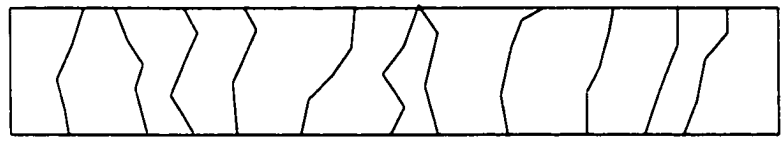

(c) Columnar Grain Structure

Figure 1.2 Polycrystalline Grain Types

"pin" the Fermi level local to the grain boundary. The energy at which the Fermi level gets pinned depends on the energy distribution of the intra-gap defect states, and the amount of charge transferred between these states and the bulk of the surrounding semiconductor. If the pinned Fermi level at the grain boundary is at a different energy than the Fermi level in the bulk of the grain, relative to the band edge, then this creates a potential energy barrier. Several types of grain boundary potential energy barriers are possible and are shown in the band diagrams of Figure 1.3 for a p-type material. The grain boundary states are depicted as short horizontal lines at the grain boundary in the

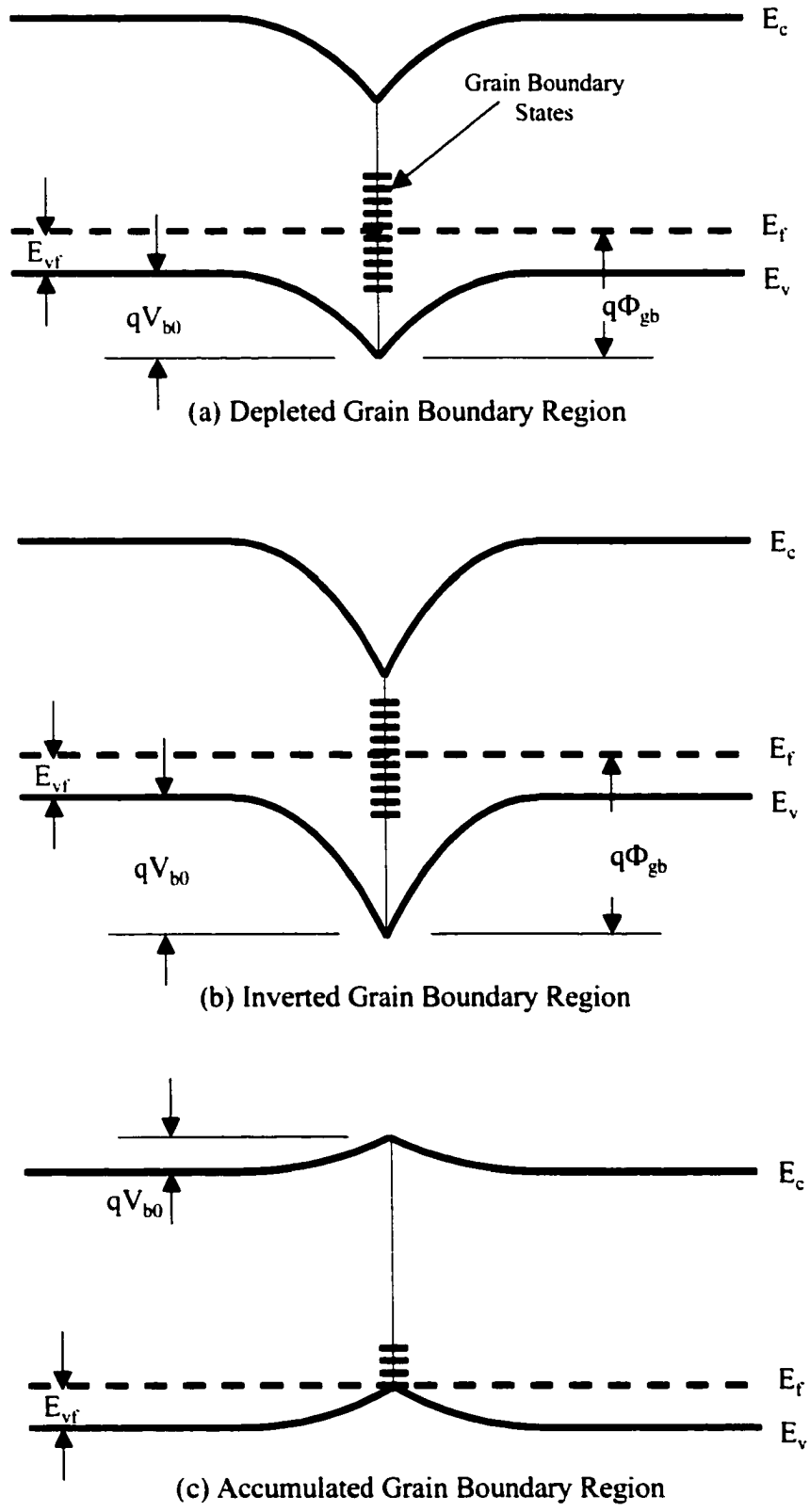

Figure 1.3 Types of Grain Boundary Potential Barriers.

figure. The areas adjacent to the grain boundary can be depleted, inverted or accumulated. In the figure, the difference between the band edge energy of the majority carrier in the bulk and at the grain boundary, is denoted as qV_{b0}, where q is the electron charge. The difference between the Fermi level energy in the bulk and the valence band edge energy in the bulk is E_{vf}. The sum of the two is:

$$q\Phi_{gb} = qV_{b0} + E_{vf} \quad \text{eV} \tag{1.1}$$

where $q\Phi_{gb}$ is the typical definition of barrier energy in the Schottky barrier literature. However, V_{b0} will be referred to as the zero-bias grain-boundary barrier potential throughout this dissertation. It is commonly believed that the grain boundaries in thin-film p-type polycrystalline CdTe, are of the depletion or slightly inverted type.[23] The grain sizes in polycrystalline CdTe solar cells vary with deposition technique, temperature, and substrate, but tend to be that of the large grain structure in Figure 1.2(b) with grain sizes in the 1-5 μm range. An example of the morphology of the CdTe used in these studies is evident in the image generated by a scanning electron microscope, and shown in Figure 1.4.

1.4 General Effects of Grain Boundaries on CdTe Devices

Exploiting CdS/CdTe solar cell devices to their fullest potential has been a technological struggle for several reasons. In addition to the back contact issues described earlier, the grain boundaries have debilitating effects on the processing and subsequent operation of CdS/CdTe solar cells. One effect is from defects and impurities, which tend to segregate toward these surfaces during high temperature processing, and therefore contribute to a variable doping level within the grains.[24,25] Also, the grain boundaries exhibit enhanced diffusion compared to the bulk.[26,27] This results in the

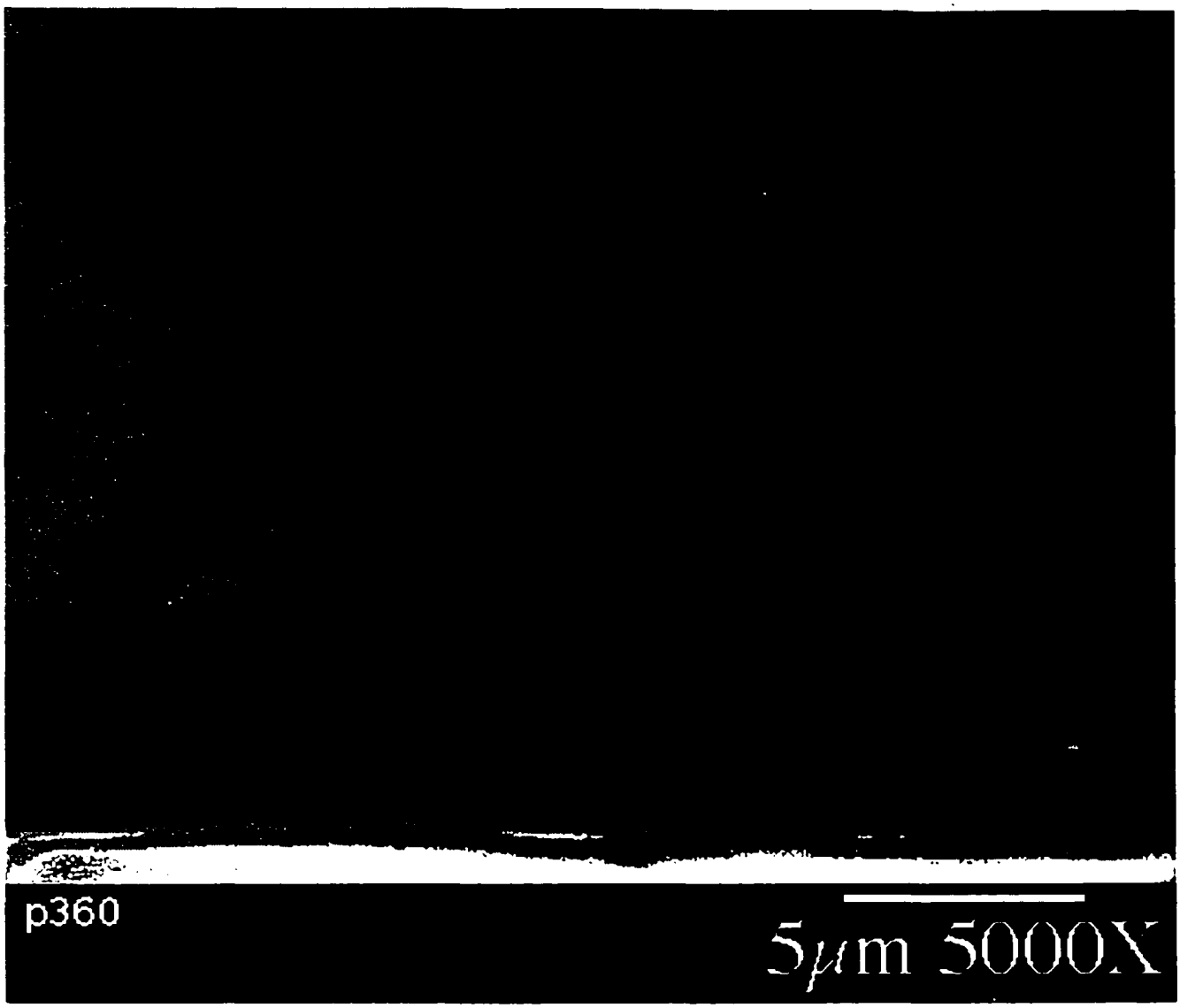

Figure 1.4 **SEM image of polycrystalline CdTe viewed at a 45° angle to the top and cross-sectional surfaces. CdTe deposited at the National Renewable Energy Laboratory.**

following problems: compromised spatial control of wet chemical etching, and penetration by impurities and atmospheric gases during processing and over time, which compromise the solar cell device stability.

The severity of the problems described above are greatly dependent on the size of the grains or number of grain boundaries. In thin films the grain diameter tends to be no

more than the film thickness, which also tends to be of the same order as the minority carrier diffusion length. Excess minority carriers within a diffusion length of the grain boundary depletion region, could get pulled into the grain boundary by the electric field and recombine. Thus, the grain boundaries can have detrimental effects on the minority carrier lifetime and ultimately the device performance. A decreased minority carrier lifetime would reduce the solar cell open-circuit voltage. If the grain boundary recombination occurred in the bulk of the device, before the light generated carriers had a chance to do any work, then this would result in a decreased short-circuit current. Grain boundaries within the junction depletion region would act as a source of junction recombination and consequently increase the diode ideality factor and/or reduce the cell fill-factor. The grain boundaries can also affect the carrier transport properties. If grain boundaries must be traversed to reach the contacts, then the grain boundary potential barriers act to increase the material resistance, which would result in increased solar cell series resistance. Solar cell shunt resistance can also be compromised if metallic impurities diffuse down the grain boundaries, and penetrate through the junction. Thus, every solar cell performance parameter is potentially affected by grain boundaries.

Several researchers have modeled the effects of grain boundaries on solar cell operation.[28,29,30] Lee and Gray[31] performed numerical modeling of two dimensional CdS/CdTe solar cells with grain boundaries perpendicular to the heterojunction plane and extend from the front junction to the back contact. In the modeling, no grain boundaries are in the direction normal to current flow, and the grain boundaries were modeled as a thin layer with a number of Shockley-Read-Hall (SRH) recombination centers to simulate the intra-gap defect levels. The effect of grain boundary defect density on the current-

voltage curves of illuminated solar cells is shown in Figure 1.5. The figure shows that short circuit current, I_{sc} (I @ V=0), open-circuit voltage, V_{oc} (V @ I=0), and the diode ideality factor, or sharpness of the knee in the curve, are all adversely affected by increasing grain boundary defect density.

Few CdS/CdTe solar cell device measurements have been correlated with grain boundaries. However, the effects of grain size and grain boundary passivation have been measured on other materials.[32,33] The effect of grain size on device efficiency is shown in Figure 1.6. for experimental polycrystalline thin film cells. Since larger grain sizes have a reduced surface-to-volume ratio, Figure 1.6 generally confirms the detrimental effects of grain boundaries.

1.5 Electrical Characterization Problems

Routine electrical characterization of thin film, polycrystalline CdTe device material is complicated by the presence of grain boundaries and the intrinsic nature of the CdTe due to self-compensation. Hall measurements are no longer routine. Intra-grain carrier concentrations and Hall mobility must be derived using electrical models of the polycrystallinity and known values for the following ratios: non-depleted grain size to grain boundary depletion width, grain boundary resistivity to intra-grain resistivity, and the grain boundary mobility to intra-grain mobility.[34,35] Furthermore, characterization of CdTe films not grown as devices may not be an accurate evaluation of device CdTe. It has been shown that diffusion of impurities up grain boundaries from the underlying films and substrate greatly affect the electrical properties of the CdTe film during growth and subsequent high temperature processing of a CdS/CdTe device.[36] Thus, the difficulty in characterization further inhibits device control, optimization and understanding.

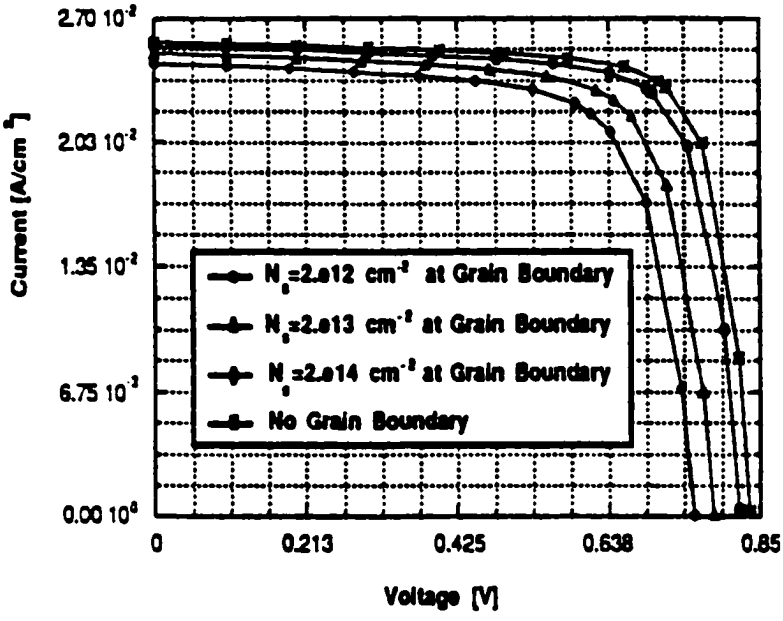

Figure 1.5 **Modeling results of illuminated CdTe solar cells showing the detrimental effects of grain boundary recombination on cell performance.[31]**

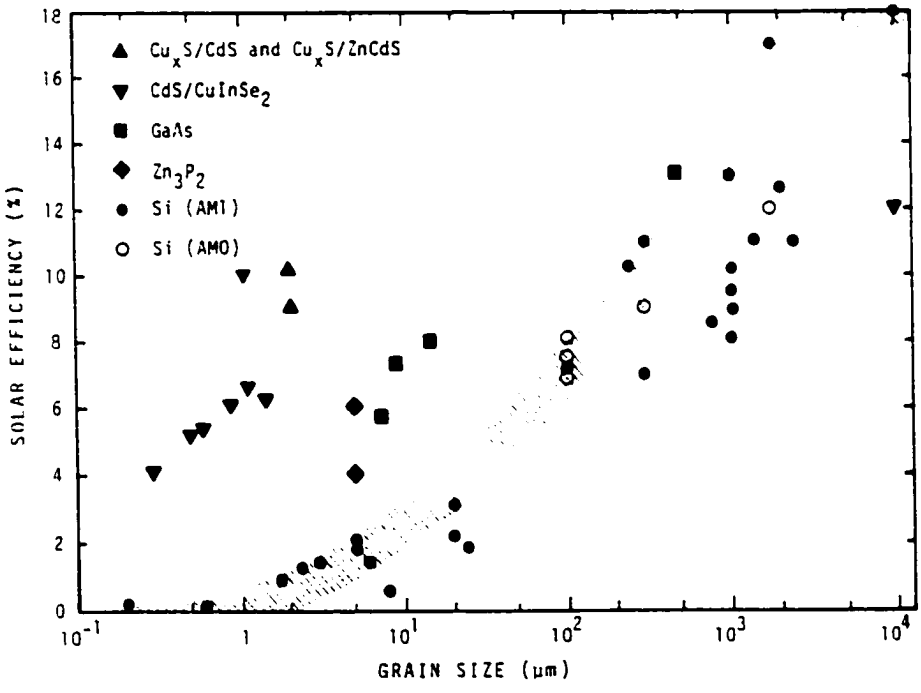

Figure 1.6 **Grain size versus device efficiency for experimental polycrystalline thin-film cells through 1981. The shaded area is the most probable relation for Si cells.[22]**

1.6 Optical Characterization

Optical thin film characterization techniques do not suffer from the complications or drawbacks that the standard electrical characterization techniques do. Optical methods such as photoluminescence (PL), and time-resolved photoluminescence (TRPL), have been used to study the effects of grain boundaries on excess carrier recombination and lifetime on solar cells. The effects can be separated into device junction influences and device bulk influences since the solar cells can be optically excited from either the front or back (no back contact). Ahrenkiel et al.[37] measured the effect of grain size on minority carrier lifetime on CdS/CdTe devices. Later TRPL measurements showed a relation between minority carrier lifetime and V_{oc}.[38] The effects of grain size on PL intensity and TRPL lifetime is shown in Figure 1.7. In these particular films, the large grain ($\approx$ 4 μm) material was adjacent to the CdS and the small grain material ($\approx$ 1-4 μm) was located at the back of the film. The film thicknesses were about 10 μm and the absorption length in CdTe is approximately 0.2 μm for 600 nm excitation. The PL intensity plot shows that the large grain material has a PL intensity that is an order of magnitude greater than that of the small grain material. This result indicates that the small grain material has a greater amount of non-radiative recombination due to the increased grain boundary states from an increased grain surface-to-volume ratio. Furthermore, the TRPL measurement shows a reduced lifetime for the small-grain film. This result reflects the fact that the photo-generated carriers are on average closer to non-radiative grain boundary sites in smaller grain material.

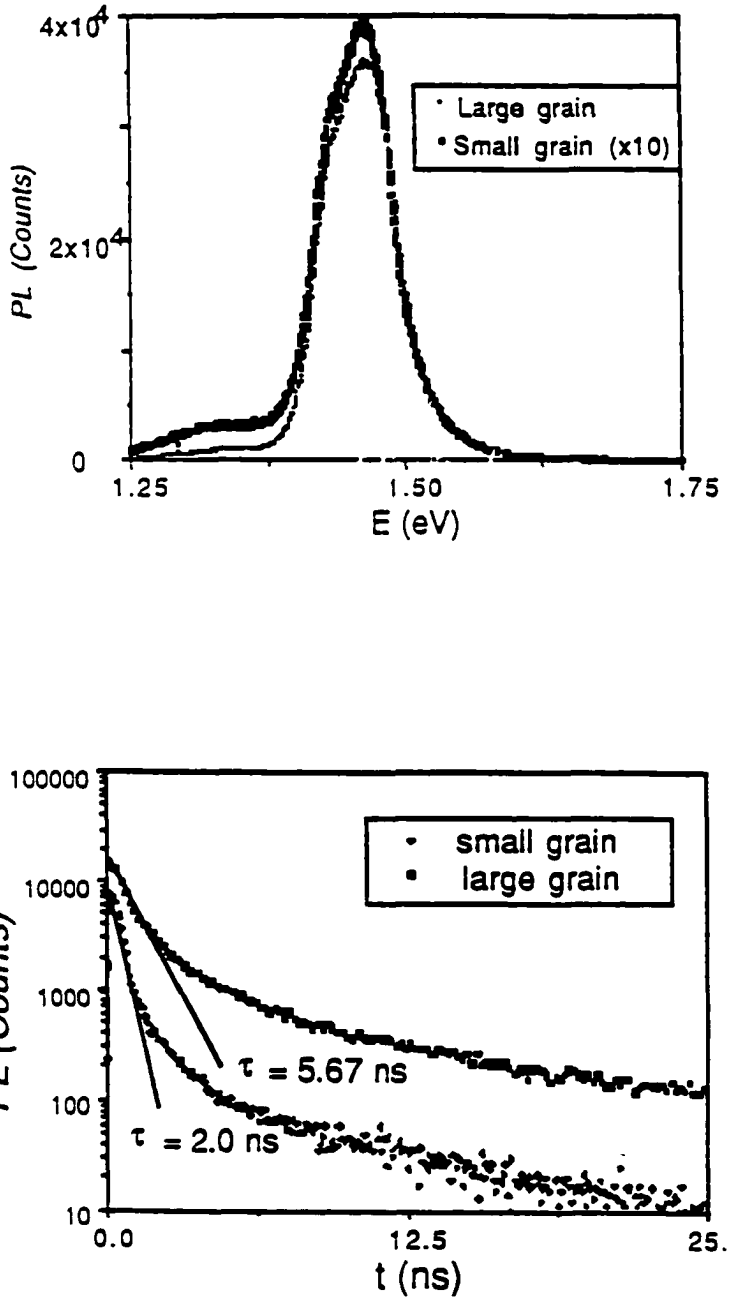

Figure 1.7 **Photoluminescence Intensity (top) and Time Resolved Photoluminescence Lifetime (bottom) dependence on grain size.**[37]

Other PL measurements by Levi and this author[39] demonstrated spectral changes in junction side photoluminescence due to the back contact nitric-phosphoric (NP) etch. The PL spectra for the NP-etched and non-etched samples are shown in Figure 1.8.

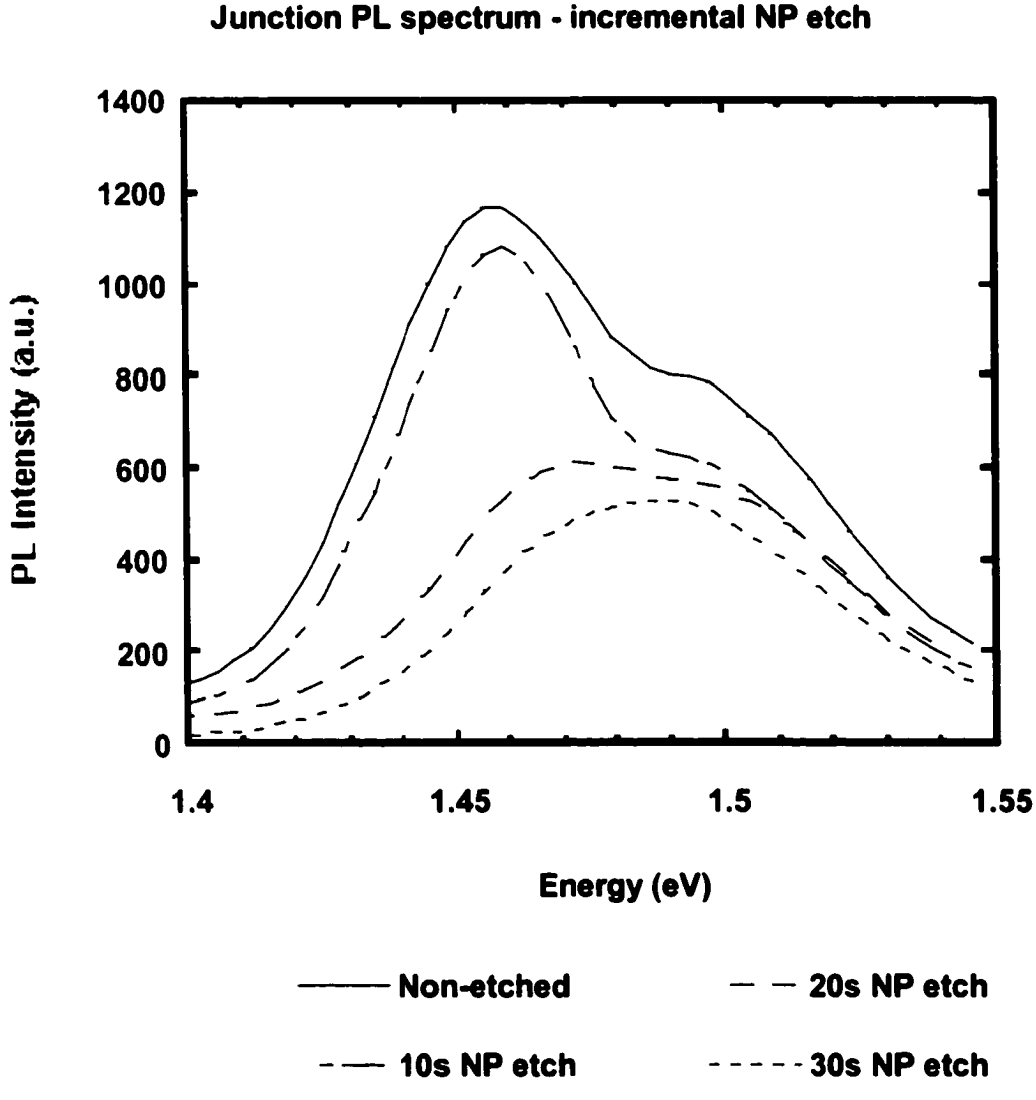

Figure 1.8 **Photoluminescence spectra for NP etched and non-etched CdTe showing a spectral change due to a grain boundary etchant.[39]**

The NP-etch has been previously shown to preferentially etch the grain boundaries and create a tellurium rich layer at grain surfaces.[40] The conclusion from the PL study was

that the NP-etch changed the local fields at the grain boundaries which changed the location of radiative recombination. The radiative recombination occurred closer to the grain boundary in the non-etched films. These PL results prompted the electrical characterization contained within this dissertation, in order to clarify the effects of a backside NP etch on the front-side grain boundaries.

1.7 Statement of Dissertation Objective

It is the aforementioned difficulty in the electrical characterization and understanding of polycrystalline CdTe that this dissertation aims to improve on. A new technique will be utilized to lift-off or separate the post-processed, thin-film polycrystalline CdTe from the CdS, SnO_2 and glass substrate, without the use of chemical etches. The technique will enable electrical characterization to aid understanding of how device processing affects the grain boundaries. Subsequently, the grain boundary information can be used in two-dimensional device emulation programs to determine the effects on device operation.

The goal of this dissertation is to determine the grain boundary barrier potentials, depletion widths, and doping densities near the grain boundaries in polycrystalline CdTe. These properties are to be determined as a function of processing and depth into the film. Quantitative knowledge of these properties as a function of depth will aid in determining more accurate two-dimensional models of the polycrystalline devices. Subsequently, this may lead to improved device understanding.

Chapter 1 References

[1] D.M.Chapin , C.S. Fuller, and B.L. Pearson, *J. Appl. Phys.* **25**, p. 676, (1954).

[2] C.J. Campbell, and J. H. Laherrere, *Scientific America*, pp. 78-91, March 1998.

[3] C.V.Mathai, "Global Climate Change: The Kyoto Protocol", EM, pp.13-16. Febuary (1998).

[4] Photovoltaic Insiders Report, XVII (8), Richard Curry – Editor.

[5] E. Becquerel, *C. R. Hebd. Seances Acad. Sci.*, **9**, p. 561, (1839).

[6] S.M. Sze, Physics of Semiconductor Devices – 2nd Edition, John Wiley and Sons, NY, (1981).

[7] P. A. Crossley, , G.T. Noel, and M. Wolf, "Review and Evaluation of Past Solar Cell Development Efforts", Final Report, FCA Astro-Electronics Division, Princeton, N.J. June (1968).

[8] Takamoto et al., Appl. Phys. Lett., **70**, pp. 381, (1997).

[9] H.J. Hovel, Solar Cells, Vol 11, Semiconductor and Semimetal Series, New York, Academic Press, pp. 217-222, (1975).

[10] K. Zweibel, H. S. Ullal, and B. von Roedern, Twenty Fifth IEEE Photovoltaic Specialists Conference, pp. 745-750, (1996).

[11] J.J. Loferski, *J. Appl. Phys.*, **27**, p 777, (1956).

[12] R.H. Bube, Properties of Semiconductor Materials – Vol. 1 - Photovoltaic Materials, Imperial College Press, London, UK, (1998).

[13] C. Ferekides, J. Britt, Y. Ma, and L. Killian, Twenty Third IEEE Photovoltaics Specialists Conference, pp. 389, (1993).

[14] B.E. McCandless and R.W. Birkmire, *Solar Cells*, 31, pp. 527-535, (1991).

[15] D.H. Levi, H.R. Moutinho, F.S. Hasoon, R.K. Ahrenkiel, L.L. Kazmerski, and M.M. Al-Jassim, AIP Conf. Proc. 353, 13th NREL Photovoltaics Program Review, edited by H.S. Ullal and C. Edwin, AIP Press, pp. 400-411, (1996).

[16] S. A. Galloway, A.W. Brinkman, K. Durose, P.R. Wilshaw and A.J. Holland, *Appl. Phys. Lett.*, **68**(26), pp. 3725-3727, (1996).

[15] A.W. Brinkman, "Properties of Narrow Gap Cadmium based Compounds", EMIS Data Review Series No. 10, edited by P. Capper, INSPEC, London, UK, pp. 575-581, (1994).

[18] Y. Martaing, *Rev. Phys. Appl.*, **12**, p. 211, (1977).

[19] A.L. Fahrenbruch, *Solar Cells*, **21**, p. 399, (1987).

[20] D. Albin, verbal communication, (2000).

[21] J. Sarlund, M.R. Ritala, M. Leskela, E. Siponmaa, R. Zilliacus, *Solar Energy Materials and Solar Cells*, **44**, pp. 177-190, (1996).

[22] A.L. Fahrenbruch, R.H. Bube, "Fundamentals of Solar Cells," Academic Press, New York, N.Y., pp. 363-364, (1983).

[23] T.P. Thorpe, Jr., A.L. Fahrenbruch, and R.H. Bube, *J. of Appl. Phys.*, **60**(15), p. 3622, (1986).

[24] M. Aucouturier, "Polycrystalline Semiconductors Physical Properties and Applications", edited by G. Harbeke, Springer-Verlag, Berlin, (1985).

[25] W.C. Winegard, *Metall. Rev.*, **6**, p. 57, (1961).

[26] I. Kaur et al., "Fundamentals of Grain and Interphase Boundary Diffusion," John Wiley and Sons, Chichester, (1995).

[27] D.H. Levi, L.M. Woods, D.S Albin, T.A. Gessert, R.C. Reedy and R.K. Ahrenkiel, Twenty Seventh IEEE Photovoltaic Specialist – 2nd World Conf. On Photovoltaic Conversion, pp. 1047-1050, (1998).

[28] J.G. Fossum and F.A. Lindholm, several publications.

[29] C. Lanza and H.J. Hovel, *IEEE Trans. on Elect. Dev.*, ED-**27**, (11), pp. 2085-2088, (1990).

[30] L.M. Fraas, *J. of Appl. Phys.*, **49**(2), pp. 871-875, (1978).

[31] Y.J. Lee and J.L. Gray, Twenty Third IEEE Photovoltaics Specialist Conf., pp. 586-591, (1993).

[32] C.H. Seager, D.S. Ginley, and J.D. Zook, *Appl. Phys. Lett.* **36**(10), pp. 831-833, (1980).

[33] J.G. Fossum and F.A. Lindholm, *IEEE Electron Dev. Lett.*, EDL-1,(12), pp. 267-269, (1980).

[34] D.P. Snowden and A.M. Portis, *Phys. Rev.*, **120**(6), pp. 1983, (1960).

[35] R. H. Bube , *Appl. Phys. Lett.*, **13**(4), pp. 136. (1968).

[36] R. Dhere et al.., MRS, Spring, (1996).

[37] R.K. Ahrenkiel, B.M. Keyes, L. Wang, and S.P. Albright, IEEE Photovoltaics Specialst Conf., pp. 940-945, (1991).

[38] R.K. Ahrenkiel, B.M. Keyes, D.H. Levi, K. Emery, T.L. Chu, and S.S. Chu, *Appl. Phys. Lett.*, **64**(21), pp. 2879-2881, (1994).

[39] D.H. Levi, L.M. Woods, D.S. Albin, T.A. Gessert, D.W. Niles, A. Swartzlander, R.K. Ahrenkiel, and P. Sheldon, Twenty Sixth IEEE Photovoltaics Specialist Conf., pp. 351-354, (1997).

[40] D. Niles, X. Li, P. Sheldon, and H. Hochst, *J. Appl. Phys.*, **77** (9), pp. 4489-4493, (1995).

Chapter 2

BACKGROUND

The studies reported in this dissertation utilize fundamental concepts as well as electrical and opto-electronic characterization techniques. This chapter presents relevant background of previous electrical studies of CdTe grain boundaries that have been accomplished to date, and topics necessary to discuss the experimental results herein.

2.1 In-plane Electrical Model of Polycrystalline Films

Numerous studies have been completed to determine the role of grain boundaries on the in-plane resistance of polycrystalline films.[41,42,43] Simple electrical models of polycrystalline films have been proposed to help explain in-plane impedance measurements, and conclude that the grain boundary resistance dominates the DC in-plane resistance.[41] For the purposes of this study, it is necessary to demonstrate that the DC resistances of the films tested herein are dominated by the grain boundary resistance, so that the DC conduction can be characterized by theory for conduction across grain boundaries described in Chapter 3. A method for establishing a dominant grain boundary resistance is discussed in sections 2.1.1 – 2.1.2 as follows.

2.1.1 Frequency-Dependent Resistance of Polycrystalline Material

Snowden[41] showed that the polycrystalline PbS film can be modeled electrically with a simplified RC network as shown within the dotted frame of Figure 2.1. The model in

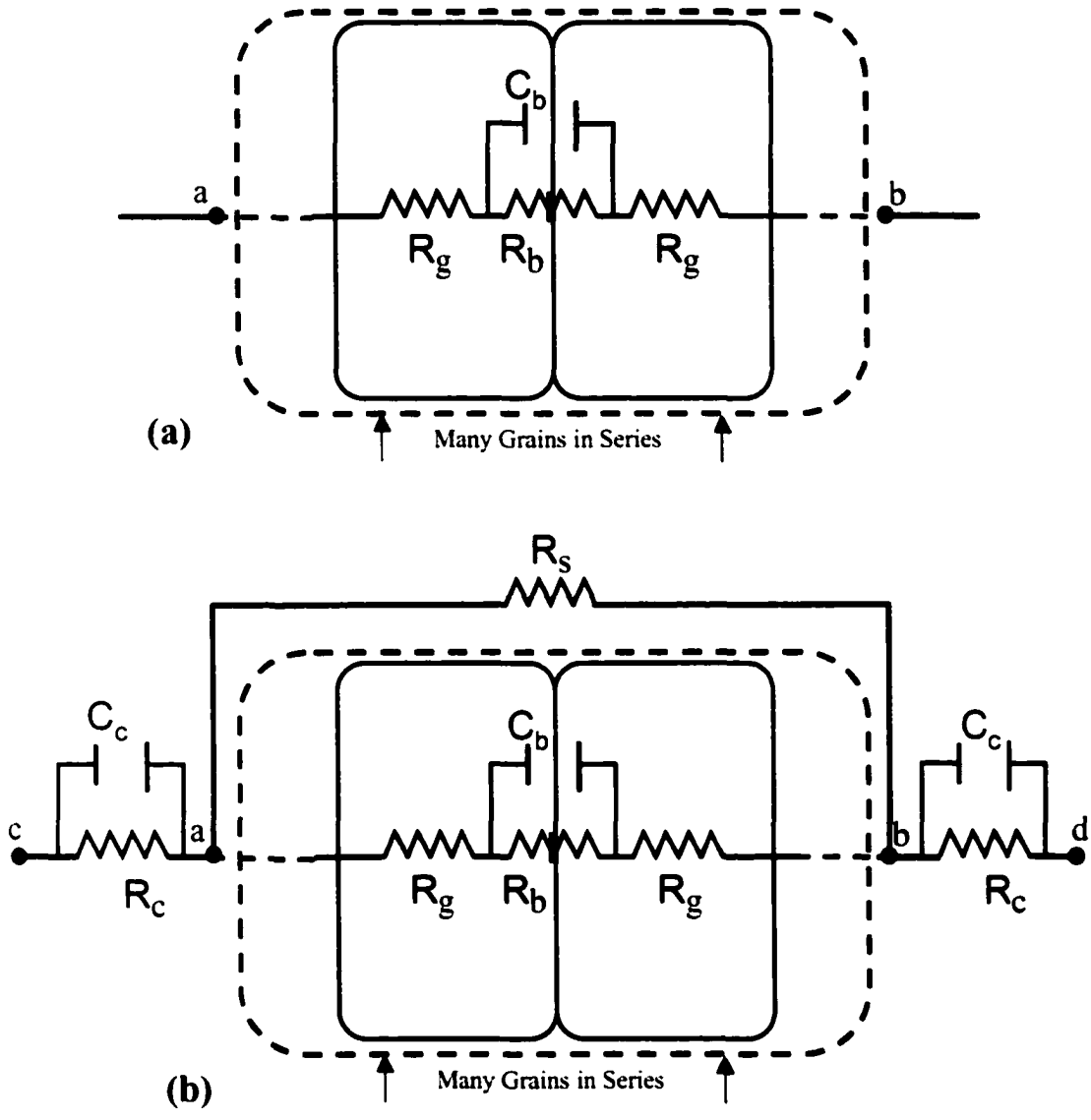

Figure 2.1 **Polycrystalline electrical model (a) showing two grains only with grain boundary resistance, R_b, capacitance, C_b, and intragrain resistances, R_g. Complete model to be considered for measurement purposes (b) includes contact resistances, R_c and capacitances, C_c, and shunt pathway, R_s.**

Fig. 2.1(a) includes an intra-grain resistance, R_g, in series with a grain boundary region modeled as a parallel combination of a resistor, R_b and capacitor, C_b. A more complete model of polycrystalline material would include the effects of a possible shunt path, R_s in Figure 2.1(b). This shunt path could be due to highly conductive grain boundaries, or a highly conductive ohmic layer within the film. Also, during electrical measurements, the influence of the contacts, R_c and C_c in Figure 2.1(b), must be considered. Ignoring for the moment the influence of the shunt path and contacts, then the real part of the impedance, $Re(Z)$, for the circuit in Figure 2.1(a) is defined as $R(\omega)$, and is given as

$$R(\omega) = \frac{(n-1)R_b}{1+(\omega R_b C_b)^2} + nR_g \quad ohms \tag{2.1}$$

where n is the number of identical grains in series. According to the model, if $R_b >> R_g$, then a measurement of $R(\omega)$ should show a breakpoint when $\omega/2\pi = (2\pi R_b C_b)^{-1}$, followed by a dramatic decrease at intermediate frequencies. At higher frequencies, $R(\omega)$ should show another breakpoint when $\omega/2\pi = (4\pi^2 R_g R_b C_b^2)^{-1/2}$, and then flatten out at frequencies beyond this breakpoint. $R(\omega)$ is shown in the solid curve of Figure 2.2 for this case of $R_b >> R_g$. If $R_g >> R_b$, then $R(\omega)$ would exhibit little frequency dependence. At low frequencies $R(\omega)$ is equal to the DC resistance or R_{DC}. From equation (2.1), $R_{DC} \cong n(R_b + R_g)$ for $n >> 1$. At frequencies between the two breakpoints, $R(\omega)$ is approximately proportional to ω^{-2}. At higher frequencies, $R(\omega) \equiv R_{HF} \cong nR_g$, as the higher frequencies effectively shorts out R_b via C_b. Thus, a measurement of R_{DC} and R_{HF} would allow separation of R_b and R_g.

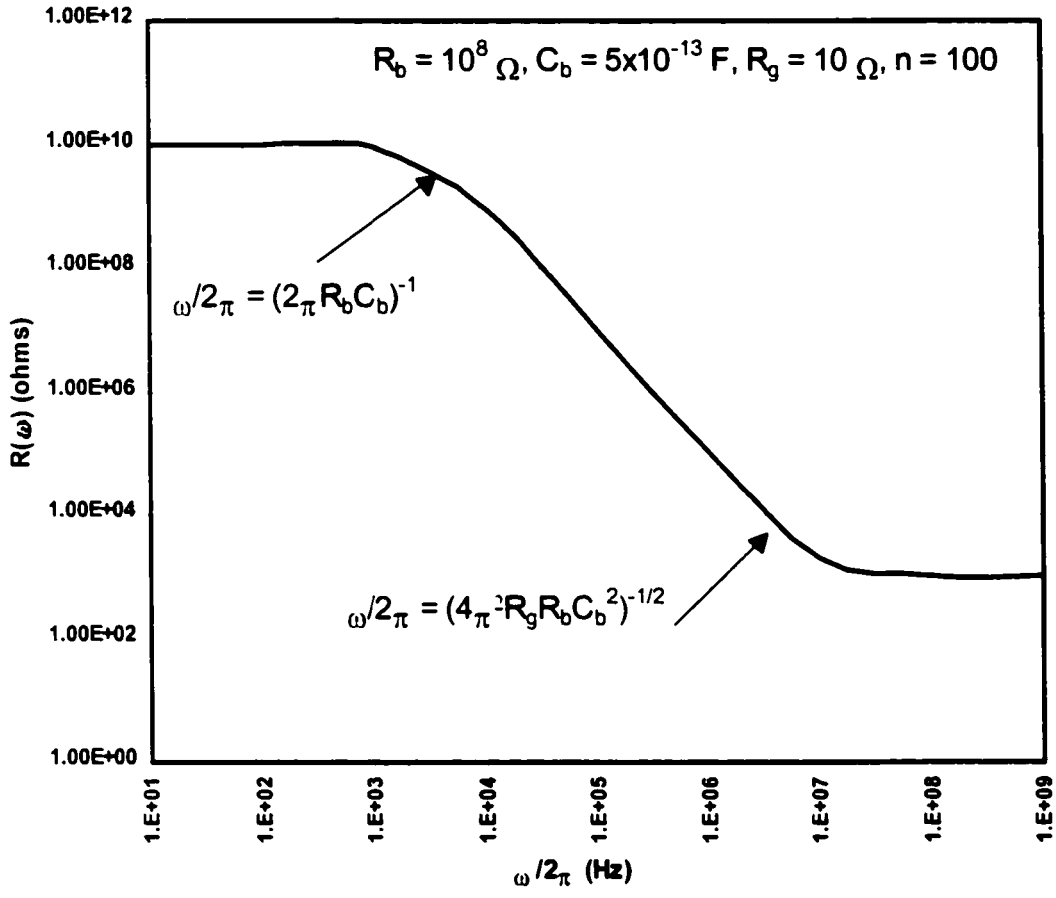

Figure 2.2 **Theoretical $R(\omega)$ for polycrystalline films ($R_b = 10^8\ \Omega$, $C_b = 5x10^{-13}$ F, $R_g = 10\ \Omega$, n = 100). Sample dimensions: length/cross-sectional area = 40 cm^{-1}.**

As mentioned earlier, a more complete model of polycrystalline material would include the effects of a possible shunt path, R_s in Figure 2.1(b). In this analysis, it is assumed that the polycrystalline material is electrically isolated in that there are no other parallel films or substrates that are highly conductive and would confound the measurement. However, in the event $R_s << n(R_b + R_g)$ for $n >> 1$, then a measure of the $Re(Z)$ from a to b would not show any frequency dependence. If $R_s >> n(R_b + R_g)$ for $n >> 1$, then R_s can be ignored and $Re(Z)$ can be described by $R(\omega)$.

At this point in the impedance analysis, if the measured *Re(Z)* has the *shape* of the curve in Figure 2.2, then $R_{DC} \cong (n\text{-}1)R_b$, and a DC measurement enables us to measure the grain boundary properties. However, in the event of a non-negligible contact resistance, then $R_{DC} \cong (n\text{-}1)R_b + 2R_c$. Thus, another measurement technique is required to show that the contact resistance can be neglected, and is described later.

2.1.1.1 Frequency Dependence Resistance with Grain-Boundary Feedback

The simple grain-boundary electrical model assumes that the grain-boundary barrier height does not change with the application of a small AC voltage. However, during the application of the AC signal some charge is injected into grain-boundary traps, which changes the occupancy of the these trap states. Depending on the amount of charge injected and the density of trap states at the grain boundary, then this could significantly alter the quasi-Fermi level at the grain-boundary. If so, then there is an out-of-phase modulation of the barrier height, which yields an out-of-phase conduction and capacitance component. Pike and Seager modeled this effect assuming a constant grain boundary density of trap states, and therefore a single time-constant (τ) for equilibrating trapped charge at the grain boundary, and is given as follows: [44]

$$R_b(\omega) = \left(\frac{1}{R_{LF}} + \frac{\omega^2 \tau C_D}{1 + \omega^2 \tau^2} \right)^{-1} \quad \text{ohms} \qquad (2.2a)$$

$$C_b(\omega) = C_{HF} + \frac{C_D}{1 + \omega^2 \tau^2} \quad \text{farads} \qquad (2.2b)$$

where R_b and C_b are now dependent on the frequency of the AC signal, R_{LF} represents the frequency-independent part of the grain-boundary resistance, C_{HF} is the grain-boundary capacitance measured at high-frequency, and C_D is the capacitance related to the changes in the right- and left-hand side grain boundary depletion regions with applied bias. By

definition, $C_D >> C_{HF}$. These frequency-dependent values of R_b and C_b can then be inserted into equation (2.1). The low and high-frequency breakpoints of $R(\omega)$ without grain-boundary feedback, or $\tau >> R_{LF}C_D$, become $\omega_{LF} \cong (R_{LF}C_D)^{-1}$ and $\omega_{HF} \cong (R_{LF}R_g C_D^2)^{-1/2}$, respectively, using these modified definitions of R_b and C_b. If $\tau << R_{LF}C_D$, then the modified theory with grain-boundary feedback contains four breakpoints located at $\omega_1 = \omega_{LF} \cong (R_{LF}C_D)^{-1}$, $\omega_2 \cong (\tau R_{LF}C_D)^{-1}$, $\omega_3 \cong (\tau C_{HF}/C_D)^{-1}$, and $\omega_4 \cong (C_D/(\tau R_g C_{HF}^2))^{-1/2}$, listed in order of appearance with increasing frequency. Note that ω_{LF} is still present in this case with grain-boundary feedback. Also, if τ is very small, then ω_2, ω_3 and ω_4 are not observed as ω_{HF} appears first. Several examples of the frequency-dependent resistance with grain-boundary feedback are given in Figure 2.3 where τ, R_{LF}, R_g, C_{HF}, and C_D are as given in the figure.

It is important to note that at very low frequencies, $R(\omega) \cong n(R_{LF} + R_g)$ for $n >> 1$, and is unaffected by the grain-boundary feedback. Likewise at high-frequency, $R(\omega) \cong nR_g$. Thus if $R_{LF} >> R_g$, then $R_{DC} \cong (n-1)R_{LF}$ or the grain-boundary resistance, as in the simple theory, and $R(\omega)$ will show a drop between low and high frequencies with either two or four breakpoints.

Lastly, the modified theory with grain-boundary feedback accounts for only a single time constant, τ, and capacitance C_D, corresponding to a constant grain-boundary density of states. It is more likely that the grain-boundary density of states is a smoothly varying function of energy,[23] thus τ and C_D would be smoothly varying with the applied voltage. This in effect would act to smooth out the frequency dependence between the low and high-frequency breakpoints, as no single set of breakpoints would be apparent due to the

continuous array of breakpoints. Thus, the slope of the $R(\omega)$ frequency dependence would most likely deviate from the ω^{-2} dependence as predicted by the simple theory without grain-boundary feedback.

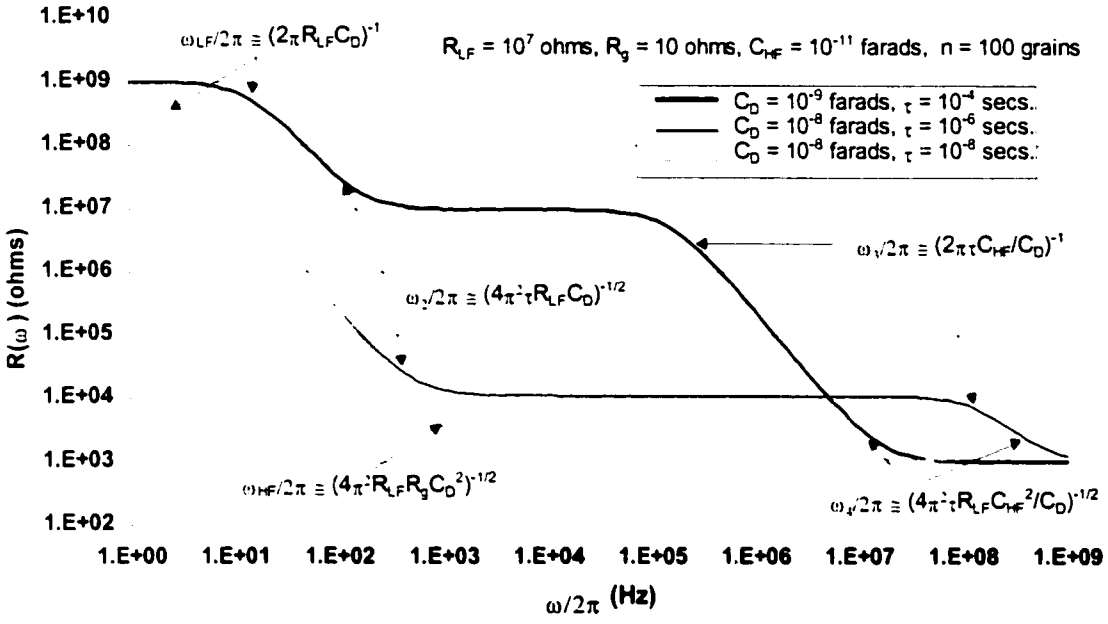

Figure 2.3 **Theoretical plots of R(ω) modified to include grain-boundary feedback. Several examples are shown with variable values of C_D and τ as indicated.**

2.1.2 Contact Resistance

Tunneling Schottky barrier contacts can be modeled in a similar way as grain boundaries. That is, the metal semiconductor junction can modeled as a capacitor, C_c, in parallel with resistor, R_c, as shown in Figure 2.1(b). The same surface states that pin the Fermi level near mid-gap at grain boundaries can also pin the Fermi level at a Schottky barrier metal-semiconductor interface. This could lead to similar band bending and depletion widths in the semiconductor and thus similar barrier potentials. Consequently, the resistance of the Schottky barrier contacts may be similar to that of the grain boundary. If R_c is large, then it may interfere with an attempt to directly measure the

polycrystalline film DC resistance as discussed above. To form a low resistance tunneling contact, the doping under the contact must be greatly increased, and the contact area should be made as large as possible. A method for determining if the contact resistance is negligible compared to the film resistance is discussed as follows:

The Transfer Length Method (TLM)

For the purposes of this study, it is necessary to demonstrate that the contact resistance is negligible compared to the film resistance when measured over a wide range of temperatures and illumination conditions. The TLM[45,46] is ideally suited for this purpose as it provides a direct measure of the contact resistance. The method requires several parallel contacts to be deposited on the film and of the same length (L) and width (W), but spaced at various distances from each other. Here again, it is assumed that the polycrystalline material is electrically isolated in that there are no other parallel films or substrates that are highly conductive and would confound the measurement. A top view of a possible contact configuration is shown in Figure 2.4(a). The resistance is measured across the various gaps and is plotted against the gap widths as shown in Figure 2.4(b). The extrapolated intercept of the fitted line to the resistance axis, represents the point of zero film resistance, and is equal to twice the contact resistance, $2R_c$.

2.1 Previous In-plane CdTe Electrical Studies

This section contains information on previous in-plane electrical characterization of CdTe. Few researchers[23,47] have characterized CdTe grain boundary barrier potentials in the past due to the difficulty in accounting for polycrystalline effects. Previous grain boundary electrical characterization has focused primarily on bicrystals, as the single grain boundary can be well defined. With bicrystals, measurements of the bulk doping,

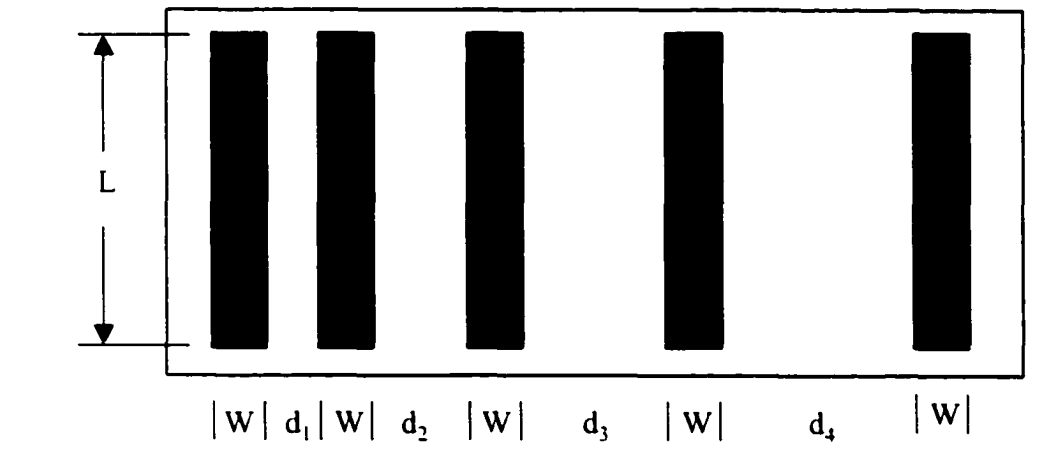

(a)

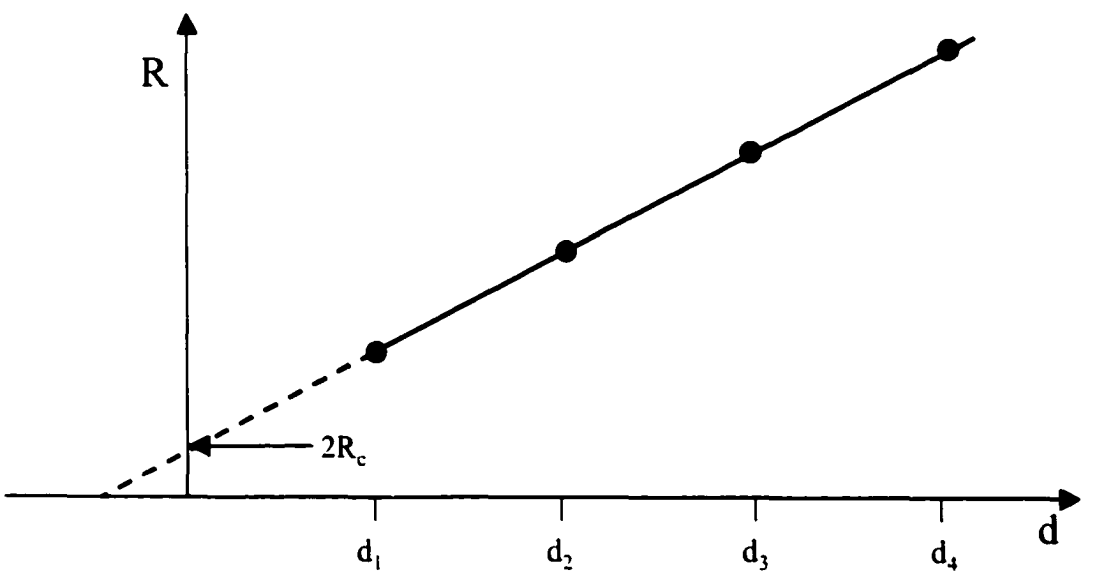

(b)

Figure 2.4 **Transfer Length Method (TLM) showing (a) contact test structure with equally sized contacts, but variable spacing, d, and (b) contact resistance determination from extrapolated fit of resistance versus spacing plot to resistance axis intercept.**[45]

number of grain boundaries (one), and grain boundary cross-sectional area are more easily accomplished. This makes capacitance techniques for measuring the grain boundary barrier potential possible. Bicrystal samples are usually made from thick, large grained, polycrystalline wafers sawn from a polycrystalline ingot. However, it is likely that the grain boundaries in the ingot growth may be much different that those created during the coalescence stages of thin film growth. The growth conditions, intrinsic doping level, degree of impurity segregation, grain size, and orientations could all be different than that of films grown by thin film growth. Consequently, any conclusions drawn from bicrystals, are at best, merely indications of possible polycrystalline behavior. Therefore, it is desirable to extract grain boundary information from polycrystalline material. However, bicrystal data will be used to validate the theories presented in chapter 3 by comparing the results from these theories with the results from capacitance techniques described below. To date, measurements of polycrystalline CdTe have usually been limited to resistivity and photoconductivity measurements. The only attempts to estimate the grain boundary barrier potentials have been from measuring conductivity activation energies. More refined techniques has been applied to Si and GaAs polycrystalline material and will be discussed later.

2.2.1 Bicrystals

Bicrystal samples are created by cutting out a sample from the wafer that contains a single grain boundary that is approximately straight and forms a plane that bisects the sample. Contacts are applied on both sides of grain boundary to characterize the single grain boundary. Additional contacts can be applied to characterize the surrounding bulk crystalline material. Thorpe et al.[23] used bicrystals to evaluate several techniques for

studying the effects of different passivation techniques on grain boundary barrier potentials. The techniques employed were: 1) measurement of the zero bias grain boundary capacitance, C_0; 2) measurement of voltage intercept from the grain boundary capacitance-voltage relation; and 3) measurement of conductivity activation energy, E_a. In this dissertation, bicrystals will be used to validate a method for determining grain boundary barrier potentials, which will then be applied to polycrystalline thin films. The following describes the measurement techniques used by Thorpe et al. in greater detail.

2.2.1.1. Zero Bias Capacitance Measurements

The grain-boundary barrier potential at zero bias, V_{b0}, can be determined from Poisson's equation as applied to a double depletion region or:

$$V_{b0} = \frac{q\varepsilon_s N_b A^2}{8C_{b0}^2} \quad V \tag{2.3}$$

where ε_s is the semiconductor bulk permittivity, A is the grain boundary cross-sectional area, N_b is the doping density in the vicinity of the grain boundary and C_{b0} is the measured grain boundary capacitance at zero bias or C_b in Figure (2.1a). C_{b0} is found from the imaginary part of the impedance Im(Z), and can be determined at any frequency provided R_b and R_g are known (n = 2 for bicrystals). However at high frequencies, Im(Z) is proportional to C_{b0} only. Thus the measurement is typically performed at high frequencies. C_{b0} is also given by:

$$C_{b0} = \frac{\varepsilon_s A}{2x_{d0}} \quad F \tag{2.4}$$

where x_{d0} is the grain boundary depletion depth at zero bias. Thus, the frequency of the applied field should be also be high enough such that the width of the grain boundary depletion region is not influenced by deep level defects,[48] or any grain-boundary feedback

effects as described earlier. The accuracy of V_{b0} is primarily limited to an accurate knowledge of the N_b. Here, N_b is assumed constant and independent of position. Using values of the doping density measured from the bulk may be misleading due to impurity segregation and diffusion near the grain boundaries. Additional complications arise in accurately measuring C_{b0}, as it may be difficult to separate C_{b0} from the serially connected contact capacitances, C_c, which may be comparable to or smaller then C_{b0}. At zero bias, C_c or the metal-semiconductor junction capacitance, is given as:[49]

$$C_c = A\sqrt{\frac{q\varepsilon_s N_a}{2\phi_i}}\ F \tag{2.5}$$

where A is now the the contact area, N_a is the semiconductor doping concentration immediately under the metal contact, and ϕ_i is the junction built in potential. Thus, equation (2.5) is a similar expression to that of the capacitance for a single grain boundary (solve equation (2.3) for C_{b0}). Assuming for the moment that $V_{b0} \approx \phi_i$ as discussed in section 2.1.2, then either the contact area must be made very large, or N_a must be made very large in order to increase the contact capacitance above that of the grain boundary capacitance. If possible, both contact area and N_a are adjusted. N_a is usually made large anyway to reduce the contact resistance, but very high levels are difficult to attain due to compensation. Also, the cross-sectional area of a grain boundary may be comparable to that of the top surface contacts when using thick bicrystals. Finally, C_{b0} may be very large due to impurity segregation in the vicinity of the grain boundaries. All of these factors make it difficult to separate C_{b0} from C_c. The magnitude of the C_c can be found from a capacitance measurement of the bulk single crystal material

next to the grain boundary by using an adjacent set of contacts not spanning the grain boundary.

2.2.1.2 In-Plane C-V Measurements

A second technique makes use of the C-V relation for a grain boundary assuming the applied voltage is supported on the reverse-biased side of the grain boundary:[50]

$$\left(\frac{2C_{b0}}{C}-1\right)^2 = 1+\frac{V}{V_{b0}} \tag{2.6}$$

V_{b0} is determined by the voltage intercept obtained by extrapolating a plot of the left hand side of equation (2.6) versus voltage. An example of this technique is shown in Figure 2.5 for a CdTe bicrystal measured by Thorpe et. al.[23] This technique is not limited by

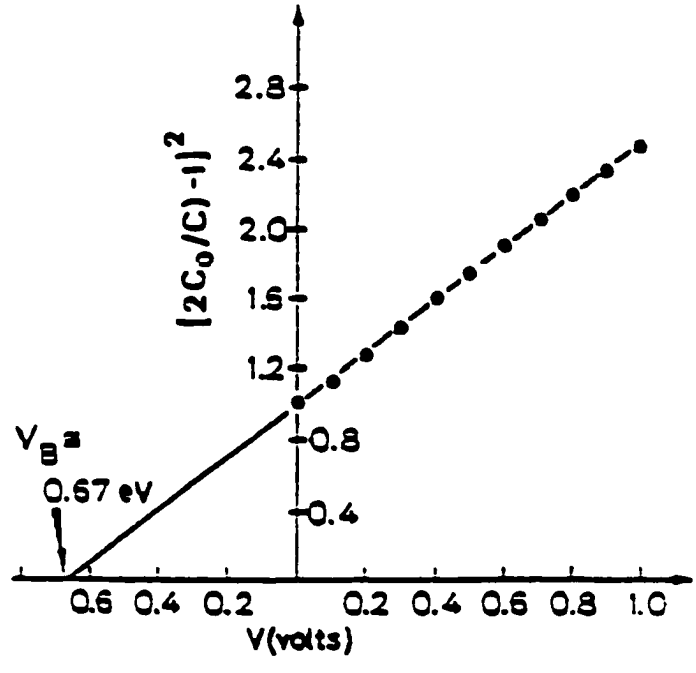

Figure 2.5 **In-Plane C-V Measurement on CdTe bicrystal. Left side of Eqn. (2.6) versus applied voltage. Extrapolated voltage intercept is V_{b0}.[23]**

needing to know the values of N_b or the grain boundary cross-sectional area. However, the accuracy of this technique may still be compromised by the contact capacitance as discussed earlier.

2.2.1.3. Activation Energy Measurement

A third technique for determining the grain boundary barrier potential is accomplished by measuring the current or conductance versus temperature, and using the assumption of thermionic emission as the conduction mechanism over the grain boundary barrier. The details of the thermionic emission theory will be discussed later in Chapter 3. The temperature dependent data is plotted on an Arrhenius plot, and the slope of the line is the activation energy, E_a. Under the assumption of thermionic emission, then $E_a = q\Phi_{gb}$, where $q\Phi_{gb}$ is as shown in Figure 1.3. With additional knowledge of the energy separation between the Fermi level and the majority-carrier band edge, or E_{vf} in Figure 1.3, near the boundary, then the barrier potential can be found from:[23]

$$qV_{b0} = E_a - E_{vf} \qquad V \tag{2.7}$$

An example of this technique was performed as a function of illumination intensity and is shown in Figure 2.6 for CdTe bicrystals. In this example, the authors[23] could not fit the data with a single activation energy, and only used fits to the low temperature data to calculate the barrier height as a function of illumination (see inset of Figure 2.6). In this experiment the bulk doping was measured to be 2 x 10^{16} cm^{-3} and the barrier height was determined from equation (2.7). The experiment demonstrates the effect of illumination on CdTe grain boundaries. That is, the light generates electon-hole pairs which increases the minority carrier current to the grain boundary and neutralizes oppositely charged grain boundary defects. This results in a diminished density of defect states at the grain

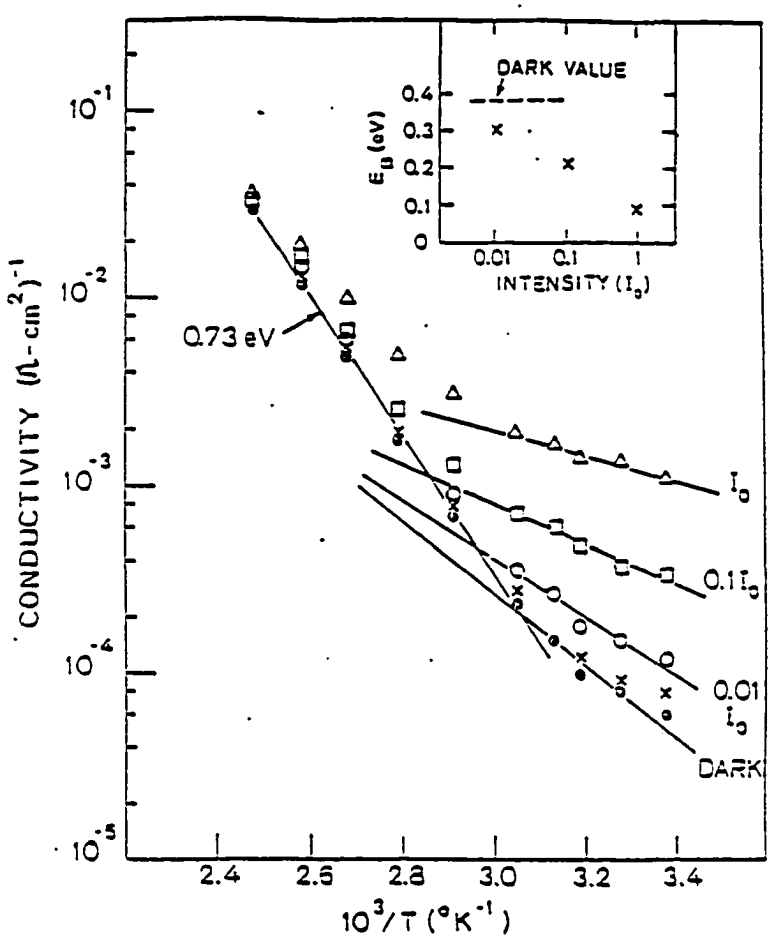

Figure 2.6 **CdTe Bicrystal Activation Energy Measurement. Arrhenius plots of conductivity versus temperature data under various levels of illumination. The slope of the line is the activation energy, E_a. Inset shows barrier height as determined from eqn. (2.7) versus light intensity.[23]**

boundary, unpinning the Fermi level and lowering the grain boundary barrier height. However, since the dark data can not be fit by a single activation energy, then the assumption of thermionic emission as the majority carrier current conduction mechanism is questionable. As discussed in chapter 3, other grain boundary conduction models such as thermally-assisted-tunneling, may fit the dark data throughout the entire temperature range. Thermionic emission theory may describe current conduction in this temperature range and for typical CdTe bulk doping densities, but not for doping densities above 10^{17}

cm^{-3} (see Figure 3.1 in chapter 3). Thorpe et al.[23] assumed that the doping and consequently E_{vf} was the same as in the bulk of the material, which may not be accurate given the tendency for impurities to segregate near grain boundaries.

2.2.2. Polycrystalline CdTe Activation Energy Measurements

The activation energy measurements described for bicrystals have also been used on polycrystalline films. Thorpe et al.[23] and von Windheim et al.[47] have measured activation energies on polycrystalline CdTe films. Some activation energy measurements from both of these studies are shown in Figure 2.7 for various treatments of polycrystalline CdTe films. The study by Thorpe et al. (Fig. 2.7a) demonstrated that the grain boundary defect states could be temporarily passivated by diffusion of Lithium atoms. Following just the dark data for the moment, the conductivity activation energy before the Li diffusion is 0.44 eV with a low conductivity, and 0.35 eV after the Li diffusion with a two orders of magnitude increase in the conductivity. Two months later, the conductivity and activation energy have nearly returned to their initial values. The light data follows the same trend. The study by von Windheim et al. (Fig. 2.7b) used the measurement of the conductivity activation energy to demonstrated that CdTe grain boundaries are sensitive to the annealing atmosphere and to tellurium or cadmium diffusions. Using the anneal in argon as a baseline, von Windheim showed that both an anneal in air, or excess tellurium can lower the conductivity activation energy, while excess cadmium increases the activation energy. The tellurium diffusion treatment is of particular interest for later comparison herein, as the NP etch creates a tellurium-rich layer in the grain boundaries. None of these studies used CdTe thin films as-processed for devices, but used films grown on insulating glass substrates only. Consequentially the results may be different

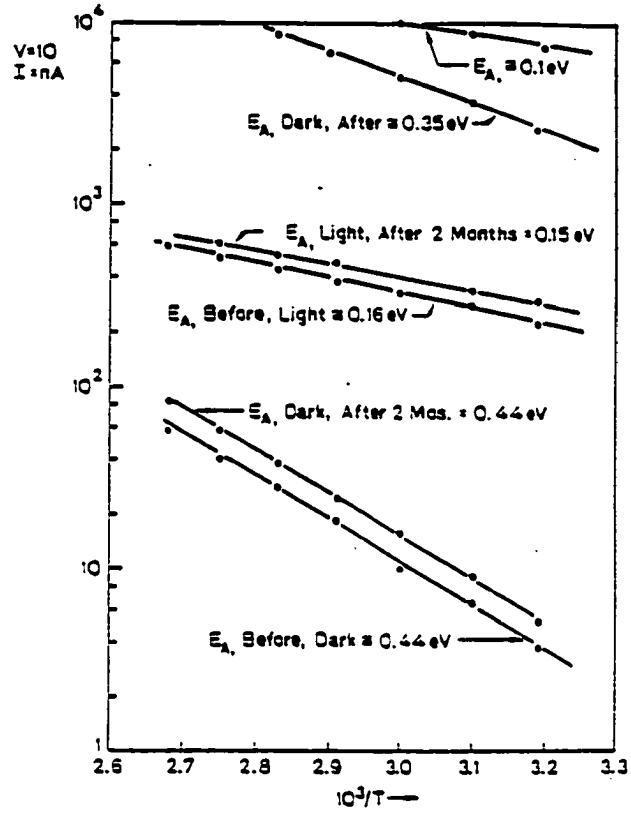

(a)

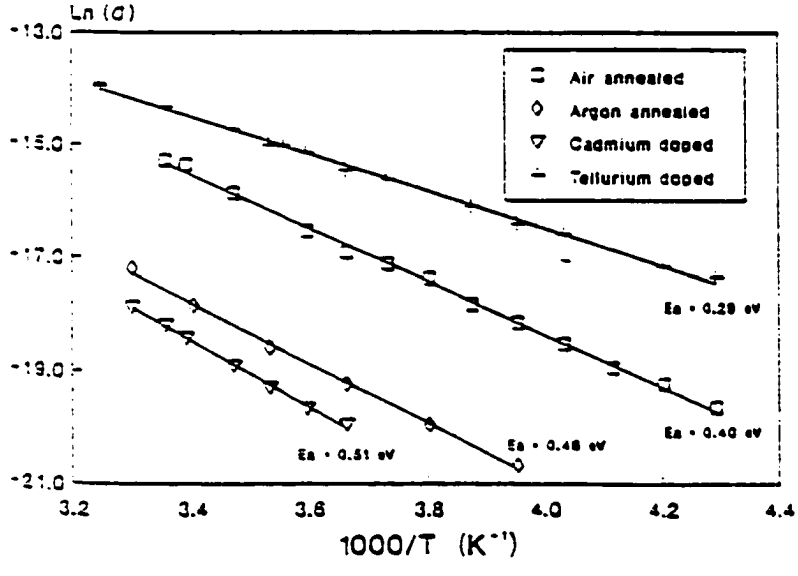

(b)

Figure 2.7 **Thin-film Polycrystalline Activation Energy Measurements. (a) Effects of a Li diffusion, before, after and two months after, on light and dark activation energy,[23] and (b) effect of air anneal and Te and Cd diffusions on activation energy when compared to a baseline argon anneal.[47]**

when compared to films that are subjected to the device processing. However, these previous studies do demonstrate that the CdTe grain boundaries are sensitive to processing treatments.

In these previous CdTe polycrystalline studies, there was no attempt to determine the barrier energy, V_{b0}, presumably due to the difficulty in obtaining an accurate measure of the doping density or E_{vf} in the polycrystalline material. Thus, the activation energy measurement is only a relative measure of the barrier energy at best. Despite this fact, a relative measure of the barrier energy was sufficient to demonstrate processing effects on polycrystalline CdTe grain boundaries. As discussed earlier, this method is only accurate if thermionic emission is the conduction mechanism. In order to determine accurate numbers for modeling, better or more refined methods and understanding are necessary.

2.2.3 GaAs Bicrystal Measurements

One particular in-plane characterization of GaAs bicrystals is included here because it uses a refinement to the previously discussed activation energy measurement, and due to its similarity with the method outlined in chapter 3 of this dissertation. Seager and Pike[51] used both thermionic emission theory and thermally assisted tunneling theory to fit conductance versus temperature data of lightly doped, 10^{15} cm^{-3}, and highly doped, 10^{17} cm^{-3}, GaAs bicrystals. At the high doping level, theory suggests that the conduction mechanism across the grain boundaries should be thermally assisted tunneling. This is indeed what Seager and Pike found. Thermionic emission fit the data from the lightly doped samples better, and thermally assisted tunneling fit the data from the highly doped samples better. The fits are shown in Figure 2.8.

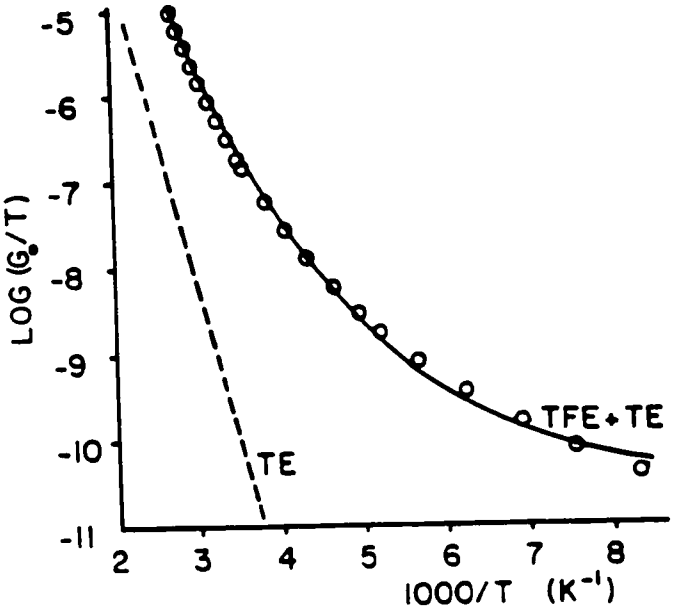

Figure 2.8 **Arrhenius Plot of highly doped (2×10^{18} cm^{-3}) bicrystal showing an improved fit using a thermally assisted tunneling model (TFE + TE) as opposed to a thermionic only model (TE). Both curves used a barrier height determined by the zero bias capacitance.[51]**

2.2.4 Effect of Grain Boundary Barrier Potential Inhomogenities

J. H. Werner has done theoretical studies on the effects of grain boundary barrier inhomogenities during temperature measurements.[52,53] The inhomogenities arise from potential fluctuations along the two-dimensional grain boundary, or spatial inhomogenities, and potential fluctuations from different types or orientations of grain boundaries, or structural inhomogenities. Werner's results showed that the grain-boundary inhomogenities can produce curved Arrhenius plots for the current or conductivity. This could interfere with the interpretation of the conduction mechanism, and lead to misguided calculations of the grain boundary barrier heights and doping levels. Werner employed a statistical analysis applied to thermionic emission transport, and will be discussed in detail in chapter 3. The effects of his statistical analysis yield an additional fitting parameter, which is the standard deviation of the barrier potential.

Werner was able to fit data using this extra degree of control, which previous researchers attributed to tunneling. These fits are shown is Figure 2.9.

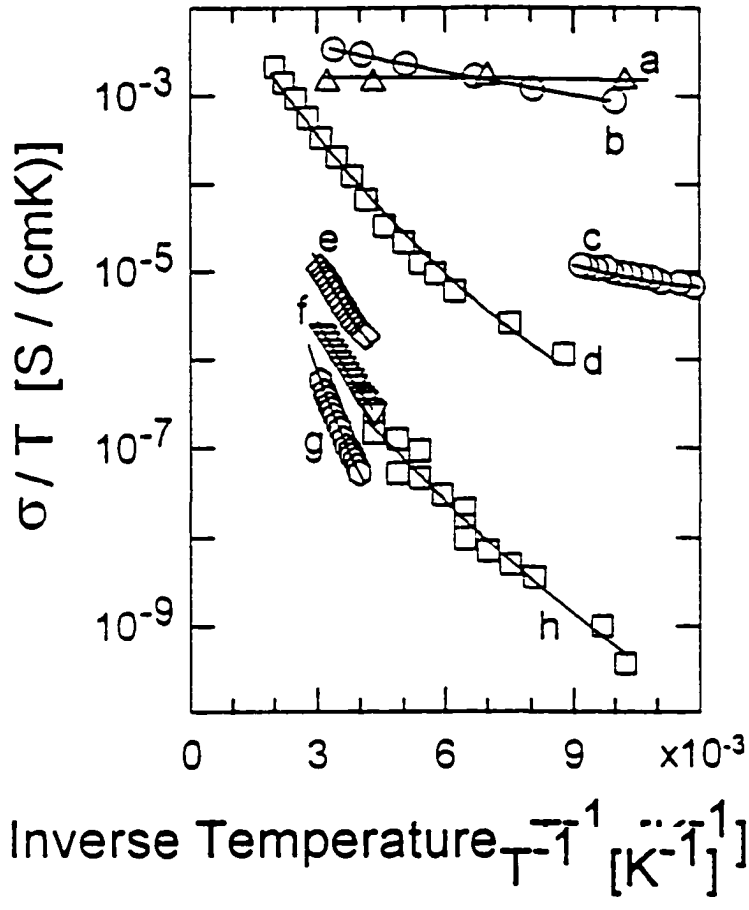

Figure 2.9 **Arrhenius plots of assorted films from the literature showing good fits with thermionic emission theory modified to include grain boundary inhomogenities.[53]**

2.3 Research Plan

This dissertation will extend the present methods for characterization of polycrystalline CdTe thin films discussed above. This will be accomplished by using Schottky barrier theory modified for grain boundaries as described in the next chapter. This theory will be fit to current versus temperature data to determine the grain-boundary barrier potential, depletion widths and doping in the vicinity of the grain boundary of as-processed

polycrystalline CdTe. The technique will be validated on bicrystal data, where the results can be corroborated with the capacitance techniques outlined in section 2.2.1. Prior to this, an unambiguous determination of the grain boundary dominance of the DC resistance must be demonstrated. This will be done with a measure of the resistance frequency response as described in section 2.1, for the polycrystalline material. Additionally, the effects of contact resistance will be shown to be negligible. Finally, the technique will be used to study the effects of CdTe solar cell processing on the grain boundaries from an NP etch, a $CdCl_2$ heat treatment, and CdTe source plate usage.

Chapter 2 References

[41] D.P. Snowden and A.M. Portis, *Phys. Rev.*, **120**(6), pp. 1983, (1960).

[42] R. H. Bube , *Appl. Phys. Lett.*, **13**(4), pp. 136. (1968).

[43] G.H. Blount, R.H. Bube, and A.L. Robinson, *J. of Appl. Phys.*, **41**(5), pp. 2190, (1970).

[44] C.H. Seager and G. E. Pike, *Appl. Phys. Lett.*, 37(8), pp.747-749, (1980).

[45] D.K. Schroder, "Semiconductor Material & Device Characterization", John Wiley & Sons, Inc., New York, (1990).

[46] W. Shockley, A. Goetzberger, and R. M. Scarlett, "Research and Investigation of Inverse Epitaxial UHF Power Transistors," Rep. No. AFAL-TDR-64-207, Air Force Avionics Lab., Wright-Patterson Air Force Base, OH, Sept., (1964).

[47] J. von Windheim, I. Renaud, and M. Cocivera, *J. Appl. Phys.*, 67(9), pp. 4167-4172, (1990).

[48] D.L. Losee, *J. of Appl. Phys.*, **46**(5), pp. 2204-2214, (1975).

[49] R.S. Muller and T.I. Kamins, "Device Electronics for Integrated Circuits", John Wiley & Sons, N.Y., (1986).

[50] M.G. Spencer, W.J. Schaff, and D.K. Wagner, *J. of Appl. Phys.*, **54**(3), pg. 1429, (1983).

[51] C.H. Seager and G.E. Pike, *Appl. Phys. Lett.*, **40**(6), pp 471-474, (1982).

[52] J. H. Werner and H. H. Guttler, *J. Appl. Phys.*, **69**(3), pp1522-1533, (1991).

[53] J. H. Werner, *Solid State Phenom.*, **37-38**, pp 213-218, (1994).

Chapter 3

THEORY OF CONDUCTION ACROSS GRAIN BOUNDARIES

In this chapter the grain boundary current-voltage characteristic and the theory for different conduction mechanisms across grain boundaries is presented. Grain-boundary energy barriers as shown in Figure 3.1 can be viewed as back-to-back parabolic barriers. Thus, the conduction of current over either side of a grain boundary potential barrier can be described in a manner similar to Schottky barrier conduction. The primary deterrent to theoretically determining the magnitude of the conduction across a grain boundary potential barrier is the lack of knowledge of the doping density within the grain boundary

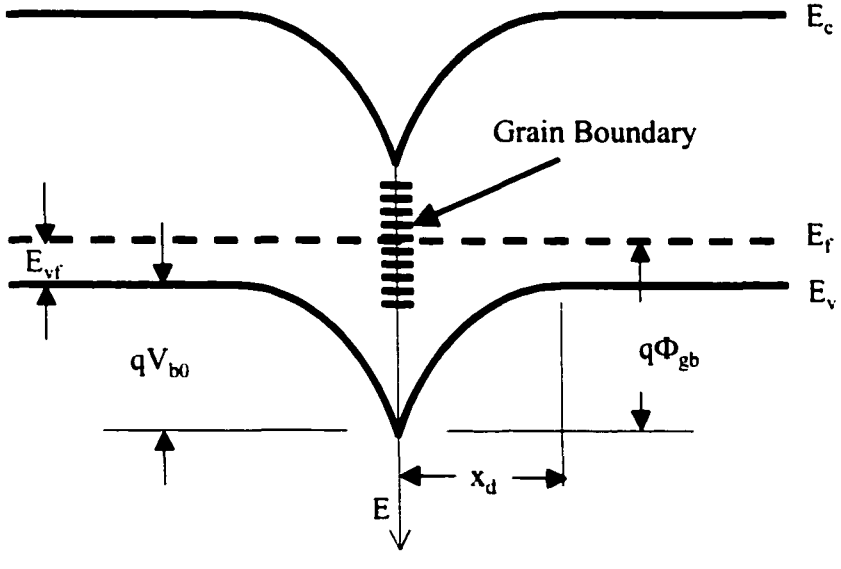

Figure 3.1 **Grain boundary band diagram of inverted grain boundary with p-type bulk at zero bias. Energy is drawn downward for holes. Φ_{gb} is the grain boundary barrier height, V_{b0} is the zero-bias band bending, and x_d is the grain boundary depletion width.**

depletion region. Without this knowledge one can not easily determine whether the primary conduction mechanism is drift-diffusion, thermionic emission, thermally assisted tunneling or just tunneling. Figure 3.2, taken from Fahrenbruch and Bube,[22] shows the approximate range, value, and dependence on the doping density for each conduction model given a Schottky barrier of 1.0 eV.

In this dissertation, the conduction mechanism will be determined from an analysis of the conductivity temperature dependence in the temperature range of approximately 298°K to 400°K. The temperature dependent theory for each conduction mechanism is fit to the data, and the conduction model that best fits the data is interpreted as the dominant conduction mechanism. Values of barrier height and doping density are taken from this best fit. An approach similar to this has been successfully used in the past on GaAs bicrystals.[51]

3.1 Current-Voltage Characteristic Across Grain Boundaries

A current-voltage relation for carriers crossing a grain boundary has been developed by Mueller,[54] and is given as follows:

$$J(V) = 2[(1-\gamma)J_0]\tanh\left(\frac{qV}{2kT}\right) \quad A/cm^2 \tag{3.1}$$

where J_0 is the conduction model-dependent majority carrier saturation current for conduction across the grain boundary. γ is the grain boundary carrier capture coefficient and is a number between 0 and 1 representing the fraction of carriers crossing the barrier that are captured at the grain boundary. For the case of polycrystalline films, V becomes an estimate of the voltage applied per grain boundary. Usually the voltage bias is applied over hundreds of grain boundaries, which results in the case that the applied bias per

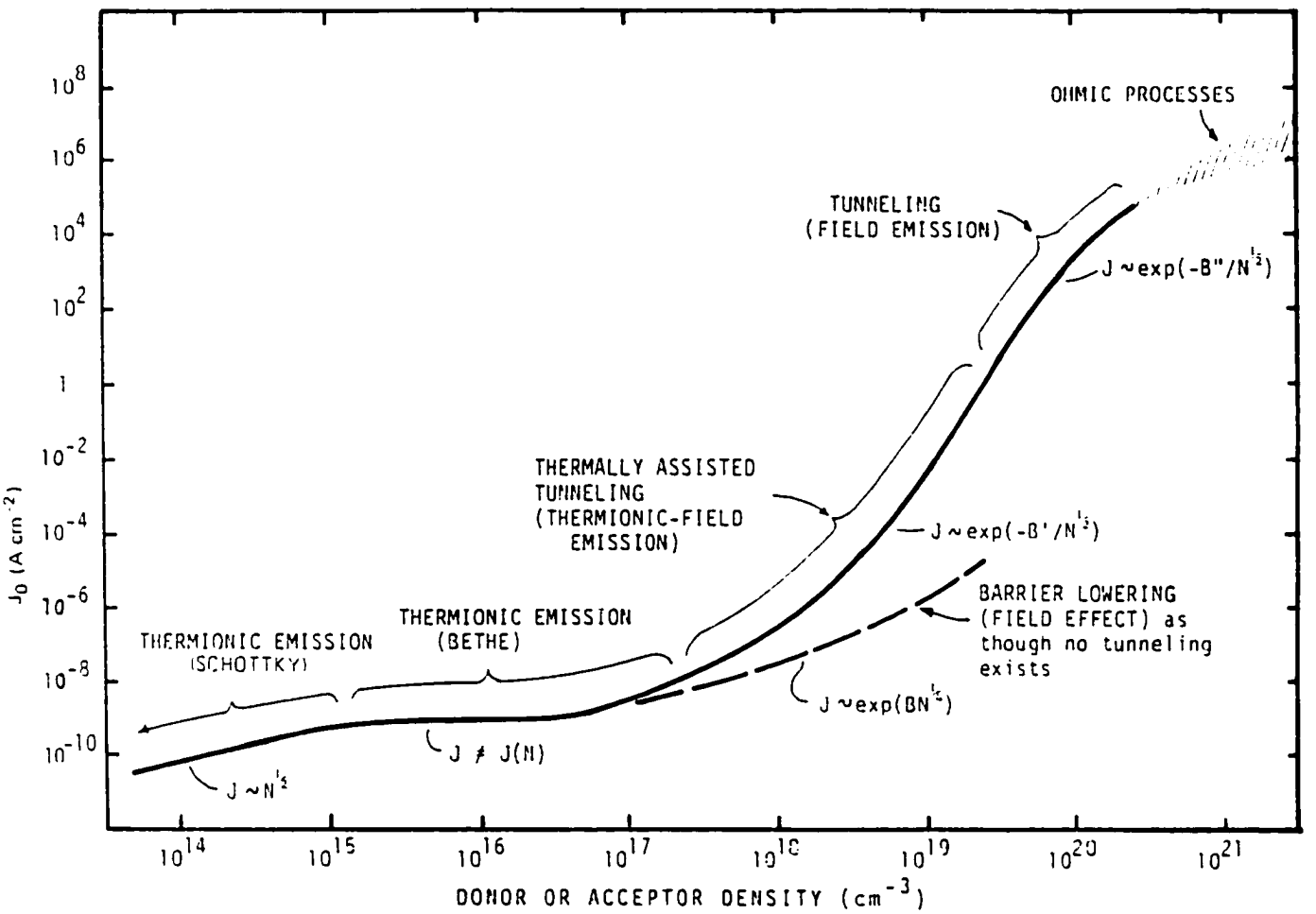

Figure 3.2 **Qualitative plot of zero-bias saturation current, J_0, versus doping density, N for a Schottky diode. B, B' and B'' are constants and T = 300K. The boundaries of the regions and the values of J_0 depend on the detailed properties of the semiconductor. A barrier height of 1.0 eV is assumed.[22]**

grain boundary is small, or $qV < 2kT$. In the case of a small applied bias, equation (3.1) can be simplified by approximating the hyperbolic tangent term with its argument. Thus for small applied biases, the current is linear with voltage. A convenient feature of equation (3.1) is that it is independent of the fractional distribution of V over the two sides of the grain boundary.

Equation (3.1) applies to all conduction models as long as conduction across each side of the grain boundary can be described by the Schottky barrier current-voltage relation, or:

$$J(V) = J_0\left[\exp\left(\frac{qV_1}{kT}\right) - 1\right] \quad A/cm^2 \tag{3.2}$$

where V_1 is positive for the forward biased side of the grain boundary and negative for the reverse biased side. Conduction across grain boundaries by drift-diffusion and thermionic emission fit the form of equation (3.2), however it is an approximation for conduction by thermally-assisted tunneling. Consequently, equation (3.2) is of limited applicability and is not valid in the case of tunneling *without* thermal assistance. This is discussed further, as well as the derivation of equations (3.1) for thermally-assisted tunneling, in Appendix A.

The value of γ depends on the grain boundary density of defect states and can vary widely in polycrystalline CdTe. Mueller[55] has determined γ for Ge *bicrystal* grain boundaries by observing the difference in current between a measurement across a grain boundary, versus a measurement from the bulk to the grain boundary. The latter measurement is not easy to perform. However, a measurement similar to Mueller's may be possible for polycrystalline materials by using a scanning tunneling microscope technique developed by Ballif et al.[56] Mueller's results show that γ is in the range of 0.2 to 0.6 for the Ge bicrystals, and increases with increasing grain boundary misfit angle. Spencer[50] has calculated γ to be less than 0.2 on a GaAs bicrystal from measurements of the grain boundary charge density and the capture cross-sections for the grain boundary

states. The effects of different values of γ for CdTe grain boundaries will be evaluated in the results chapter.

The current-voltage relation given in equation (3.1) neglects the minority carrier contribution to the total current across the grain boundary. The minority carrier current can be approximated by using theory analogous with a Schottky barrier diode or a one sided, long based diode to describe the injection of excess minority carriers into the intra-grain quasi-neutral region. This analogy is better understood by considering the inverted grain boundary as shown in Figure 3.1, where the grain boundary forms the n-side of a pn-junction in either direction. When modified to reflect grain boundary parameters, the one-sided, long-based diode J_0 becomes:[57]

$$J_0^n = \frac{qn_i^2\sqrt{\frac{kT}{q}\mu_n}}{N_b\sqrt{\tau_n}} \qquad A/cm^2 \qquad (3.3)$$

where, μ_n and τ_n are the electron mobility and lifetime, respectively. N_b and n_i are the grain's doping density and intrinsic carrier concentration, respectively, in the region adjacent to the grain boundary. Using values which are typical for bulk CdTe,[31] $n_i \approx 6\text{x}10^5$ cm^{-3}, μ_n=100 cm^2/V-s, and approximating the bulk τ_n with the large grained polycrystalline value of 5 ns as given in Figure 1.7(b), results in a maximum value of $J_0^n = 0.002/N_b$. Thus, if N_b is approximated with a typical bulk value of 10^{15} cm^{-3}, then $J_0^n = 2\text{x}10^{-18}$ A/cm^2. This value of J_0^n is negligible compared to values of J_0 for majority carriers (see subsequent section 3.2).

The derivation of equation (3.1) also neglects the effects of carrier generation and recombination from the grain boundary space-charge region. However, CdTe materials tend to be highly compensated, and contain a large number of native defect states. Materials with a larger number of mid-gap states would have smaller bulk carrier lifetimes, which could increase the generation-recombination current. Thus, the significance of the current due to generation-recombination must be considered. Using a one-sided pn-junction to describe one side of the grain boundary as before, then one side of the grain boundary is treated as a forward-biased one-sided pn-junction, while the other side is treated with a reverse-bias. Since a forward-biased one-sided pn-junction gives a net recombination, while the reverse biased one-sided pn-junction gives a net generation, then the overall current due to generation-recombination is equal to the difference between the forward and reverse-biased sides. However, the reverse-bias generation current is negligible compared to the forward-biased recombination current for a small applied biases.[58] A rigorous analysis of recombination in forward-biased and one-sided pn-junctions has been developed by Shur.[58] The saturation current from Shur's analysis, modified to reflect grain boundary parameters, is given as:

$$J_0^{gr} = \frac{n_i qkT}{2\tau}\sqrt{\frac{\pi\varepsilon_s}{4qN_b V_{b0}}} \qquad A/cm^2 \qquad (3.4)$$

where here τ is equal to $(\tau_n \tau_p)^{1/2}$ with τ_n and τ_p being the electron and hole "bulk" carrier lifetimes respectively, ε_s is the low frequency bulk material permittivity, and qV_{b0} is the zero-bias band bending. In equation (3.4), V_{b0} is assumed to be much greater than the

applied voltage and equal to the "built in" voltage. As earlier, the "bulk" lifetimes will be approximated by the large grained polycrystalline CdTe value of 5 ps. Using typical bulk values of $\varepsilon_s = 10.9\varepsilon_0$,[31] where ε_0 is the permittivity of free space, 10^{15} cm^{-3} for N_b, and using a mid-gap CdTe value of 0.75 eV for qV_{b0}, then this gives $J_0^{gr} \approx 3 \times 10^{-11}$ A/cm^2. This value of J_0^{gr} is comparable to values of J_0 from drift-diffusion and thermionic emission when using these same values of N_b and qV_{b0} (see subsequent section 3.2). However, the generation-recombination current is dependent on $N_b^{-1/2}$. If N_b is large in the grain boundary space-charge region, $N_b = 10^{17}$ cm^{-3} for example, then generation-recombination would be negligible. Thus the significance of generation-recombination will be addressed again after values of N_b have been determined in the results chapter. The primary factor affecting the temperature dependence of J_0^{gr} is n_i, since $n_i \propto [\exp(-E_g/kT)]^{1/2}$. This temperature dependence results in an activation energy of about $\frac{1}{2}E_g$. Since the bandgap of CdTe is about 1.5 eV, then this gives a J_0^{gr} an activation energy of 0.75 eV.

3.2 Models for Conduction Across Grain Boundary Barriers

Current conducted across grain boundary barriers is possible by several mechanisms, which depend on the doping density in the region adjacent to the grain boundary. As shown in Figure 3.2, drift and diffusion conduction dominates at low doping densities, thermionic emission dominates at intermediate doping densities, and thermally assisted tunneling or tunneling dominates at high doping densities. Each of these mechanisms has a different temperature dependence, which is contained within the saturation current factor and discussed below.

3.2.1 Combined Drift-Diffusion and Thermionic Emission Theory

Crowell and Sze[59] developed a current conduction model for Schottky barriers that combines drift-diffusion theory with thermionic emission theory. The saturation current from this combined theory can be written in terms of N_b and V_{b0} as:

$$J_0^{ddt} = \frac{q f_P f_Q N_b}{\frac{1}{\upsilon_d} + \frac{1}{f_P f_Q \upsilon_r}} \exp\left(-\frac{q(V_{b0} - \Delta V_b)}{kT}\right) \quad A/cm^2 \qquad (3.5)$$

where N_b and V_{b0} are as defined earlier, ΔV_b is the image force barrier lowering potential, and v_d and v_r are the effective diffusion velocity due to drift-diffusion carrier transport and the "recombination velocity" due to thermionic emission carrier transport, respectively. The factors f_P and f_Q correspond to the degree of phonon backscattering and quantum mechanical reflection at the top of the barrier respectively, and have values between 0 and 1. Crowell and Sze have determined that $f_P f_Q \cong 0.5$ over a wide range of electric fields and materials where drift-diffusion or thermionic emission transport is dominant.

The diffusion velocity in equation (3.5) can be approximated from the value of the maximum electric field at the barrier, ξ_{max}, or:

$$v_d = \mu \xi_{\max} \quad cm/s \qquad (3.6)$$

where μ is the majority carrier mobility. For the grain boundary double depletion region and small applied bias, ξ_{max} can be expressed in terms of N_b and V_{b0} and is given as:

$$\xi_{max} = \sqrt{\frac{2qN_b V_{b0}}{\varepsilon_s}} \qquad V/cm \tag{3.7}$$

As an example, $v_d \approx 10^6$ cm/s, using previously mentioned CdTe values for ε_s, μ_p, and $N_b = 10^{15}$ cm^{-3}, and $qV_{b0} = 0.75$ eV.

An expression for v_r for carriers thermally emitted over the barrier can be found from thermionic emission theory and given as:

$$v_r = \sqrt{\frac{kT}{2\pi m^*}} \qquad cm/s \tag{3.8}$$

Thus, v_r is a constant of the material and dependent on the majority carrier effective mass, m^*. This gives $v_r = 4.5 \times 10^6$ cm/s as a typical value for CdTe using $m_p^* = 0.35m_0$,[31] for holes, where m_0 is the mass of an electron in vacuum.

From equation (3.5) it can be seen that if $f_P f_Q v_r$ is much smaller than v_d, then the current flow is mostly described by thermionic emission. Conversely, if v_d is much smaller than $f_P f_Q v_r$, then the current flow is described by drift-diffusion. The form of equation (3.5) suggests that the two conduction mechanisms occur in series, such that the limiting conduction mechanism describes the current flow. For the values of N_b and qV_{b0} used above v_d is about ½ of $f_P f_Q v_r$, and drift-diffusion would be the limiting process. However, if N_b is much higher than the bulk value of 10^{15} cm^{-3}, then thermionic emission would become the limiting process. For $qV_{b0} = 0.75$ eV, v_d is approximately equal to v_r

when $N_b = 4 \times 10^{15}$ cm^{-3}. Again, the actual values of N_b and V_{b0} will be determined from a fit to the data.

The image force barrier lowering effect, ΔV_b, is neglected in the calculation of v_d as this factor is not significant when v_d becomes less than v_r. However, ΔV_b may be significant in the exponential term of equation (3.5). The magnitude of the image force barrier lowering can be approximated by:[49]

$$\Delta V_b = \sqrt{\frac{q\xi_{\max}}{4\pi\varepsilon_s}} \qquad V \tag{3.8}$$

Thus, $q\Delta V_b$ = 15 meV using previously stated values of $N_b = 10^{15}$ cm^{-3} and qV_{b0} = 0.75 eV. This value of $q\Delta V_b$ is small, but if N_b is large for example; $N_b = 10^{17}$ cm^{-3}, then $q\Delta V_b$ = 47 meV and is thus significant.

The primary temperature dependence of J_0^{ddt} comes from the exponential factor in equation (3.5). Thus J_0^{ddt} increases approximately exponentially with increasing temperature, and has an activation energy of about $q(V_{b0} - \Delta V_b)$. However, the relative magnitudes of v_d and v_r are temperature dependent. The temperature dependence of v_d comes from the temperature dependence of the mobility. At room temperatures or higher then μ is dominated by lattice scattering, which has a $T^{-3/2}$ dependence for a semiconductor.[60] The temperature dependence of v_r can be determined from equation (3.8) and is $T^{1/2}$. Thus, as the temperature increases, v_d decreases while v_r increases. This indicates that the limiting conduction mechanism may change from thermionic emission to drift-diffusion with increasing temperatures, depending on the value of ξ_{max}.

A preliminary value of J_0^{ddt} can be determined using equation (3.5). Using typical values of μ_p, m_p*, ε_s for bulk CdTe as given earlier, along with $N_b = 10^{15}$ cm^{-3} and qV_{b0} = 0.75 eV, results in $J_0^{ddt} \approx 2 \times 10^{-11}$ A/cm^2 at room temperature. This result confirms $J_0^{ddt} >> J_0^n$ and that the minority carrier current can be neglected in equation (3.1). Using $N_b = 10^{17}$ cm^{-3}, then J_0^{ddt} increases by three orders of magnitude to $\approx 2 \times 10^{-8}$ A/cm^2 at room temperature, and generation-recombination currents become negligible.

3.2.2 Thermally-Assisted Tunneling Theory

In the event of very narrow potential energy barriers, carriers can "pass through" the barrier via quantum mechanical tunneling. The zero-bias depletion width of one side of the grain boundary barrier region as shown in Figure 3.1, is found from Poisson's equation in the abrupt approximation and given as:

$$x_d = \sqrt{\frac{2\varepsilon_s V_{b0}}{qN_b}} \qquad cm \tag{3.9}$$

For a given V_{b0}, x_d decreases when the doping in the region adjacent to the grain boundary increases. When x_d becomes thin enough ($\approx$ 100 Å), then tunneling is possible through the bottom of the barrier. However with thicker depletion widths or lower levels of doping, tunneling is possible with thermal assistance up to the thin part of the energy barrier (refer to Figure 3.1). Thus, thermally-assisted tunneling effects must be considered when doping levels become moderate. Two types of thermally-assisted tunneling are considered herein: 1) a one-step tunneling process in which the carriers are thermally excited up to a thin part of the parabolic barrier;[51,61] 2) a two-step tunneling

process in which the carriers are thermally excited up to a point where the barrier is thin enough to tunnel to grain boundary defect states, and from there tunnel to the band edge on the far side of the barrier. For V_{b0} = 1.0 eV, Figure 3.1 indicates that the thermally-assisted tunneling effect becomes significant beyond a doping level of 10^{17} cm^{-3}.

Tunneling through the bottom of barrier without thermal assistance can occur either directly or via intra-gap defect states.[62,63,64] This type of tunneling is mostly independent of temperature, and any temperature dependence comes via V_{b0} through the temperature dependence of E_g. The temperature dependence of V_{b0} is discussed further in section (3.2.4). Tunneling through the bottom of the barrier will not be considered herein as experimental evidence shows that the current from the samples herein is thermally activated in the range 300-400°K.

The calculation for the thermally-assisted tunneling current through an energy barrier will start with a general tunneling expression from Harrison[65] for the net current from one side, 1, of the barrier to the other side, 2, or $J = J_{1\to2} - J_{2\to1}$, and given as:

$$J = \frac{q8\pi^2}{h} \sum_{k_t} \int_{-\infty}^{\infty} |M_{12}|^2 N_1(E) N_2(E) [f_1(E) - f_2(E)] dE \qquad A/cm2 \qquad (3.10)$$

where h is the Planck constant, q is the charge of an electron the summation is over transverse momentum, k_t, E is the total carrier energy, M_{12} is the matrix element for the transition from side one to side two, $N_1(E)$ and $N_2(E)$ are the density of states on side one and side two, respectively and $f_1(E)$ and $f_2(E)$ are the occupancy factors.

3.2.2.1 One-Step Thermally-Assisted Tunneling

Crowell and Rideout[66] developed a current conduction model for Schottky barriers, which accounts for thermally-assisted tunneling. This model covers the full range of thermally-assisted tunneling from nearly thermionic emission to tunneling through the bottom of the barrier, however some of the approximations used begin to break down at these limits. The current for this model can be derived from equation (3.10) and is written as follows:

$$J = \frac{A^* T}{k} \int_0^{\infty} T(E_p)\{f_1(E_p) - f_2(E_p)\}dE \qquad A/cm^2 \qquad (3.11)$$

where A^* is the Richardson constant equal to $4\pi qm^*k^2/h^3$, and f_1 and f_2 are now the Boltzmann occupancy functions for the high energy process. Equation (3.11) was derived by using the semiconductor density of states for $N_1(E)$ and $N_2(E)$, and integrating over all transverse momentum states. The integration is accomplished by first interchanging the order of integration in equation (3.10), then transforming the integration from transverse momentum to an integration over E - E_p. $T(E_p)$ is the transmission probability for tunneling through the energy barrier for a carrier with energy E_p in the direction perpendicular to the barrier, and is found from the matrix element assuming a isotropic effective mass m^*. The effective mass of polycrystalline CdTe is taken to be isotropic due to its cubic structure.[67] An isotropic effective mass simplifies the analysis, which would otherwise have to account for the directional dependence of the mass in the integral. For the one-step band-to-band transition the matrix element of

equation (3.10) can be evaluated using traveling wavefunctions for both sides of the barrier, an exponentially decaying wavefunction inside of the barrier, and using the WKB approximation[66,68,69] by assuming a slowly varying barrier potential energy as a function of position.[70] With this matrix element for the one step process, *T(E)* has been found for Schottky barriers and is given as:

$$T(E_p) \cong \exp\left(-\frac{4\pi}{h} \int_{x_1}^{x_2} \left[2m^* \left(qV(x) - E_p \right)^{1/2} \right] dx \right) \tag{3.12}$$

where the x-direction is perpendicular to the barrier, x_1 is a classical turning point, or the position x when $E = qV(x)$, and x_2 is the position of the barrier maximum. $V(x)$ is the barrier potential energy assuming uniform doping in the barrier depletion region and is found from Poisson's equation for an abrupt junction as:

$$V(x) = \frac{qN_b x^2}{2\varepsilon_s} \qquad V \tag{3.13}$$

for x between 0 and x_2. The WKB assumption of a slowly varying barrier potential energy is not unreasonable when $V(x) \propto x^2$. In the limit of small applied bias, Seager and Pike[60] have commented that for back-to-back parabolic barriers the exponent in *T(E)* is just twice that for Schottky barriers, and can be evaluated analytically for the potential given in equation (3.13):

$$T(E) \cong \exp\left(-\frac{2qV_b}{E_{00}} \left\{ \sqrt{\left[1 - \frac{E}{qV_b} \right]} - \frac{E}{qV_b} a\cosh\left[\sqrt{\left(\frac{qV_b}{E} \right)} \right] \right\} \right) \tag{3.14}$$

E_{00} is a constant of the material that is proportional to the square root of N_b and can be expressed as:

$$E_{00} = \frac{qh}{4\pi}\sqrt{\left(\frac{N_b}{m^* \varepsilon_s}\right)} \qquad eV \tag{3.15}$$

Two other approximations are contained within the current equation given as equation (3.11). Due to the high energies of carriers in thermally-assisted tunneling the energy dependence of the density of states is removed from the integrand and contained within A^* as the density of states is approximately constant for the high-energy process. This approximation will become invalid when most of the carrier tunneling is near the bottom of the barrier. Also, a parabolic energy-momentum relationship is assumed with no mixing of valence and conduction band states. Thus, $qV_{b0} - E_m$, must be less than $\frac{1}{2}E_g$ or the carrier may possess some conduction band character during tunneling.[71] The validity of these approximations are to be determined.

Crowell and Rideout[66] were able to derive an approximate analytical solution to the current given in equation (3.11) by fitting the product $T(E_p)\{f_1(E_p)-f_2(E_p)\}$ to a Gaussian distribution which matches the maximum in the energy distribution of transmitted carriers, E_m, and curvature centered around E_m. This same approach can be applied to the back-to-back parabolic barriers, with $T(E_p)$ as given in equation (3.14), and is described in detail in Appendix B. The resulting Gaussian can then be integrated, and gives J_0 for the one-step thermally-assisted tunneling process as:

$$J_0^{1s} \cong \frac{A^*T}{k} \frac{E_{00}\sqrt{\pi(qV_{b0})}}{\sqrt{E_{01}}\cosh\left(\frac{E_{00}}{2kT}\right)} \exp\left(-\frac{E_{vf}}{kT}\right)\exp\left(-\frac{2qV_{b0}}{E_{01}}\right) \quad A/cm^2 \qquad (3.16a)$$

with:

$$E_{01} = E_{00}\coth\left(\frac{E_{00}}{2kT}\right) \qquad eV \qquad (3.16b)$$

E_{vf} is the position of the Fermi level in the bulk, as shown in Figure 3.1, and can be expressed in terms of E_{00} as follows:

$$E_{vf} = -kT\ln\left[\left(\frac{4\pi E_{00}}{qh}\right)^2 \frac{m^*\varepsilon_s}{N_v}\right] \quad eV \qquad (3.16c)$$

where N_v is the bulk material effective density of states.

The temperature dependence of the one-step thermally-assisted tunneling process is evident by inspection of equation (3.16). At room temperature and above E_{01} can be replaced by $2kT$ for CdTe and values of N_b less than 10^{18} cm^{-3}. Thus, the major temperature dependence of thermally assisted tunneling comes from V_{b0}/E_{01} in the exponential term. For values of N_b larger than 10^{20} cm^{-3} or when tunneling becomes dominant, then $E_{00} >> 2kT$ and E_{01} can be replaced by E_{00}. The result is a nearly temperature independent current-voltage expression, with only a slight temperature dependence coming primarily from the temperature dependence of V_{b0}. The temperature dependence of V_{b0} is discussed further in section (3.2.4).

3.2.2.2 Two-Step Thermally-Assisted Tunneling

If the density of grain boundary defect states is sufficiently high, then thermally-assisted tunneling through the grain boundary barrier via defect states may be more probable than the previously described one-step process. For the band to defect transition, the matrix element can be modeled following the approach of Sarrabayrouse[72] by assuming a delta function potential for the defect at the grain boundary.[73] The amplitude of the delta function is obtained from the solution to Schrodinger's equation at the position of the defect using a wavefunction for a three-dimensional square well potential.[74] The density of defect states at the grain boundary is treated as an exponentially increasing function of energy toward the valence band-edge, as measured from CdTe bicrystals,[23] or:

$$N_{ta}(E) = N_{ti} \exp\left(\frac{E}{E_{ta}}\right) \qquad eV^{-1}\,cm^{-2} \tag{3.17}$$

where N_{ti} is the grain boundary density of defect states at mid-gap, and E_{ta} is the characteristic energy describing the exponentially increasing density of acceptor states. As an example, the average values for the CdTe bicrystals measured by Thorpe et. al.[23] are N_{ti}= 10^{12} cm^{-2} eV^{-1} and E_{ta} = 0.25 eV.

As before, the order of integration in equation (3.10) is interchanged, and the integration over transverse momentum is transformed to an integration over E-E_p. This results in the following current equation for band-state to defect-state tunneling:

$$J = \frac{4\pi q N_{ti}}{h} \int_0^{\infty} dE_p \int_{E_p}^{\infty} T_d(E, E_p)\{f_1(E) - f_2(E)\} \exp\left(\frac{E}{E_{ta}}\right) dE \quad A/cm2 \qquad (3.18)$$

where $T_d(E,E_p)$ is the transmission probability for the band-state to defect-state transition and is given by:

$$T_d(E, E_p) \cong \left(\frac{qV_b - E}{qV_b - E_p}\right)^{1/2} \exp\left(-2\frac{4\pi}{h}\int_{x_1}^{x_2}\left[2m^*\left(qV(x) - E_p\right)^{1/2}\right]dx\right) \qquad (3.19)$$

Equation (3.19) can be simplified by approximating $E \cong E_p$ for the high-energy thermally-assisted tunneling process. Thus $T_d(E,E_p) \cong T_d(E_p) = T(E_p)$, as given by equation (3.12) and without the factor of two in the exponent of equation (3.14). After the integration over E in equation (3.18) assuming f_1 and f_2 are the Boltzmann occupancy functions, the current between the band edge and the grain boundary defect states can be written as:

$$J = \frac{4\pi q N_{ti}}{h}\left(\frac{1}{kT} - \frac{1}{E_{ta}}\right)^{-1}\int_0^{\infty} T_d(E_p)\{f_1(E_p) - f_2(E_p)\}\exp\left(\frac{E_p}{E_{ta}}\right)dE_p \quad A/cm^2 \qquad (3.20)$$

If the product $T_d(E)\{f_1(E)-f_2(E)\}\exp(E/E_t)$ is fit to a Gaussian distribution as done in the previous section, and described in detail in Appendix B, then the saturation current can be found as:

$$J_0^{2s} \cong \frac{4\pi q N_{ti}}{h}\left(\frac{1}{kT}-\frac{1}{E_{ta}}\right)^{-1}\frac{E_{00}\sqrt{4\pi(qV_{b0})}}{\sqrt{E_{02}}\cosh\left(\frac{E_{00}}{kT}-\frac{E_{00}}{E_{ta}}\right)}\exp\left(-\frac{E_{vf}}{kT}\right)\exp\left(-\frac{qV_{b0}}{E_{02}}\right)$$

A/cm^2 (3.21a)

with:

$$E_{02} \cong E_{00}\coth\left(\frac{E_{00}}{kT}-\frac{E_{00}}{E_{ta}}\right) \qquad eV \qquad (3.21b)$$

For a constant density of grain boundary energy states, then the above equations can be used with $E_{ta} = \infty$ or $N_t(E) = N_{ti}$. . During the fitting, N_{ti} is eliminated from equation (3.21a) using an equation for the conservation of charge at the grain boundary region or:

$$\sqrt{\frac{8\varepsilon_s N_b V_{b0}}{q^2}} = \int_{E_v}^{E_c} N_{td}(E)\left[1-f(E,E_f)\right]dE - \int_{E_v}^{E_c} N_{ta}(E)\left[f(E,E_f)\right]dE \quad \text{C/cm}^2 \qquad (3.22)$$

which states that the total charge at the grain boundary, right-hand side of eqn. (3.22), equals the total opposite charge in the surrounding grain boundary space-charge regions, left-hand side of eqn (3.22). In equation (3.22), $N_{ta}(E)$ is as given in equation (3.17), and $N_{td}(E)$ is the equivalent density of grain boundary states equation for donors. Here also, $N_{td}(E)$ is assumed to be exponentially increasing density of states with a characteristic energy of E_{td} as determined by Thorpe et. al.[23] Thus, the right-hand side of equation (3.22) is just the total ionized donors at the grain boundary (positive charge), minus the total ionized acceptors at the grain boundary (negative charge). The left-hand side of equation (3.22) can be found from Poisson's equation for the double-sided space-charge

region of the grain boundary. By anticipating that the biggest contributions to the integrals in equation (3.22) come when $(E - E_f) >> kT$, or $(E_f - E) >> kT$ for the exponentially increasing density of grain boundary states, then Boltzmann's approximation can be used for the occupancy functions. Also, by neglecting insignificant terms that show up after the integration, equation (3.22) becomes:

$$\sqrt{\frac{8\varepsilon_s N_b V_{b0}}{q^2}} = N_{ti}\left[E_{td}\exp\left(\frac{E_c - E_f}{E_{td}}\right) - E_{ta}\exp\left(\frac{E_f - E_v}{E_{ta}}\right)\right] \quad \text{C/cm}^2 \quad (3.23)$$

From here, $(E_c - E_f)$ is replaced by $(E_g - V_{b0} - E_{vf})$, and $(E_f - E_v)$ can be replace by $(V_{b0} + E_{vf})$. Then equation (3.23) is solved for N_{ti}, and the resulting expression is plugged back into equation for J_0^{2s} and used for fitting to the current versus temperature data. The fitting parameters for the two-step thermally-assisted tunneling model are V_{b0}, E_{00}, E_{ta}, and E_{td}. Since there is a wide range of combinations of E_{ta} and E_{td} that yield good fits, then these values were limited to the range found for several bicrystals as measured by Thorpe et. al. For E_{ta} the range was found to be 0.1 – 0.4 eV, and for E_{td} the range was found to be 0.05 – 0.3 eV.[23] Fortunately, the effects of variable values of E_{ta} and E_{td} on the resultant fitted values of V_{b0} and E_{00} is very small, since E_{ta} is systematically varied while E_{td} is left as a fitting parameter. The sensitivity of the fits to E_{ta} and E_{td} will be discussed in greater detail in the results chapter.

The temperature dependence of the two-step thermally-assisted tunneling process can be found by inspection of equation (3.21). At room temperature and above E_{02} can be replaced by $[(1/kT)-(1/Et)]^{-1}$ for CdTe and values of N_b less than 10^{18} cm^{-3}. Thus, the major temperature dependence of thermally assisted tunneling comes from V_{b0}/E_{02} in the

exponential term. For values of N_b larger than 7 x 10^{19} cm^{-3} or when tunneling becomes dominant, then $E_{00} >> [(1/kT)-(1/Et)]^{-1}$ and E_{02} can be replaced by E_{00}. The result is a nearly temperature independent current-voltage expression, with only a slight temperature dependence coming primarily from the temperature dependence of V_{b0}. The temperature dependence of V_{b0} is discussed further in section (3.2.4).

On a final note for the two-step thermally-assisted tunneling model, γ in equation (3.1) has no meaning for the two-step tunneling process, and is set to zero during fitting.

3.2.3 Energy Distribution of Transmitted Carriers from Thermally-Assisted Tunneling

The maximum in the energy distribution of transmitted carriers, E_m, is determined by the value of E_{00}, which depends on the doping density, and temperature according to:

$$\frac{E_m}{qV_{b0}} = \cosh^{-2}\left(\frac{E_{00}}{2kT}\right) \tag{3.24a}$$

for the one-step thermally-assisted tunneling process, and:

$$\frac{E_m}{qV_{b0}} = \cosh^{-2}\left(\frac{E_{00}}{kT} - \frac{E_{00}}{E_{ta}}\right) \tag{3.24b}$$

for the two-step thermally-assisted tunneling process. The transmission rate, normalized to E_m for the *two-step* thermally-assisted tunneling process, is plotted against the normalized barrier height for several example values of E_{00} and kT as shown in Figure 3.3. This figure illustrates the energy distribution of transmitted carriers in dimensionless

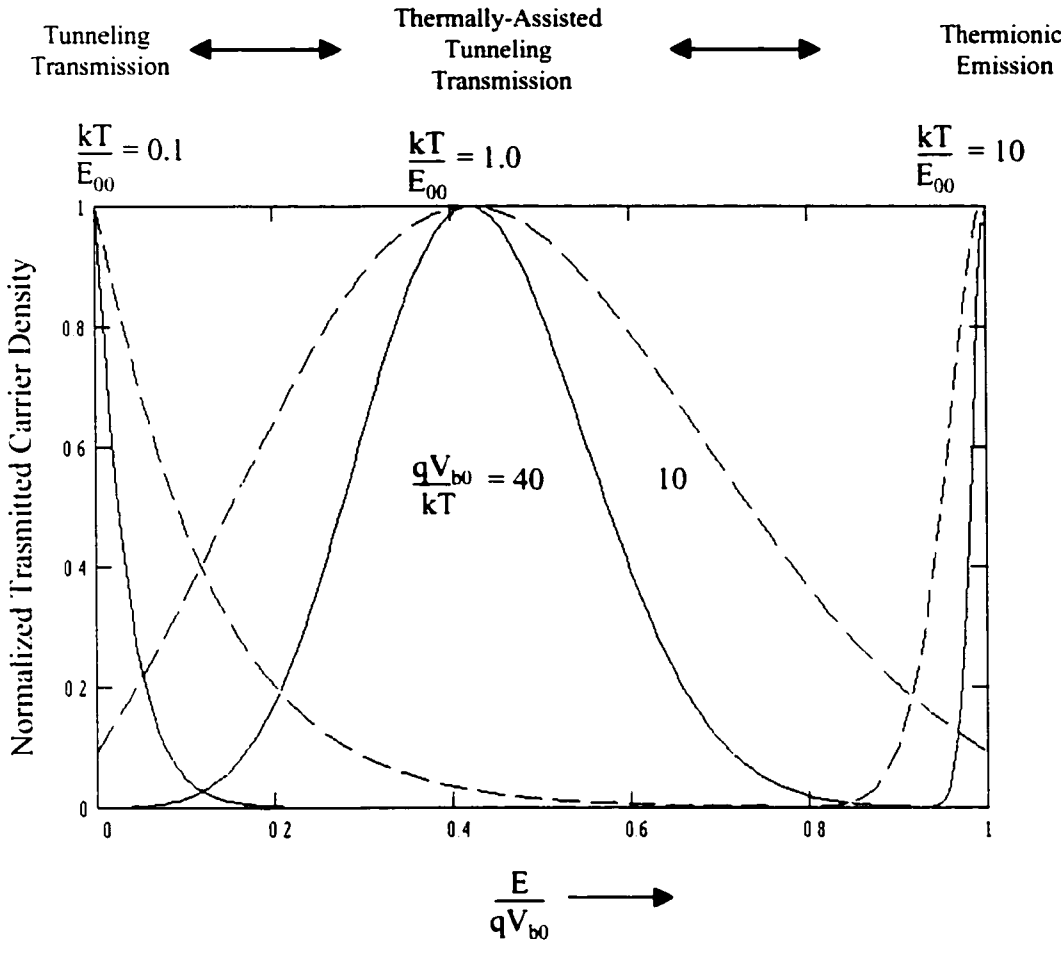

Figure 3.3 **Normalized energy and transmitted carriers distributions for selected values of kT/E_{00} and the semiconductor band bending qV_{b0} in units of kT for the two-step thermally-assisted tunneling process. $E_{ta} >> kT$ is assumed. Solid lines are for $qV_{b0}/kT = 40$ and dashed lines are for $qV_{b0}/kT = 10$.**

units. As can be seen from the figure, when E_{00} is large compared to kT, then emission is through the bottom of the band and is primarily tunneling only. When E_{00} is small compared to kT, then the carriers are emitted over the top of the barrier or thermionic. However, when E_{00} is comparable to kT, then transmission is dominated by thermally-assisted tunneling. Thus, the value of E_{00} indicates which process is dominant. The

figure also shows that taller barrier heights give smaller spreads in the energy distribution of transmitted carriers.

3.2.4 Temperature Dependence of the Bandgap

The temperature dependence of the CdTe band-gap is linear and has been measured to be approximately -3.2×10^{-4} eV/°K.[75,76] Part of this dependence can be attributed to the absolute change in energy of the valence band, and consequently may influence the grain boundary barrier potential. As an approximation, if one half of the band-gap temperature dependence is assigned to dV_{b0}/dT, then V_{b0} decreases by only 16 meV with a 100 °K increase. The resultant increase in saturation current due to dV_{b0}/dT is 50%, when using the thermionic emission theory presented in equation (3.4) with $N_b = 10^{17}$ cm^{-3} and V_{b0} = 0.75 eV at 300 °K. This represents only a small fraction of the total change in current predicted by the conduction models presented herein. The approximation of $dV_{b0}/dT = \frac{1}{2}\, dE_g/dT$ will be used in the temperature dependent theoretical fits to the data.

3.2.5 Grain-Boundary Barrier Height Inhomogeneity Theory

The grain-boundary conduction analysis up to this point does not account for the variable grain-boundary barrier heights in polycrystalline material. For inhomogeneous barrier heights the current is presumed to tend toward the paths with lower barrier heights. The influence of the barrier height inhomogeneity was theoretically developed by Werner and the effects were discussed in section 2.2.4. To model the effects Werner employed a statistical analysis using a Gaussian distribution of grain boundary potentials as given below:[52,53]

$$P(V_{b0}) = \frac{1}{\sigma_s \sqrt{2\pi}} \exp\left(- \frac{(V_{bm} - V_{b0})^2}{2\sigma_s^2} \right) \tag{3.25}$$

where V_{bm} is the mean zero bias band bending, and σ_s is the standard deviation. If the saturation current can be expressed as:

$$J_0 = C \exp\left(\frac{-qV_{b0}}{kT}\right) \quad A/cm^2 \tag{3.26}$$

where C is a constant, then the effective V_{b0}, or V_{beff}, can be found from:

$$\exp\left(-\frac{qV_{beff}}{kT}\right) = \int_{-\infty}^{\infty} \exp\left(-\frac{qV_{b0}}{kT}\right) P(V_{b0}) dV_{b0} \tag{3.27}$$

using the expression for $P(V_{b0})$ from equation (3.25) in (3.27). This results in the following relation:

$$V_{beff} = V_{bm} - \frac{q\sigma_s^2}{2kT} \quad V \tag{3.28}$$

This expression is then used in place of V_{b0} for the current versus temperature analysis. Thus, σ_s is now the additional unknown in the fitting of the temperature dependent data. Werner states that the inhomogeneity analysis is valid for any quantity that is thermally activated according to the form of equation (3.26). Consequently, Werner's treatment can only be strictly applied to the combined drift-diffusion and thermionic emission saturation conduction theory given by equation (3.5). The thermally-assisted tunneling saturation current of equations (3.16a) and (3.21a) do not quite fit the form of equation

(3.26). However, equations (3.26-3.28) be modified to approximate the thermally-assisted tunneling case by replacing kT with E_0. This is possible if E_{00} is not too large, since most of the temperature dependence comes from the exponential containing V_{b0}. The effects grain boundary inhomogeneities will be evaluated herein.

3.2.6 Saturation Current as a Function of Temperature

Figure 3.4 summarizes the temperature dependence in the range of 300-400°K for the various types of saturation current as modeled in this chapter. Two different values of doping adjacent to the grain boundary (N_b), are used for each type of saturation current, with $N_b = 10^{15}$ cm^{-3} for Fig. 3.4(a) and $N_b=10^{17}$ cm^{-3} for Fig. 3.4(b). A zero bias band bending of $V_{b0} = 0.75$ eV is assumed in both (a) and (b). Also, uniform barrier heights or $\sigma_s=0$ was assumed, and the values of $N_{ti}= 10^{12}$ cm^{-2} eV^{-1} and $E_{ta} = 0.1$ eV was used for J_0^{2s}.

All current models, except for J_0^n, indicate 3-4 orders of magnitude increase in current due to increasing the temperature from 300°K to 400°K and when neglecting the temperature dependence due to the small applied voltage. This current increase is consistent with knowledge gained a posteriori for CdTe grain boundaries. As discussed earlier in section 3.1, the minority carrier saturation current, J_0^n is negligible at these temperatures when compared to the majority carrier conduction mechanisms J_0^{ddt}, J_0^{1s}, and J_0^{2s}. Also as discussed earlier in section 3.1, the saturation current due to generation-recombination, J_0^{gr}, decreases at the higher doping densities, see Fig. 3.4(b). Lastly, using the grain boundary density of defect states as measured by Thorpe,[23] then the two-step thermally-assisted tunneling model, J_0^{2s}, yields the highest current at both doping densities.

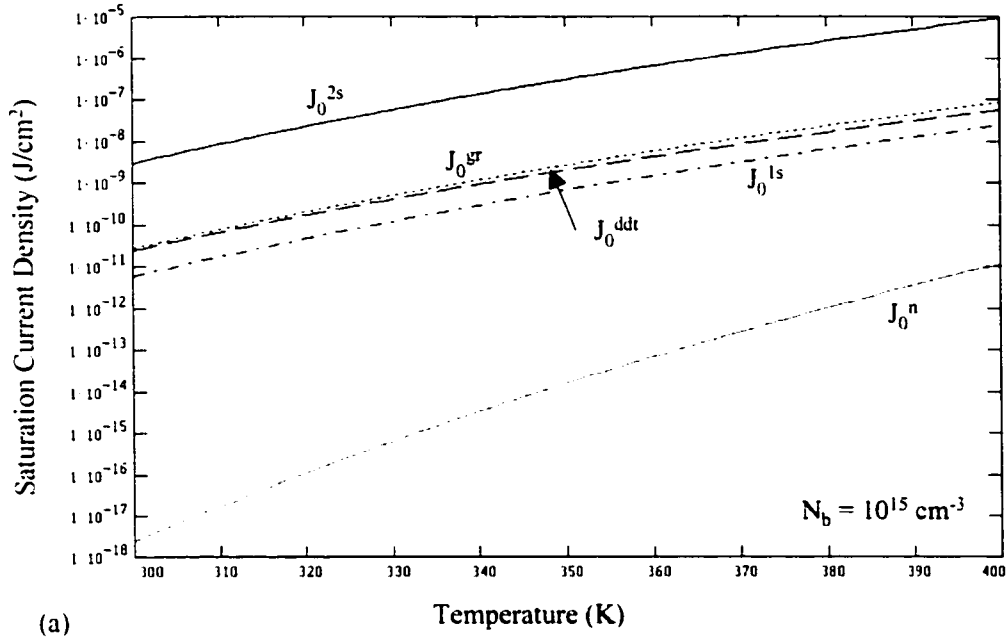

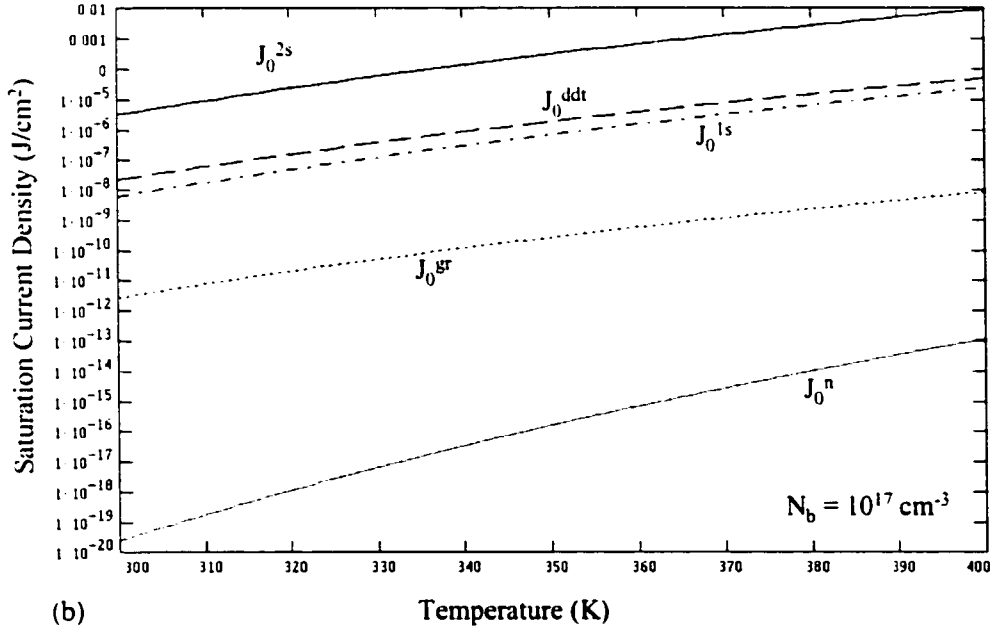

Figure 3.4 **Temperature dependence for the various types of saturation current as modeled in this chapter., $N_b = 10^{15}$ cm^{-3} is assumed in (a), and N_b=10^{17} cm^{-3} is assumed (b). A zero bias band bending of V_{b0} = 0.75 eV is used in both (a) and (b). Also, uniform barrier heights or $\sigma_s = 0$ was assumed, and the values of N_{ti}= 10^{12} cm^{-2} eV^{-1} and E_{ta}= 0.1 eV was used for J_0^{2s}.**

3.3 Bicrystal Barrier Height Measurements: Technique Comparison

In this dissertation, several grain boundary parameters will be determined from theoretical fitting of current vs. temperature data. As discussed in chapter 2, capacitance techniques can be used to obtain grain boundary information from bicrystals. Thus, bicrystals can be used to compare measurement techniques. Using bicrystals with low bulk doping levels, some studies have already demonstrated a correlation between barrier heights, as derived from fitting temperature-dependent data with thermionic emission theory, and barrier heights as derived from zero bias capacitance or capacitance-voltage data.[23,51] A similar comparison can be done on highly doped bicrystals using thermally-assisted tunneling theory.

Bicrystal data was used to compare the grain boundary barrier heights derived from the thermally-assisted tunneling theory with barrier heights derived from zero bias capacitance measurements described in chapter 2. The thermally-assisted tunneling theory presented in this chapter was fit to data from a study on GaAs bicrystals by Pike and Seager.[51] The fitting was performed using Peakfit software and as described in Chapter 4 (later). Two bicrystals were used in the study by Pike and Seager, and the bulk doping was measured from Hall measurements as 4.6×10^{17} cm^{-3} for bicrystal A, and 2.0×10^{18} cm^{-3} for bicrystal B. In addition, grain boundary barrier heights were determined from the measured zero bias capacitance and equation (2.4) and given as 0.73 eV and 0.83 eV for bicrystals A and B respectively. Thus, according to Figure 3.2, the measured doping and barrier heights from this study suggest thermally-assisted tunneling as the most likely conduction mechanism across the grain boundaries for both of these bicrystals.

In order to fit the data given by Seager and Pike, the small signal, ($qV << kT$), conductance versus inverse temperature data was converted to current versus temperature by assuming an applied voltage of 1 mV. During the fitting an isotropic effective mass was assumed, with $m^* = 0.068$, $\varepsilon_r = 13.2$, and $N_c = 1.1\text{x}10^{18}$ cm^{-3} as the GaAs material characteristics.[57] Figure 3.5 shows the data for the two bicrystals and the resultant fits using the one-step thermally-assisted tunneling model, and the combined drift-diffusion/thermionic emission model with N_b limited to $1\text{x}10^{17}$ cm^{-3}. This is the approximate value at which drift-diffusion/thermionic emission is no longer physically valid for a given barrier height. Bicrystal A is shown in the plot at the top of the figure, and bicrystal B is shown on the bottom. Without considering the possibility of grain boundary inhomogeneity for the moment (σ locked at 0 meV), the one-step thermally-assisted tunneling model gives the best fit to both bicrystals. The fit using the one-step thermally-assisted tunneling model yields $V_{b0} = 552$ meV, and $N_b = 7.9\text{x}10^{15}$ cm^{-3} ($E_{00} = 1.7$ meV) for bicrystal A, and $V_{b0} = 1110$ meV, and $N_b = 4.0\text{x}10^{19}$ cm^{-3} ($E_{00} = 58$ meV) for bicrystal B. However, the fits yield a low coefficient of determination, $r^2 < 0.995$, and fit poorly in the low temperature half of the plot of bicrystal A. The fits are even worse for bicrystal B, especially for the drift-diffusion/thermionic emission fit ($r^2 = 0.597$). When allowing for inhomogeneity among the grain boundaries in bicrystal A, the fits become much better for the one-step thermally assisted tunneling model ($r^2 = 0.997$), and the fitted values become $V_{b0} = 833$ meV, $N_b = 2.6\text{x}10^{17}$ cm^{-3} ($E_{00} = 9.8$ meV), and $\sigma = 82$ meV. However, the fit only gets worse for bicrystal B when including any inhomogeneity with the one-step thermally-assisted tunneling model. In addition to the

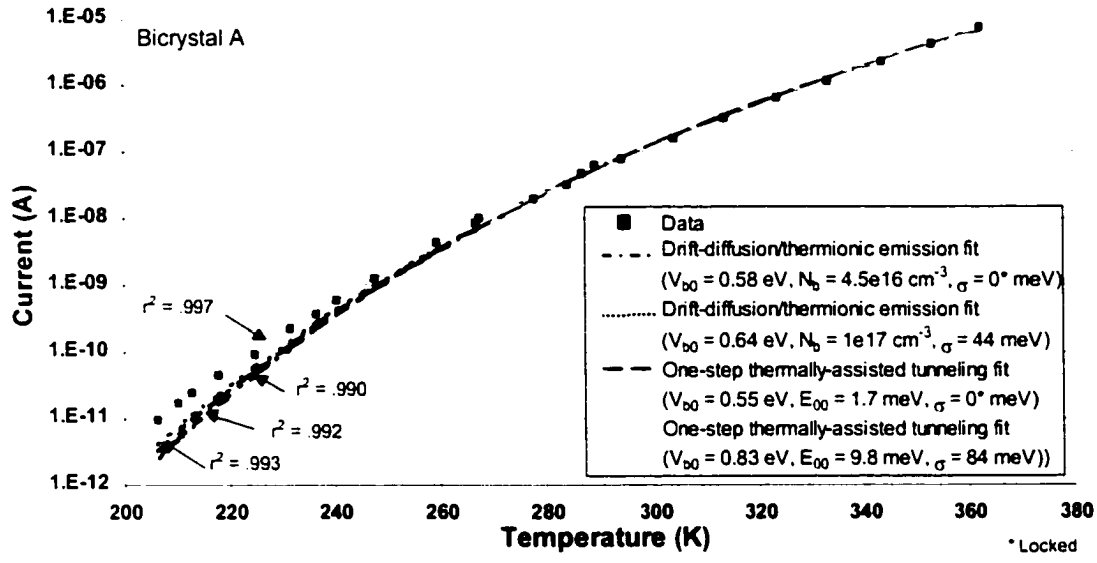

(a)

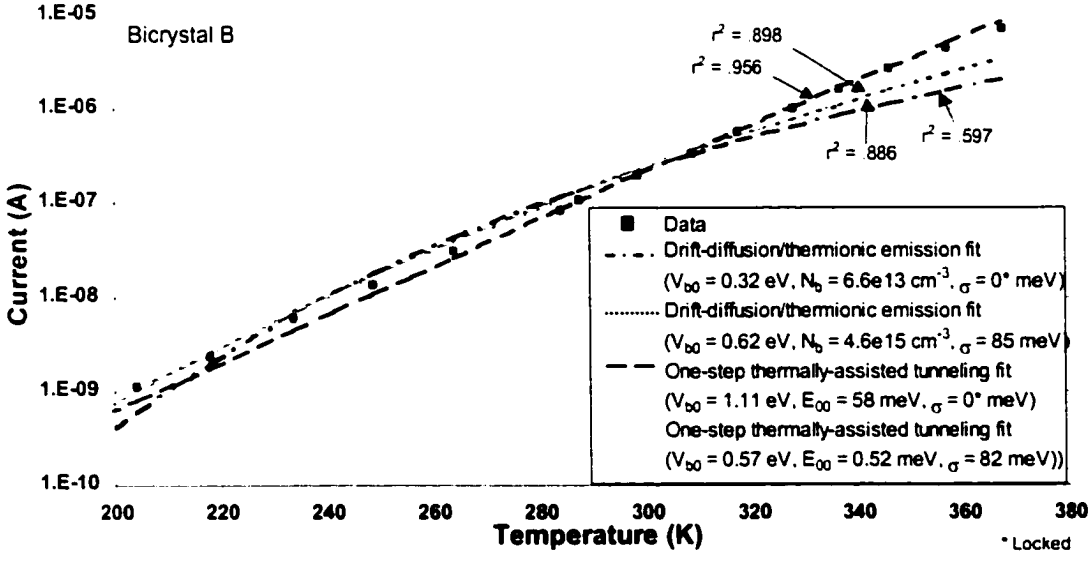

(b)

Figure 3.5 **Theoretical conduction model fits to GaAs bicrystal data for Bicrystal A (a) and Bicrystal B (b), using the Drift-Diffusion/Thermionic, and 1-step Thermally-Assisted Tunneling theories presented herein. Fits were accomplished with V_{b0}, E_{00} (N_b for Drift-Diff./Therm. Theory), and σ_s (barrier height inhomogeneity factor) as fitting parameters, which are given in the figure.**

poor fits for bicrystal B, the fitted values for V_{b0} and N_b for both bicrystals do not match the values as determined from Hall and capacitance techniques.

When using the values as determined from Hall and capacitance techniques for N_b and V_{b0}, the one-step thermally-assisted tunneling model fits as shown by the dashed lines in Figure 3.6. Much better fits can be obtained from the *two*-step thermally-assisted tunneling model, when using the same values of N_b and V_{b0} as determined from the Hall and capacitance techniques. The two-step fits are shown by the solid lines in Figure 3.6. These fits assumed exponentially increasing grain-boundary density of states parameters, as discussed earlier. The Hall and capacitance characterization, together with these fitting results, indicate that the current across the GaAs grain-boundaries most likely occurs via a two-step thermally-assisted tunneling process.

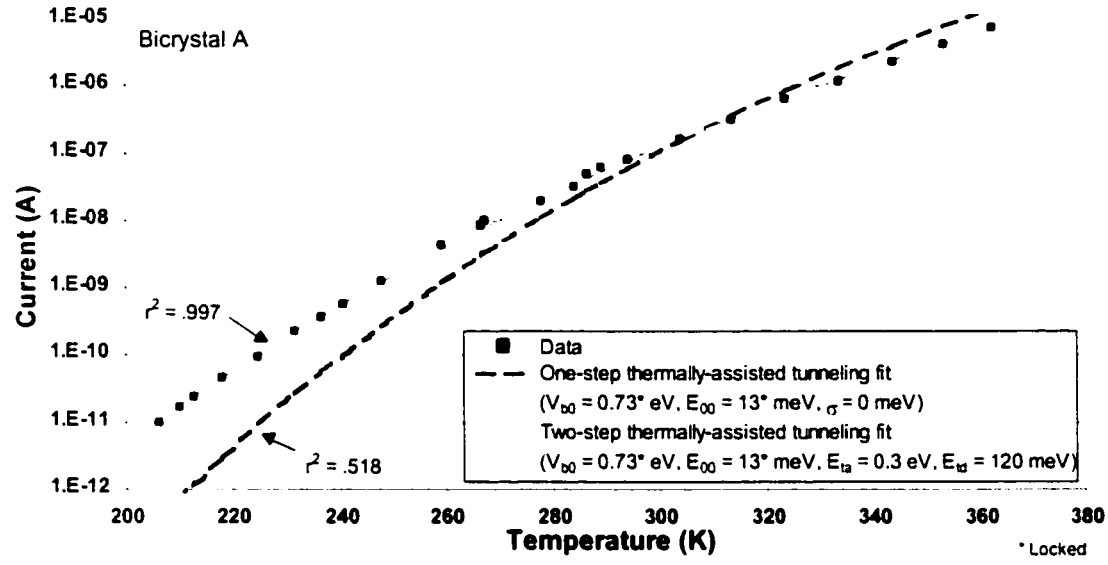

(a)

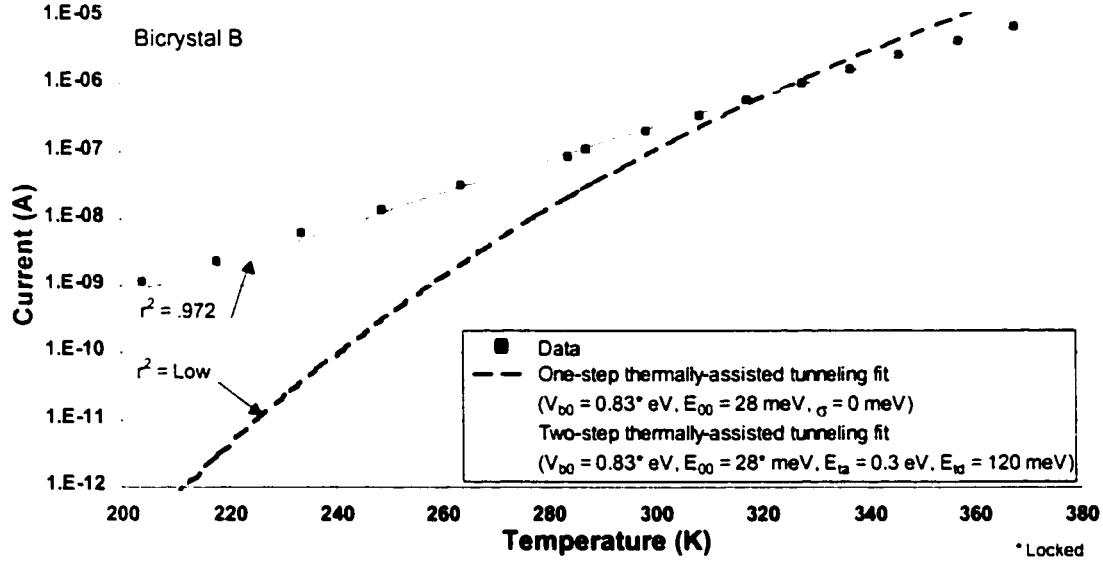

(b)

Figure 3.6 **Theoretical conduction model fits to bicrystal data for Bicrystal A (a) and Bicrystal B (b), using the 1-step, and 2-step Thermally-Assisted Tunneling theories presented in chapter 3. Fits were accomplished using V_{b0}, E_{00} (or N_b), values as determined by Hall and Capacitance measurements. This left σ_s (barrier height inhomogeneity) as the fitting parameter for the 1-step, and E_{ta} and E_{td} as the fitting parameters for the 2-step thermally-assisted tunneling models.**

Chapter 3 References

[54] R.K. Mueller, *J. Appl. Phys.*, **32**(4), pg 635-639, (1961).

[55] R.K. Mueller, *J. Phys. Chem. Solids*, 8, pg. 157, (1959).

[56] C. Ballif, M. Regula, and F. Levy, *Solar Energy Materials and Solar Cells*, 57, pp. 189-207, (1999).

[57] R.S. Muller and T.I. Kamins, "Device Electronics for Integrated Circuits", 2nd edition, John Wiley & Sons, Inc., New York, (1986).

[58] M. Shur, *IEEE Trans. On Electron. Dev.*, **35**(9), pg. 1565, (1988).

[59] C.R. Crowell and S.M. Sze, *Solid-St. Electron.*, **9**, pg. 1035, (1966).

[60] R.H. Bube, "Electrons in Solids - 2nd edition," Academic Press Inc., San Diego, pp167-174, (1988).

[61] J. Martinez and J. Piqueras, *Solid-St. Electron.*, 23, pp. 297-303, (1980).

[62] A. R. Riben and D. L. Feucht, *Solid State Comm.*, **9**, pp. 1055-1065, (1966).

[63] C. T. Sah, *Phys. Rev.*, 123(5), pp. 1594-1612, (1961).

[64] L. Esaki, "Solid-State Physics in Electronics and Telecommunications," Academic Press, Inc., New York, Vol. 1, (1960).

[65] W. A. Harrison, *Phys. Rev.*, 123 (1), pp. 85-89, (1961).

[66] C.R. Crowell and V.L. Rideout, *Solid-St. Electron.*, **12**, pp. 89-105, (1969).

[67] M. Al-Jassim, verbal communication, (1998).

[68] F. A. Padovani and R. Stratton, *Solid-St. Electron.*, **9**, pp. 695-707, (1966).

[69] S. J. Fonash, *Solid-St. Electron.*, **15**, pp. 783-787, (1972).

[70] D. Park, "Introduction to Quantum Theory, 2nd edition," McGraw –Hill, Inc., New York, pp. 104-108, (1974).

[71] J.W. Conley and G.D. Mahan, *Phys. Rev.*, **161**(3), pg. 161, (1967).

[72] G. Sarrabayrouse, J. Buxo, A. Myszkowski, and D. Esteve, *Revue De Physique Appliquee*, **12**, pp. 433-437, (1977).

[73] G. Lucowsky, *Solid State Comm.*, **3** , p. 299, (1965).

[74] I. Lundstrom, and C. Svensson, *J. Appl. Phys.*, **43**(12), pg. 5045-5047, (1972).

[75] J. Camassel, D. Auvergne, H. Mathieu, R. Triboulet and Y. Marfaing, *Solid State Comm.*, **13**, p. 63-68, (1973).

[76] R. Ludeke, *J. of Appl. Phys.*, **39**(8), pp. 4028-4029, (1968).

Chapter 4

EXPERIMENTAL PROCEDURES

This chapter presents relevant sample preparation and experimental apparatus description necessary to discuss the experimental results herein. The sample growth and processing will be described first in section 4.1 with attention given to the processes that will be evaluated by in-plane electrical characterization. This will be followed by a description of the lift-off technique and contacting which enables in-plane electrical characterization of CdTe from as-processed solar cells. Section 4.2 provides a detailed description of the in-plane electrical characterization technique and experimental apparatus. Finally, a description of the data analysis and curve fitting is given in section 4.3.

4.1 Polycrystalline Sample Preparation

All polycrystalline samples described herein were processed at the National Renewable Energy Laboratory (NREL) using NREL's standard process for CdS/CdTe heterojunction solar cells. This process has produced solar cell devices with efficiencies in excess of 15%.[77]

4.1.1 Sample Growth and Processing

All films are deposited onto a 1.5 inch square substrate of SnO_2-coated Corning 7059 borosilicate glass. The SnO_2-coated glass is purchased from Solarex Corp. and acts as a n-type transparent top contact. The role of the individual device layers was discussed in

Chapter 1. An additional thin layer of insulating SnO_2 is first deposited by chemical vapor deposition (CVD). Next, approximately 1000Å of n-type CdS is deposited on the insulating SnO_2 by a chemical-bath solution.[78] The chemical-bath solution is typically at a temperature of 100°C, and the deposition time is 35-40 minutes. After the CdS deposition, the CdS is annealed in hydrogen at 300°C and 30 Torr for 5 minutes. Following the anneal, CdTe is deposited onto the CdS by close-spaced sublimation (CSS).[78] The CSS configuration is shown in Figure 4.1.

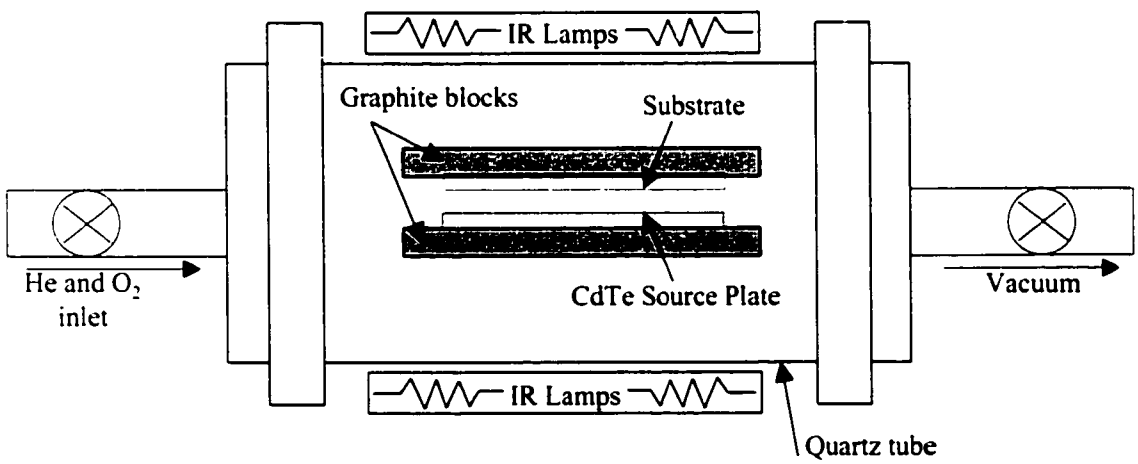

Figure 4.1 Schematic of Close-spaced sublimation chamber.

In the CSS configuration, a CdTe source plate and substrate are held facing each other at about a 2 mm spacing. Both He and O_2 are introduced into the chamber to obtain a background pressure of approximately 0.02 Torr. During the growth, the oxygen partial pressure is about 0.9 Torr, and the helium partial pressure is about 14.1 Torr. The infra-red (IR) lamps heat both substrate and source to growth temperatures of 620°C and 660°C, respectively. The growth takes place as elemental gases come off the higher

temperature CdTe source plate, diffuse over to the slightly cooler substrate, and recombine on the substrate surface. A typical film thickness is 8-10 μm.

After the CdTe deposition, the samples receive a $CdCl_2$ vapor treatment in a CSS configuration.[78] This configuration is very similar to that as shown in Figure 4.1, only a $CdCl_2$ source plate is used instead of a CdTe source plate, and the spacing is 1 mm. During the treatment, both the source and substrate temperature are held at 400°C for about five minutes. The growth chamber atmosphere is the laboratory ambient. After the CdTe deposition and vapor $CdCl_2$ heat treatment, the layers are as shown below in Figure 4.2. At this point, the samples are ready for back contact processing.

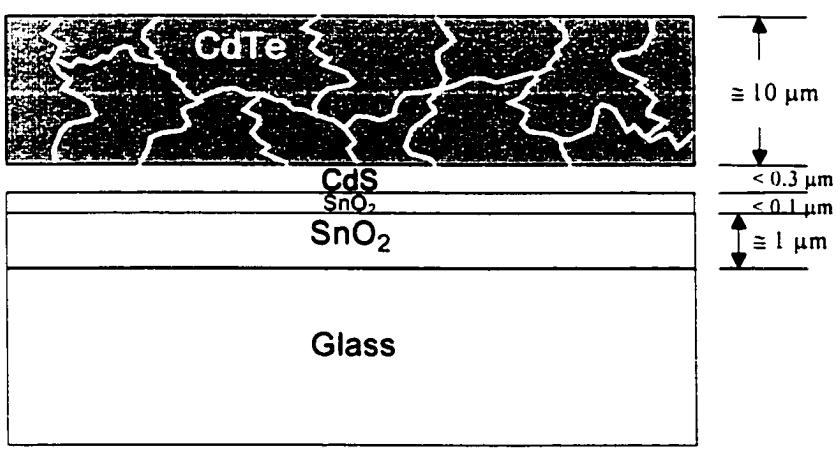

Figure 4.2 **Cross-sectional schematic of solar cell device prior to back contact processing.**

4.1.1.1 NP etch study

The samples for this study were processed up to the point of back contact metalization, which is the final layer to be processed. A 30-second dip into a NP etch (about 1% nitric acid, 70% phosphoric acid, and 29% water) is performed as part of the back contact

process. The NP etch creates a Te-rich surface, which becomes an interface layer between the CdTe and the back contact metalization. The Te-rich interface layer is postulated to aid in the formation of a low resistivity back contact, as NP etched solar cells have lower series resistance compared to unetched solar cells.[79] A side-effect of the etch is the creation of Te-rich grain boundaries as the etch has been shown to preferentially etch grain boundaries.[39,40] It is this side-effect that will be characterized by electrical measurements of the grain boundaries herein. Several samples were NP etched, while companion samples were left unetched for later comparison. The samples are ion-beam-milled about 0.3 μm to remove the Te-rich conducting layer on the surface. The unetched samples were also ion-beam-milled 0.3 μm for consistency. Ion-beam-milling was chosen for Te material removal, as chemical etching presented a greater chance of affecting the grain boundaries. Removal of the conducting surface layer by ion-beam-milling was visible to the eye, however previous x-ray photoemission spectroscopy (XPS) and Auger electron spectroscopy (AES) analysis show excess Te remaining in the grain boundaries to depths in excess of 1.2 μm.[39,40] In order to study the effects of the NP etch versus depth, ion-beam-milling is performed on etched and unetched samples to achieve milling depths of approximately 0.3, 1.8, 4.6, 6.1 and 7.8 μm. The ion-beam-milling depths were determined from companion samples with black wax dots as shadow masks to protect the underlying surface against the milling. After removal of the wax, the companion samples were subsequently profiled using a Dektak III profilometer to determine the thickness of CdTe removed. All of the samples prepared for the NP etch study are listed in Table 4.1 below.

Table 4.1 – Samples for NP etch study

	Ion-Beam-Mill Depth				
	0.3 μm	1.8 μm	4.6 μm	6.1 μm	7.8 μm
NP-etched	P360np	P360npx	P393np	P393npx	P392np
Unetched	P360	P360x	P393	P393x	P392

4.1.1.2 CdTe source plate usage study

A second group of samples were prepared to study the effects of the CdTe source plate usage during the CSS CdTe deposition. Typically, a new CdTe source plate is prepared for every 12-15 sequentially grown samples. Each group of samples corresponding to a single source plate constitutes a "run." Samples from different points in the run sequence, and from different runs, were taken for electrical characterization. Following the CdTe deposition these samples received the 400°C vapor $CdCl_2$ treatment and a light 0.3 μm ion-beam-mill to clean the back CdTe surface. The original CdTe thickness on these samples was 8.0 μm. The samples are listed in Table 4.2 below.

Table 4.2 – Samples for CdTe source plate usage study

CdTe Source Plate	Samples ID and position in run
CdTe 8-25c	P902, #2; P956, #3
CdTe 8-25b	P1019, #2; P922, #7; P991, #12

4.1.1.3 Vapor $CdCl_2$ study

Finally, a few samples were cut in half and one half was processed with the 400°C, vapor $CdCl_2$ treatment, and the other without to determine the effects of this treatment on

the grain boundaries. These samples are listed in Table 4.3 below. Again all of these samples received the 0.3 μm ion-beam-mill described earlier to remove surface contaminants.

Table 4.3 – Samples for study on the $CdCl_2$ treatment

	Samples ID and position in run
Untreated	P2254a, P2254b, P2257a, P2257b, P2258a, P2258b
$CdCl_2$ Treated	P2254c, P2254d, P2257c, P2257d, P2258c, P2258d

4.1.2 Description of Lift-off Technique

In order to measure the different processing effects on the CdTe grain boundaries the CdTe must be isolated from the more conductive underlying layers. This is necessary even with the high resistivity of CdTe, since a thin insulating film offers little electrical resistance in the direction perpendicular to the plane of the film, compared to the long distances traversed for the in-plane measurements described herein. The CdTe is removed or lifted-off from the rest of the device by using a technique similar to that of von Windheim et al.,[47] but developed independently at NREL for CdTe on CdS. A piece of 3/8" thick glass is glued to the ion-beam-milled CdTe surface using Torr Seal, a product of Varian Corp. After a 24 hour curing time, the CdS, SnO_2 and thinner 7059 glass are popped off from the thick glass, Torr Seal and CdTe film by exerting a mechanical force at the position as shown in Figure 4.3. This leaves the CdTe that was formerly adjacent to the CdS as an exposed surface. Smooth films of CdTe can be made as large as 1.5 inches in diameter using this lift-off technique. The exposed surface is nearly free of CdS, except for small (< 1 μm), isolated islands of CdS, as determined by

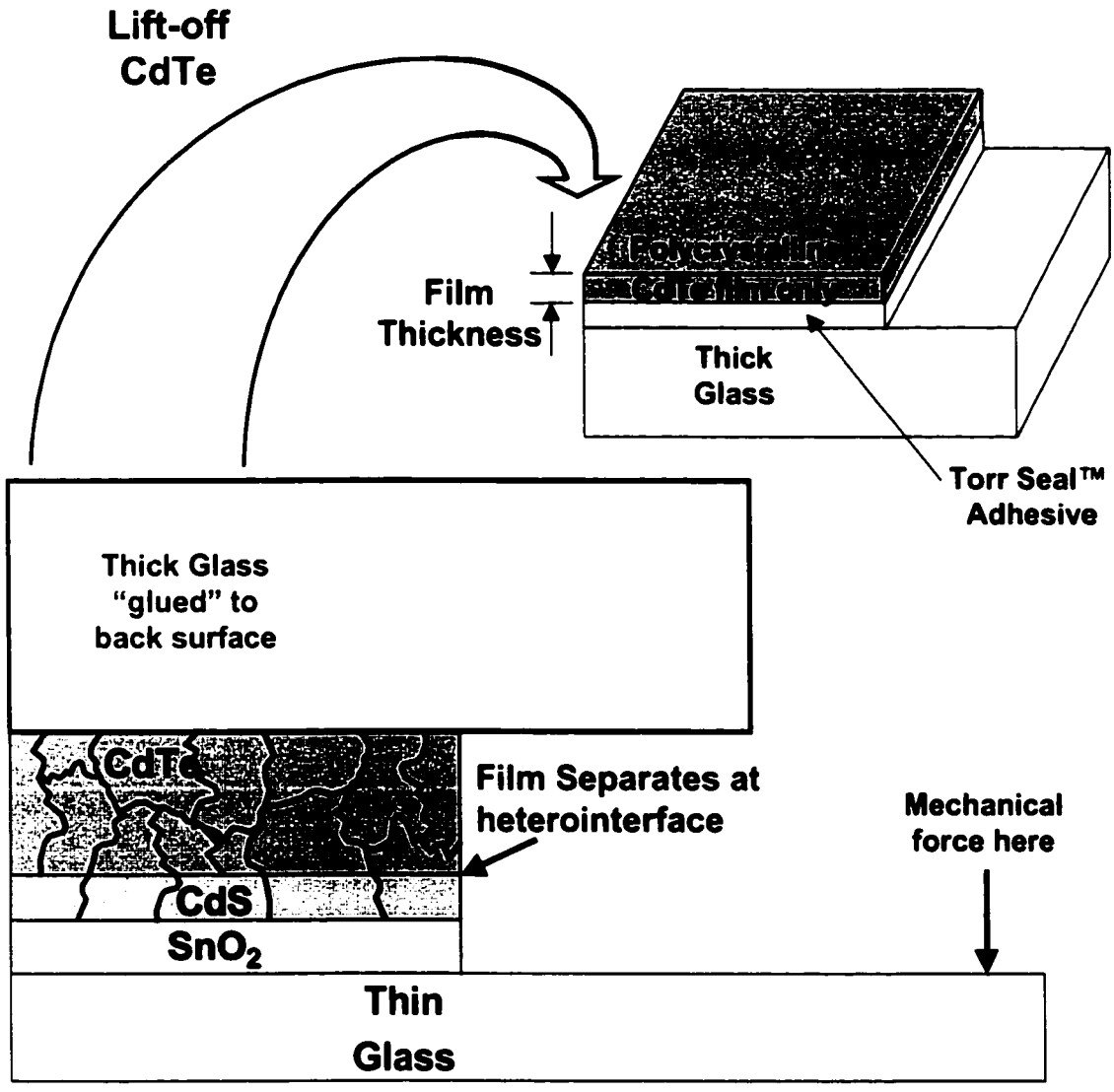

Figure 4.3 **Lift-off technique showing isolation of CdTe layer from the as processed solar cell.**

Auger Electron Spectroscopy. It is postulated that the separation occurs at the CdS/CdTe interface due to interfacial strain after the vapor $CdCl_2$ treatment. However for the vapor $CdCl_2$ study herein, some isolated films of CdTe were obtained without the vapor $CdCl_2$ treatment, but with a lower yield. Without the $CdCl_2$ treatment, some of the samples did

not separate at the heterointerface, but within the bulk of the CdTe layer. Following the lift-off, an optical microscope examination is performed on all samples to note direction and magnitude of any cracks that may exist in the isolated CdTe film. These cracks could potentially reduce the cross-sectional area of the measured film if the crack propagates in a direction that is parallel to the contacts. If multiple samples are to be made from a single growth sample, then the growth sample is cut up prior to the lift-off. This is due to the fragile nature of the lifted-off CdTe films.

4.1.3 Polycrystalline Contacting Scheme

Parallel stripes of gold contacts are evaporated on the lifted-off CdTe using metal shadow masks. The contacts are 2 mm wide by 11 mm long and can be spaced 0.4, 0.8, 1.2, 3.2, 3.6 and 5.6 mm apart. Four parallel contact stripes enables three separate two probe measurements and are small enough, when using the smaller contact spacings, to allow four separate samples to be prepared from a single 1.5 inch square growth sample. This contacting configuration is shown in Figure 4.4.

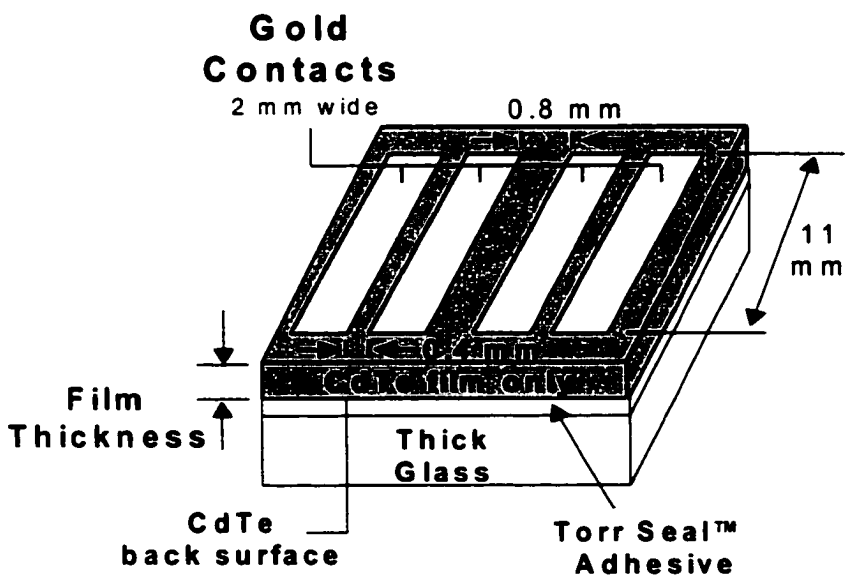

Figure 4.4 Lift-off CdTe typical sample size and contacting scheme.

Samples used for the contact resistance determination, have contact gaps of 0.4, 0.8, 1.2, 3.2, 3.6 and 5.6 mm. Due to the large contact gaps and number of contacts, the contact resistance samples require the entire 1.5 inch square growth sample.

4.2 Experimental Apparatus and Procedure

4.2.1 DC Current vs. Temperature Measurements

DC current versus temperature measurements are made at a fixed bias using a two-probe method. The DC bias is provided by a HP 6825A power supply and the current is measured by a Keithley 485 picoammeter. The sample sits on a resistively heated copper block, which provides the high temperature excursion, and is controlled by thermocouple feedback to a Lakeshore 330 temperature controller. Measurements in light used a single halogen bulb as a white light source with a reostat to control intensity. Light intensity at the sample was set to a 1-sun power density (100 mW/cm^2) by a calibrated silicon detector cell. Data acquisition is automated using a MacIntosh SE computer and National Instruments' LabView software. The set-up connections are shown in Figure 4.5 with the dark colored wiring. The DC current versus temperature measurements were performed at a fixed bias. The bias was chosen such that the voltage per grain boundary is small and much less than kT as needed for the theory presented in chapter 3. The number of grain boundaries per unit distance is determined from Scanning Electron Microscopy (SEM) images. The measured current across the polycrystalline material can exhibit a long settling time in response to a step change in voltage or illumination conditions. The settling time is dependent upon the barrier height, and is due to grain boundary defect state charging and discharging. The light generated minority carriers changes the

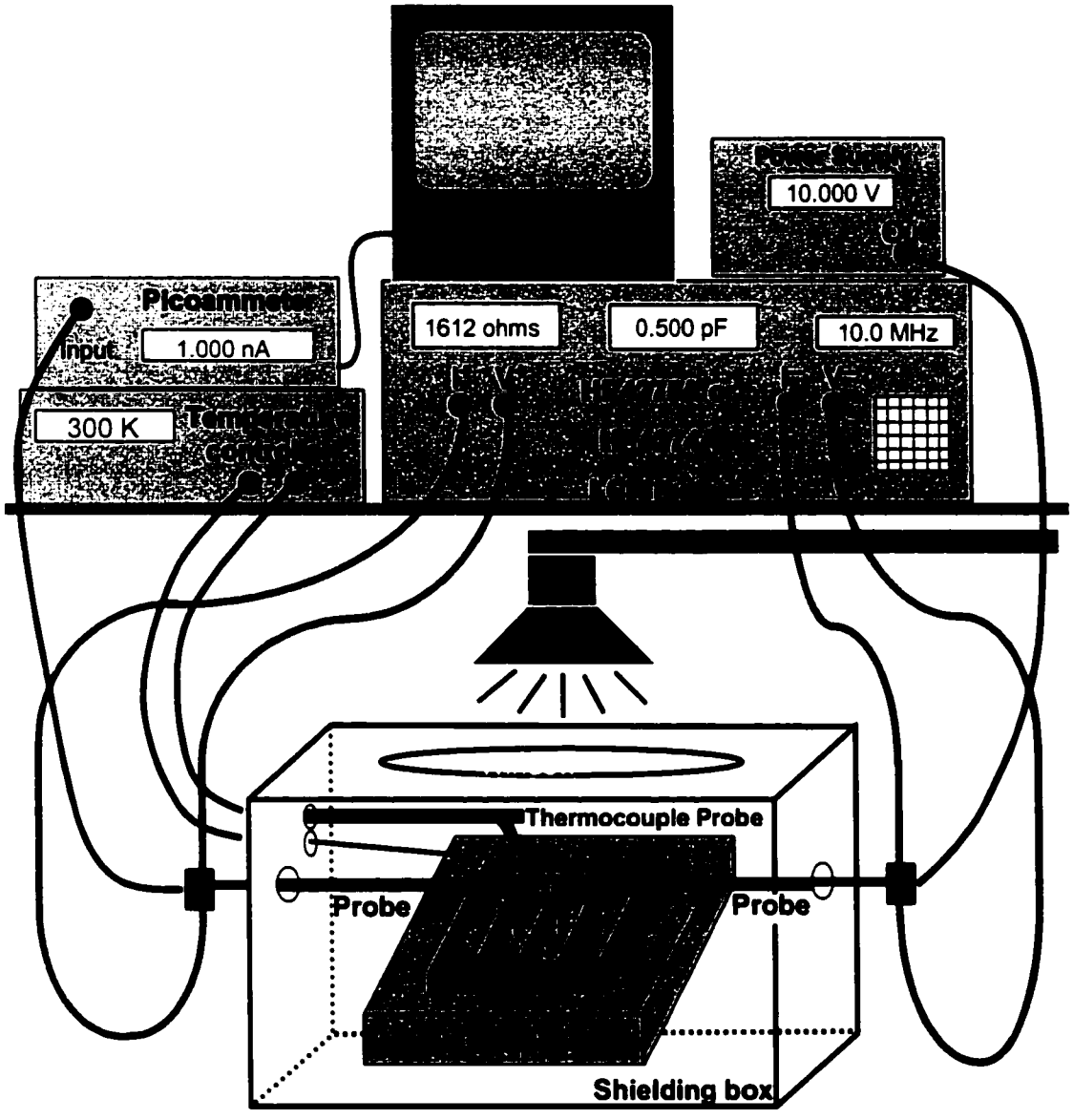

Figure 4.5 **Experimental set-up for impedance measurements using LCR meter and showing connections (grey colored wires). Set-up can be configured for current vs. temperature measurements (black wires) using the temperature controller, picoammeter, power supply, and computer for data acquisition.**

equilibrium minority carrier current into the grain boundary, which consequently modifies the occupancy of the grain boundary defect states as trapped majority carriers can recombine with the minority carriers. This change occurs very quickly with illumination as minority carriers are generated instantaneously in the vicinity of the grain boundary. But upon removal of the light, the change in the defect state occupancy relies on the dark minority current and the thermal emission of majority carriers to restore the dark equilibrium condition. Thus, for measurements in the dark, one hour was required for the current to stabilize. Measurements in light only required one minute of illumination for the current to stabilize. The sample temperature was varied from approximately 25°C to 140°C during the measurements. First the sample temperature is slowly ramped up until the sample reaches the high-temperature set-point of 140°C after about ten minutes, then the heat is turned off, and the sample is allowed to cool down in the air ambient to 50°C. Data is taken during the warm up and cool down at ten second intervals. The cool down time in the dark is approximately 35 minutes. The cool down time during light measurements is longer by about 15 minutes, which is due to supplemental heating from the halogen bulb.

4.2.2 Impedance Measurements

The Re(Z) measurements versus frequency measurements were made using HP 4274A and 4275A LCR meters, which together provided a 100-Hz to 10-MHz frequency range. Internal power supplies provided DC bias control. The experimental set-up is also shown in Figure 4.5 with light colored wire connections. The LCR meters are calibrated on a yearly basis. The resistance range is 10^{-1} - $2x10^{7}$ ohms, and three digit resolution is specified as a minimum throughout this ranges. When calibrated, the worst case

accuracy of the resistance measurement is 5%, and occurs when measuring large resistances. Parasitic resistance, capacitance, and inductance from the leads, probes, and box are determined as a function of frequency prior to the measurements. Subsequent measurements are adjusted automatically for the parasitics by the LCR meter.

Here again, darkness and bias are applied one hour prior to the measurement to allow the sample resistance to stabilize for dark measurements, whereas only one minute is required for light measurements. The measured resistance is allowed to stabilize for each change in voltage or frequency. The AC voltage was 1 V.

DC measurements of the resistance are obtained using a Kiethley 6517A Electrometer because the sample DC resistance is typically much higher than the impedance analyzer's 2 MΩ maximum. The 6517A has an internal power supply for bias control and can measure currents as small as $2x10^{-12}$ amperes. This enables resistance measurements as high as 500 Giga-ohms from a 1V bias.

4.2.3 Other Measurement Equipment

Other measurement equipment referred to herein are described as follows:

XPS measurements were made using a Physical Electronics 5600 with a monochromatic Al X-ray source. The XPS technique involves the bombardment of a sample surface with X-rays and the measurement of the concomitant photoemitted electrons. The photoemitted electrons have discrete kinetic energies that are characteristic of the emitting atoms and their bonding states. XPS can go beyond elemental analysis to provide chemical information. For the measurements in this thesis, the X-ray beam power was approximately 300 W, the spot size was 0.8 mm, and elemental resolution is 1 at. %.

AES measurements were performed for elemental surface analysis using a Physical Electronics 670I field emission scanning Auger nanoprobe. With AES, a sample surface is bombarded with a focused beam of electrons. This generates Auger electrons, which are collected and measured. Auger electrons have discrete kinetic energies that are characteristic of the emitting atoms, making AES useful for identifying elemental composition. The ability to focus and deflect the electron beam makes enables surface composition maps. For the composition maps shown herein, the electron beam size was 100 nm and the elemental surface sensitivity is 1 at. %.

SEM and electron beam induced current (EBIC) measurements were made using a JEOL JSM 840. Beam energy and magnification are noted where images are displayed.

Chapter 4 References

[77] Y. Mahathongdy, D.S. Albin, C.A. Wolden, and R. M. Baldwin, AIP Conf. Proc., 15th NREL Photovoltaics Program Review, edited by M. Al-Jassim, AIP Press, pp. 236-241, (1999).

[78] D. H. Rose, F. S. Hasoon, R. G. Dhere, D. S. Albin, R. M Ribelin, X. S. Li, Y. Mahathongdy, T. A. Gessert, and P. Sheldon, Prog. in Photovolt.: Res and Appl., 7, pp. 331-340, (1999).

[79] X. Li, D.W. Niles, F.S. Hasson, R.J. Matson, and P. Sheldon, unpublished (1997)

CHAPTER 5

RESULTS and DISCUSSION

5.1 Physical Characterization of Lift-off CdTe Film

The lift-off CdTe films were evaluated in terms of grain size, macroscopic defects, and surface composition. This was accomplished using SEM images, optical microscopy, and Auger surface mapping, respectively. The physical characterization of lift-off films is needed because the technique represents a new method for isolating the CdTe films for later analysis.

5.1.1 SEM Results

SEM images were taken of samples used in the $CdCl_2$ treatment study and are shown in Fig. 5.1(a-d). Images (a) and (c) show the film processed up through the $CdCl_2$ treatment, while images (b) and (d) are of the untreated film. The lifted-off surface is shown in Figure 5.1(a) and (b), and the back surface prior to lift-off is shown in (c) and (d). The lift-off surfaces were NP-etched to help delineate the individual grains as the NP-etch preferentially etches grain-boundaries.[40] After the etch, the grains were more discernible in the $CdCl_2$ treated sample, but it is difficult to determine individual grains in the untreated sample as the morphology appears more motley, pitted and over-etched. Nonetheless, from a qualitative visual inspection, it is evident that the approximate grain size on the lift-off side is about the same between $CdCl_2$ treated and untreated. In

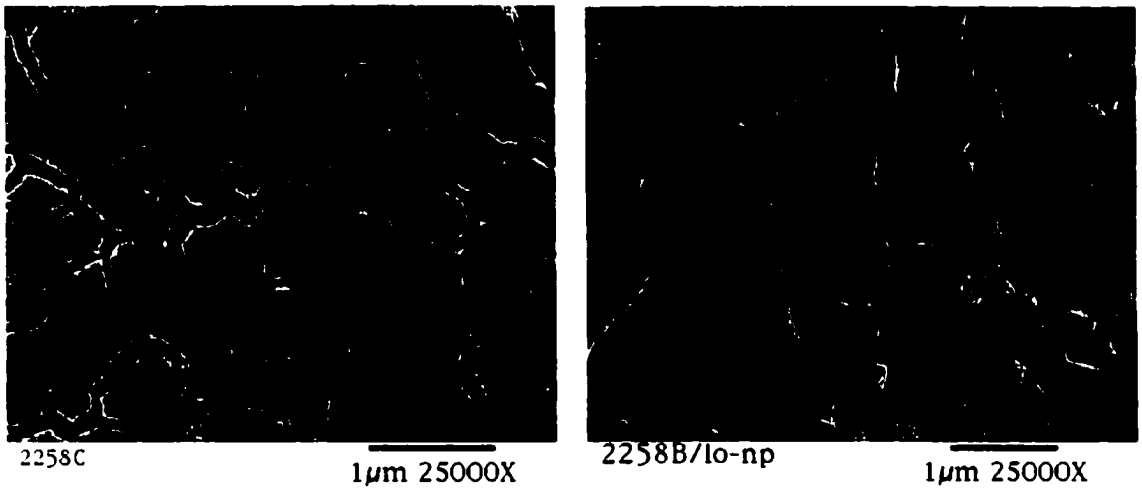

(a) Lift-off side, $CdCl_2$ treated (b) Lift-off side, untreated.

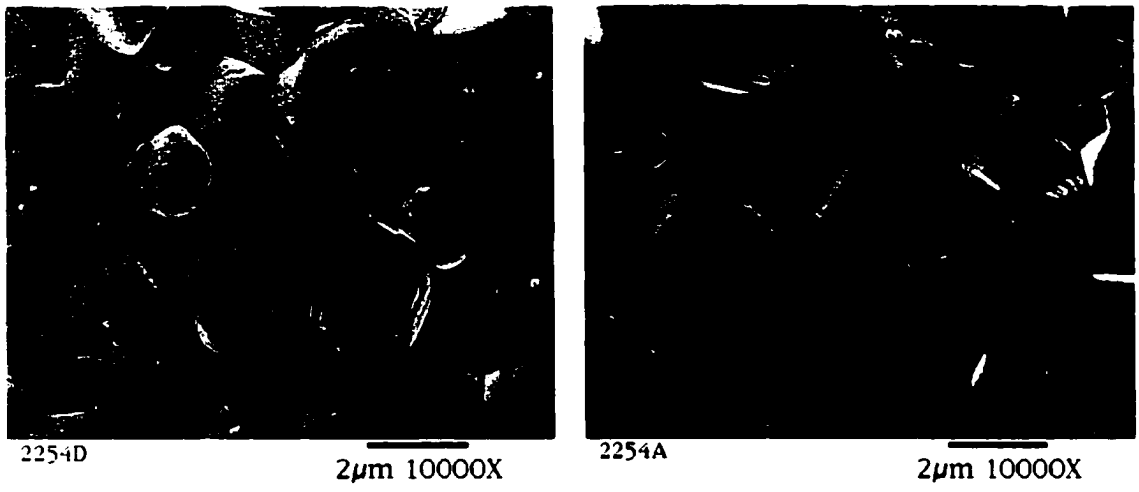

(c) Back-side, $CdCl_2$ treated. (d) Back-side, untreated.

Figure 5.1 **SEM surface images of lift-off CdTe shown in upper images, (a) and (b), and CdTe back-side prior to lift-off shown in (c) and (d). $CdCl_2$ treated samples are on the left, (a) and (c), while untreated samples are on the right, (b) and (d). Lift-off CdTe images shown in (a) and (b) were NP-etched to delineate grain boundaries. The images shown are from sample P2254 and P2258, and were taken by Rick Matson at the National Renewable Energy Laboratory. Scale is as indicated in the images.**

addition, the lift-off grain size is about half that of the more clearly distinguishable back surface grain size.

A measure of the number of grain boundaries per unit distance was obtained from the back surface images by counting the number of grain boundaries intersected by a

horizontal line drawn across each of the images. This was done in ten different places and an average number of grain boundaries per micron was calculated. For the $CdCl_2$ treated sample, the average number of grain boundaries per micron was found to be 0.66 with a standard deviation of 0.07. Similarly for the untreated sample, the average number of grain boundaries per micron was 0.69 with a standard deviation of 0.07. Thus, there is no significant difference in the grain size between $CdCl_2$ treated and untreated CdTe films. Therefore, the grain size is unaffected by the $CdCl_2$ treatment. This correlates with previous studies on the effect of the $CdCl_2$ treatment on the grain size.[14,80] It should be noted that these results, as well as cross-sectional images (not shown) indicate that the grain size increases toward the back of the film. The non-uniform grain size can lead to preferential conduction through the area of lower resistance or fewer grain boundaries (large grain sizes). The effect of cross-sectional area and voltage per grain boundary is explored in Appendix D. However, based on these images, the nominal voltage per grain boundary was taken to be the same for equal distance contacts from all samples measured.

5.1.2 Auger Surface Analysis

Scanning Auger compositional analysis was performed on the lift-off CdTe surface on samples both with and without a $CdCl_2$ treatment. The purpose of the Auger was to determine if any residual CdS remained on the lift-off surface. None of the samples demonstrated a continuous CdS layer or web, but tiny discontinuous islands of sulfur enriched areas were evident. These show up as bright white areas in the SEM image of the $CdCl_2$ treated sample as shown in Figure 5.2(a).

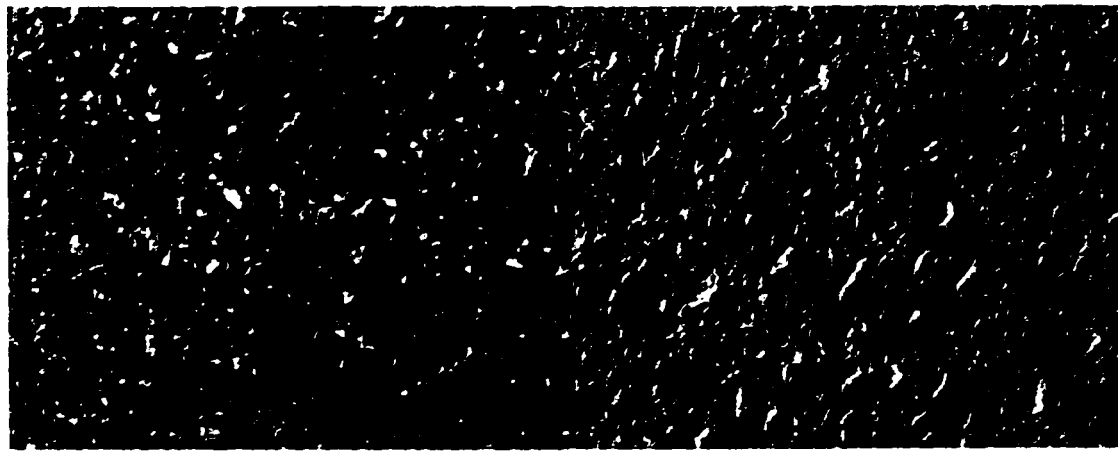

(a) $CdCl_2$ treated (b) untreated

Figure 5.2 SEM of lift-off CdTe surface for $CdCl_2$ treated (a) and untreated (b). Bright areas in (a) correspond to areas with a higher Sulfur content. Contrast is not comparable between (a) and (b). Mag. = 3000x, or 3 mm = 1 μm.

A more detailed analysis of individual points on the bright white spots gives a sulfur signal in the 10-20 atomic % range and a tellurium signal in the 10-20 atomic % range. Off of the bright white spots, the sulfur signal is in the 2-10 atomic % range while the tellurium signal is in the 20-30% atomic % range. The remaining constituents were carbon (25 - 50 at. %) and oxygen (3 – 10 at. %) which are common as adsorbed species on unprotected CdTe surfaces.[81] Carbon and oxygen aside, these measurements indicate either a mixed CdS_xTe_{1-x} alloyed surface or sub-micron islands of CdS remaining on the surface. The untreated samples shown in Figure 5.2(b) did not display bright areas, or have areas with high sulfur content. The background sulfur signal for this sample was in the 2-6 atomic % range.

5.2 Lift-off CdTe Film Resistivity

Measurements of the dark in-plane resistivity were performed on most of the lift-off CdTe samples. Table 5.1 shows the average resistivity values and standard deviation at

50 °C and 125 °C for 8 samples with the standard treatment ($CdCl_2$ treated) before back contact formation and 3 samples without $CdCl_2$ treatment. Each sample had several different contact spacings, thus the results are based over 30 different measurements. As can be seen from the average values for the standard treatment, the film dark resistivity is reduced by about two and a half orders of magnitude from 50 °C to 125 °C. The nature of the decrease in the film resistivity with increased temperature is discussed in section 5.5. Also, the calculated average and standard deviation values show a significant difference (about one standard deviation) in the resistivity between samples with the standard treatment and samples without the $CdCl_2$ treatment at 50 °C. The difference at 125 °C is not as significant. Thus, the $CdCl_2$ treatment increased the film resistivity. The effect of the $CdCl_2$ treatment on the in-plane electrical properties is the subject of section 5.5.2.

Table 5.1 Lift-off polycrystalline CdTe Resistivity at 50 °C and 125 °C, and an applied bias of 1 V.

Sample(s) ID	Sample Treatment	Statistics	Resistivity At 50 C (ohm-cm)	Resistivity At 125 C (ohm-cm)
P902, P956, P972, P991, P1019	Standard	Average	1.3E+08	5.7E+05
P2254 C&D, P2257 C&D, P2258 C&D		Std. Dev.	8.3E+07	4.0E+05
P2254 A&B, P2257 A&B, P2258 A&B	w/o $CdCl_2$	Average	4.0E+07	2.5E+05
		Std. Dev.	1.5E+07	1.1E+05

A large standard deviation was calculated from the resistivity values of the samples with the standard treatment. This variation was initially thought to be a result of some cracks as seen in most of the lift-off films. However, there was no correlation between the length of cracks and the film resistance. Thus, the question of the origin(s) of the sample-to-sample variations remains. Although not shown herein, the sample thickness

variation is well characterized for the CSS growth of CdTe, and has been shown to be less than 15% over the area where the lift-off is performed.[82] Thus, the film thickness variation is insufficient to explain the resistivity variations seen here. One possibility for the sample-to-sample variation could be any uncontrolled variations in growth and processing such as the source plate usage which is discussed later in section 5.5.3.

In addition to the samples listed above, the resistivity of several earlier samples was measured at 10 volts and under 100 mW/cm^2 of white light illumination. These samples are shown in Table 5.2. The 10 volt bias was used before careful optimization of the test set-up and standardization to the 1 volt bias. As can be seen from the table, the resistance under illumination decreases by several orders of magnitude, indicating strong photoconductivity in the unetched CdTe. In polycrystalline materials, photoconductivity can be due to an increase in the bulk free carrier concentration and/or a lowering of the grain-boundary energy barrier. The exact cause of the photoconductivity will be addressed later in section 5.4 of this chapter. Another trend to note is that the samples that have been NP-etched have a dark resistance almost four orders of magnitude lower than the standard unetched samples. In addition, the NP-etched samples are not as photoconductive as the unetched samples, since their resistance under illumination is only two-thirds of their dark value.

Table 5.2 **Lift-off Polycrystalline CdTe Resistivity at room temperature and with an applied bias of 10 V. Table shows resistivity differences between dark and illuminated with 100 mW/cm^2 white light, and NP-etched versus unetched.**

Sample(s) ID	Sample Treatment	Statistics	Dark Resistivity (ohm-cm)	Light Resistivity (ohm-cm)
P360 #1, P360 #2, P360 #12	Standard	Average	6.9E+08	2.2E+05
		Std. Dev.	5.1E+08	2.3E+05
P360np #1, P360np #2, P360np #12	NP-etched	Average	4.9E+04	1.7E+04
		Std. Dev.	2.6E+03	3.3E+03

5.3 Contact Resistance

The significance of the evaporated gold contact resistance was determined from some of the samples herein. DC electrical characterization of the lift-off film in-plane properties is not valid unless the contact resistance is negligible compared to the film resistance. The contact resistance can be determined using the Transfer Length Method (TLM) as described in Chapter 2. The TLM for sample P991 is shown in Figure 5.3, where (a) is the result at 50 °C and (b) is the result at 125 °C. For each plot, a line best fitting the data is shown to intersect the resistance axis near the zero ohms point. The nonsensical negative y-intercept shown in Figure 5.3 (a) is a result of the y-intercept being smaller than the standard deviation of the measured resistance. The sizable standard deviation is due to significant scatter in the data from the individual measurements on a sample. An example of the scatter can be seen from the different values of resistance that was measured from the three 1.2 mm contact spacings on sample P991. Error bars corresponding to $\pm$ one standard deviation for the three 1.2 mm spacings are indicated in both plots. Despite the scatter, the trend of the best-fit line indicates a negligible contact resistance when compared to the measured resistance values.

Figure 5.3(b) shows the TLM at high temperatures, since it is important for the contact resistance to be negligible at high temperatures as well. For this case, the indicated contact resistance is over an order of magnitude less than that of the average resistance measured.

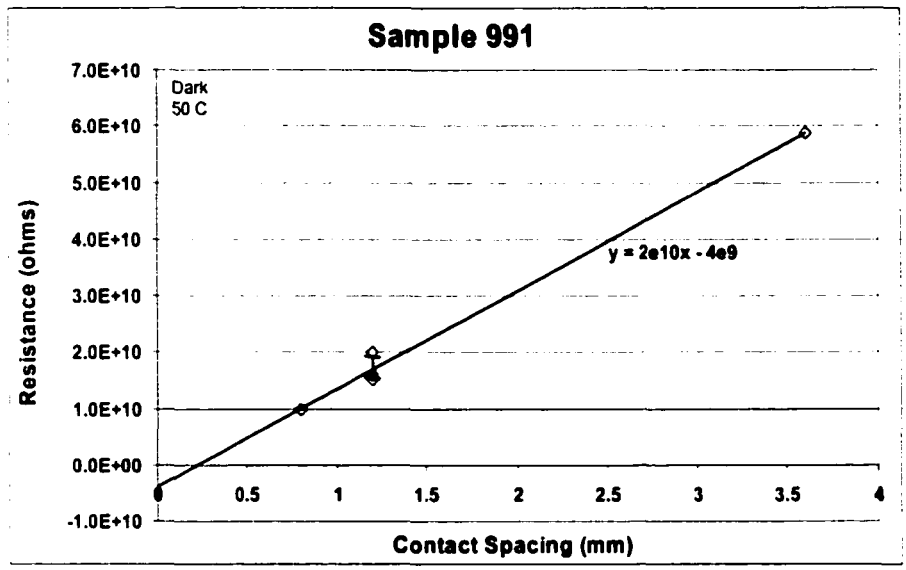

(a)

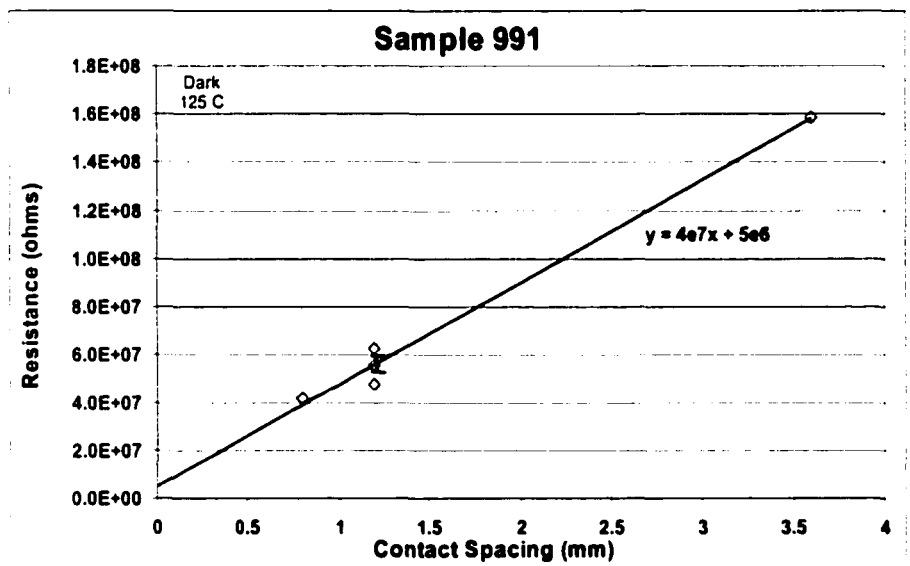

(b)

Figure 5.3 TLM performed on sample P991 at 50 °C (a) and 125 °C (b).

The TLM contact resistance results of several samples are summarized in Table 5.3. The samples tabulated represent all of the processing conditions used for in-plane measurements. The table also shows the average resistance measured for comparison with the contact resistance, R_c. In all cases, the contact resistance as derived from the TLM is either negligible, or about an order of magnitude less than the average resistance measured for all samples from all process conditions.

Table 5.3 Contact Resistance, R_c, at high and low temperatures as measured using the TLM.

Sample ID	Processing Condition	Illumination Level	Temp. (Celsius)	Number of data points	Average Resistance measured (ohms)	Rc (ohms)
P360*	Standard	Dark	25	3	4.0E+10	negligible
P360NP*	NP-etched	Dark	25	3	2.5E+06	1.5E+05
P902	Standard	Dark	50	3	2.0E+10	1.9E+09
P902	Standard	Dark	125	3	1.3E+08	1.7E+07
P956	Standard	Dark	50	3	3.1E+10	negligible
P956	Standard	Dark	125	3	1.2E+08	negligible
P972	Standard	Dark	50	6	2.7E+10	negligible
P972	Standard	Dark	125	6	9.2E+07	9.3E+06
P991	Standard	Dark	50	5	2.4E+10	negligible
P991	Standard	Dark	125	5	7.3E+07	5.1E+06
P1019	Standard	Dark	50	6	2.2E+10	negligible
P1019	Standard	Dark	125	6	8.3E+07	negligible
P902*	Standard	Light	25	3	4.8E+06	negligible
P2257	Standard	Light	25	3	2.6E+06	5.4E+05
P2254	Standard	Light	25	3	1.5E+06	3.1E+05
P2257	w/o CdCl2	Light	25	3	3.2E+06	negligible
P2254	w/o CdCl2	Light	25	4	7.3E+05	1.7E+05

* Measured at 10 V, all others measured at 1 V.

Also shown in Table 5.3 is the apparent contact resistance under illumination. The film resistance in the light is several orders of magnitude less than the film resistance in the dark for the unetched samples. However, since the 2000 Å of gold is highly reflective to the white light, the contact is shaded during the resistance measurement under illumination. Thus, the measurement of film resistance under illumination is considered

to be a worst case scenario for contact resistance, since the film resistance is decreased by several orders of magnitude due to photoconductivity, yet the contact resistance should be relatively unchanged (except for at the contact edges). The results show that even in this worst case scenario, the contact resistance is much smaller or negligible compared to the film resistance.

The results indicate that the TLM values for the dark contact resistance are either negligible or about an order of magnitude less than the average film resistance. Therefore, we will proceed with the assumption of a negligible contact resistance for all samples and from all process conditions.

5.4 Frequency-Dependent Resistance Measurements

The *Re(Z)* was measured as a function of frequency for the lift-off CdTe films in the dark. The data is shown in Figure 5.4 for unetched films (a) and NP-etched films (b). The low frequency *Re(Z)* for the unetched sample was not measurable by the LCR meter, which can only measure up to 20 MΩ. Consequently the low frequency breakpoint was not observed as the low frequency resistance was higher than this maximum. However it can still be seen that the high-frequency dark resistance drops a minimum of four orders of magnitude from the maximum measurable value for the unetched film. As discussed in Chapter 2, the high-frequency resistance is comparable to nR_g, or the number of grains multiplied by the bulk resistance, since at high frequencies the grain boundary resistance, R_b, is shunted by the grain boundary capacitance, C_b. Also, the low-frequency resistance is equal to $nR_g+(n-1)R_b$. Thus, the grain boundary resistance is a minimum of four orders of magnitude higher than the bulk resistance for the unetched film. Following the same

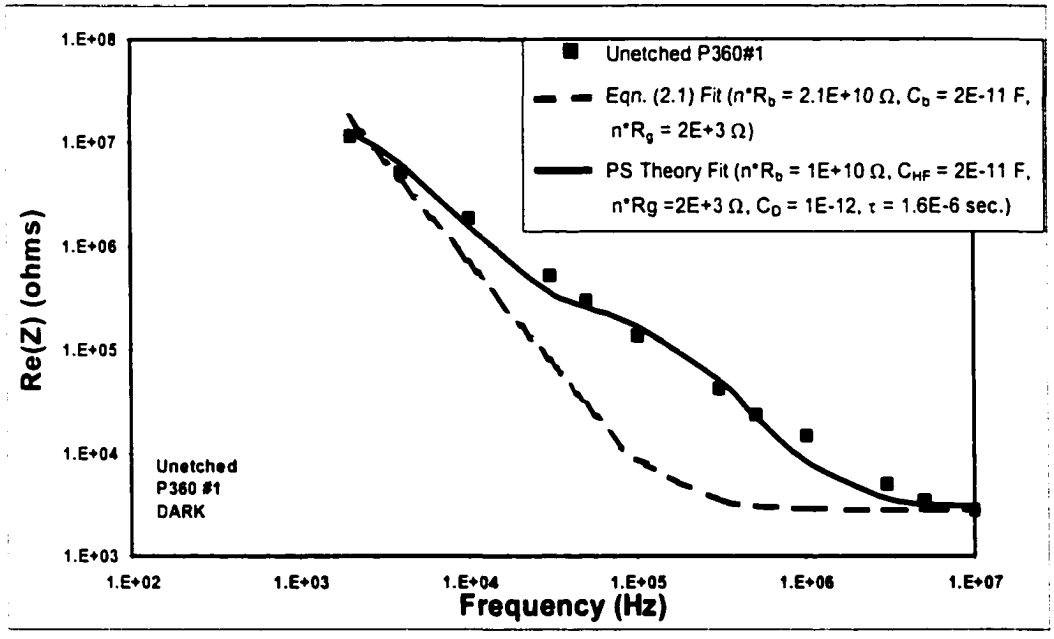

(a)

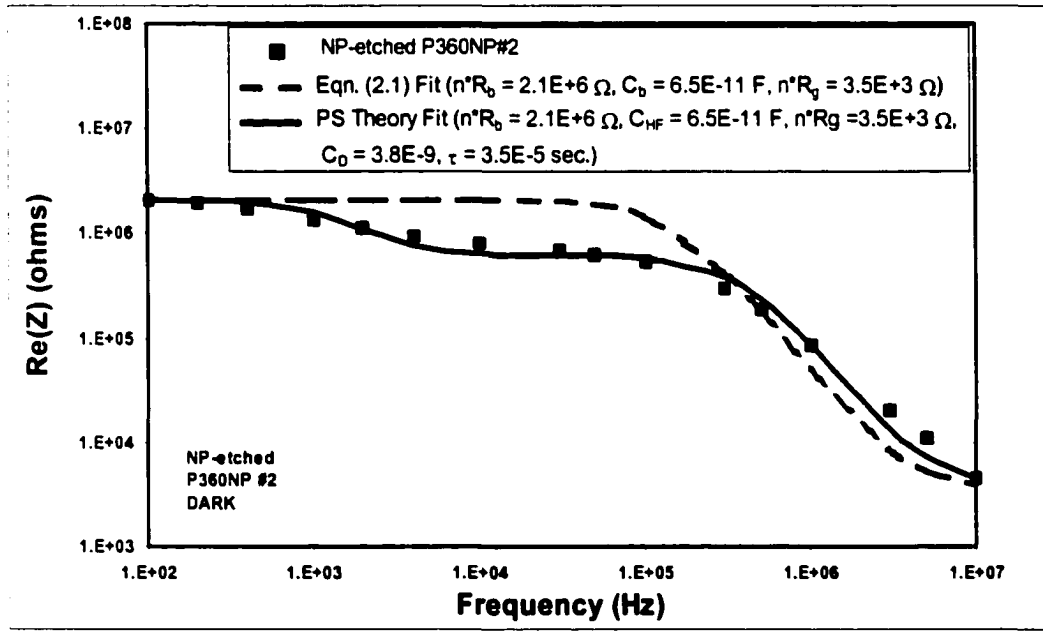

(b)

Figure 5.4 ***Re(Z)*** **vs. frequency for unetched (a) and NP-etched (b) films in the dark. Also, shown is the fit from the simple electrical model for polycrystalline films as given by Eqn. (2.1), and the fit to a modified electrical model (PS fit), which includes a frequency dependent feedback to the barrier conduction caused by charge injected into grain-boundary traps with a single time constant.**

analysis, the NP-etched film has a grain boundary resistance that is almost three orders of magnitude higher than the bulk resistance. The frequency dependent curve shapes also demonstrate that a low resistance shunt path around the grain boundaries and bulk can be safely ignored, as discussed in chapter 2.

The measured data were fit to the simple polycrystalline film electrical model, as given by equation (2.1), and the resultant fits are indicated by the dashed curves in Figure 5.4. The values for nR_g, nR_b, and C_b are indicated in the figures and are found from the fit to equation (2.1). The fit to the unetched sample is obviously somewhat arbitrary due to the lack of low-frequency data, however a DC data point was measured separately (Re(Z) = 10^{10} Ω, not shown) and added to the data at a frequency of 1 Hz to reduce the randomness of the fit. As can be seen from Figure 5.4, the simple model does not accurately fit the frequency dependence of Re(Z) for either sample. More specifically, the behavior of the curve between the low- and high-frequency breakpoints is measured to be approximately $\omega^{-1.1}$ for the unetched sample, and thus not as steep as ω^{-2}, predicted by simple polycrystalline model (dashed line) in Figure 5.4. In addition, the data from the NP-etched sample appears to have a couple of additional breakpoints not predicted by the simple model. In this case, the additional breakpoints would suggest the presence of a grain-boundary feedback mechanism, as discussed in chapter 2. Thus the *Re(Z)* data was fitted using the modified theory with grain-boundary feedback given by equation (2.2), and shown as the solid line in Fig. 5.4. This fit is labeled as the P&S fit (for Pike and Seager) and the fitted parameters are given in the figure. The relatively good fit of the NP-etched sample shown in Figure 5.4(b) would indicate that there is more-or-less a single dominant τ associated with these grain boundaries. In the case of the unetched

sample, the P&S model also yields a better fit than the simple model despite the obvious lack of additional breakpoints in the data. Thus, it is postulated that a smoother and more satisfactory fit to this sample could be obtained by assuming a smoothly varying distribution of time constants, which would be consistent with a density of grain boundary trap states that varies with energy as discussed previously. While it is beyond the scope of this dissertation to model this case and derive an exact fit to the data in Figure 5.4(a), a smoothly varying distribution of time constants is a potential explanation for the measured data.

Qualitative differences between data and theory aside, quantitatively it is apparent that the NP-etch lowers the low frequency, or grain boundary resistance, R_b, by at least an order of magnitude. However, the NP-etch does not appear to change the high-frequency bulk resistance, R_g, indicating that the NP-etch only affects the areas adjacent to the grain boundary. Using a bulk hole mobility μ_p, an estimate of the net bulk acceptor concentration, N_a, can be calculated from the high-frequency resistance, nR_g, according to:

$$N_a \cong \frac{1}{q\mu_p}\frac{d/A}{nR_g} \qquad cm^{-3} \tag{5.1}$$

where d is the contact spacing and A is the film cross-sectional area. It is assumed that the acceptor atoms are fully ionized, and that grain boundary depletion width is small compared to the grain size in this approximate calculation. Using a nominal CdTe bulk hole mobility $\mu_p \approx 60$ cm^2/V-s, and $nR_g = 2000$ ohms as taken from Figure 5.7 for the unetched sample, then $N_a \approx 9 \times 10^{14}$ cm^{-3}. This value of N_a is in the range of values of

bulk doping (N_a = 1-15 x 10^{14} cm^{-3}) as measured by capacitance-voltage techniques on similarly processed CdS/CdTe devices.[83]

The *Re(Z)* versus frequency measurement was also performed under illumination and the results are shown in Figure 5.5 for unetched (a) and NP samples (b). As can be seen from the plot of the unetched sample, the illumination lowers the low-frequency or grain boundary resistance to a point where it is now measurable by the LCR and thus possible to observe the low-frequency breakpoint. However, the high-frequency flattening is no longer fully observable due to the 20 MHz frequency limitation of the LCR meter.

The values for nR_g, nR_b, and C_b are indicated in the figures and are found from the fit to the simple model given by equation (2.1). Comparing the results to the dark curves of Figure 5.4, it is noted the illumination decreases the unetched grain boundary resistance, R_b, by a minimum of three orders of magnitude, but does not change the high-frequency grain bulk resistance, R_g, from its dark value. As stated earlier, the illuminated value of nR_g was not measurable due to the 20 MHz frequency limitation of the LCR meter. However, the fit from equation (2.1) indicates that this value has not changed much from its dark value. Thus, the photoconductivity in the CdTe film can be attributed to the grain boundaries. The grain boundary energy barrier can be lowered under illumination due to a large increase in the minority carrier current to the grain boundary. This changes the equilibrium occupancy of grain boundary states by reducing the majority carrier concentration at the grain boundary and subsequently reducing the barrier height.[84] This also reduces the grain-boundary time constant, $R_{LF}C_D$, as discussed in chapter 2. The smaller time constant pushes the ω_{LF} and ω_{HF} breakpoints out several orders of

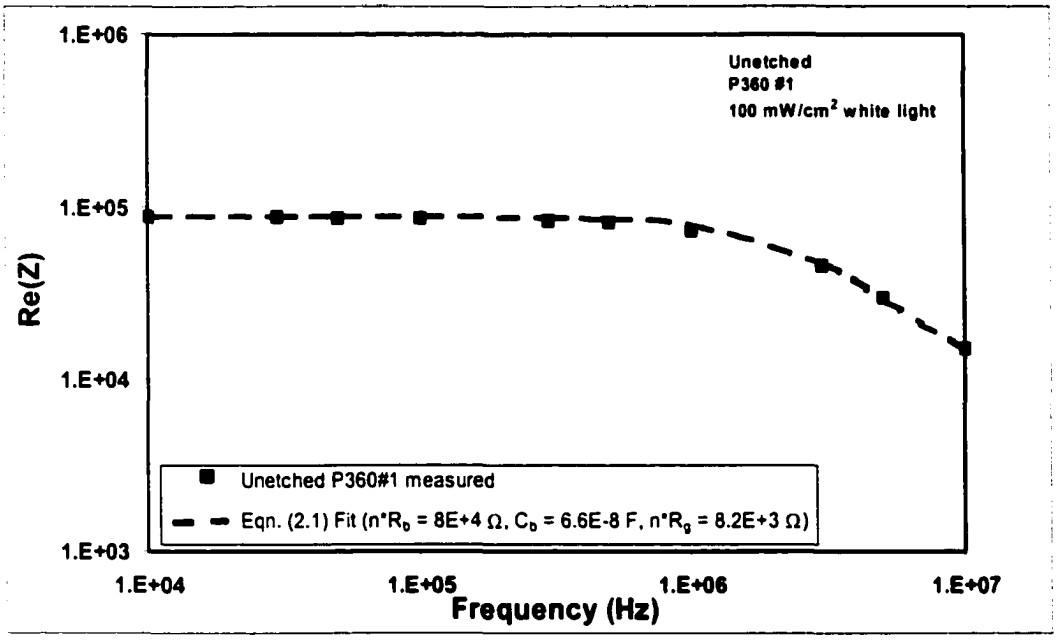

(a)

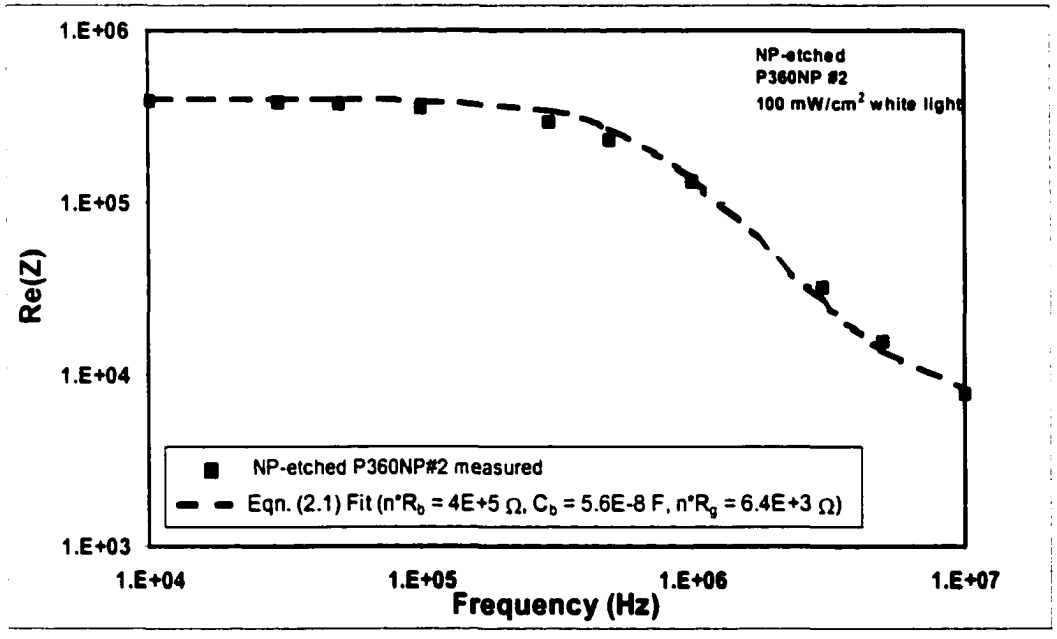

Figure 5.5 ***Re(Z)*** **vs. frequency under illumination for unetched (a) and NP-etched (b) films. Also, shown is the fit from the simple electrical model for polycrystalline films as given by Eqn. (2.1).**

magnitude higher in frequency as seen in Figure 5.5. Thus, the feedback time constant, τ, becomes much greater than $R_{LF}C_D$ and only ω_{LF} and ω_{HF} breakpoints are observed. As a result of this, Pike and Seager's feedback theory is not necessary to explain the data taken under illumination.

In contrast to the large photoconductivity of the grain boundaries in the unetched sample, the NP-etched film does not show as much of a change in grain boundary resistance from dark to light, as the fitted value of nR_b is reduced by about 80%. The dark and light illumination results indicate that the NP-etch has passivated many of the grain boundary surface states. Yet, the relatively high grain-boundary resistance of the NP-etched sample compared to its bulk resistance still indicates a grain-boundary barrier. This can be explained by the presence of a different material at the grain boundary, where the barrier is then mostly due to a heterojunction barrier that is formed in the valence band between the two materials, and therefore less dependent on illumination due to the reduction of interface states. This is also consistent with the fact that the NP-etch has been documented to remove cadmium from lattice, and leaves a layer of elemental tellurium on the grain surfaces.[40] This is depicted in the sketch shown in Figure 5.6(a). Tellurium at thicknesses greater than 50 Å is a highly conductive p-type semiconductor with a bandgap of 0.33 eV.[40] A type I band lineup between tellurium and CdTe has been found, and the valence band offset has been measured by Niles et. al.[40] as approximately 260 meV. The heterojunction barrier and energy band diagram is shown in Figure 5.6(b). Niles et. al.[40] also claim that the CdTe band bending is also 260 meV, however this appears to be a maximum. This barrier band bending value will be compared to

measurements of the grain-boundary barrier height, V_{b0}, of the NP-etched sample discussed next in section 5.5.1.

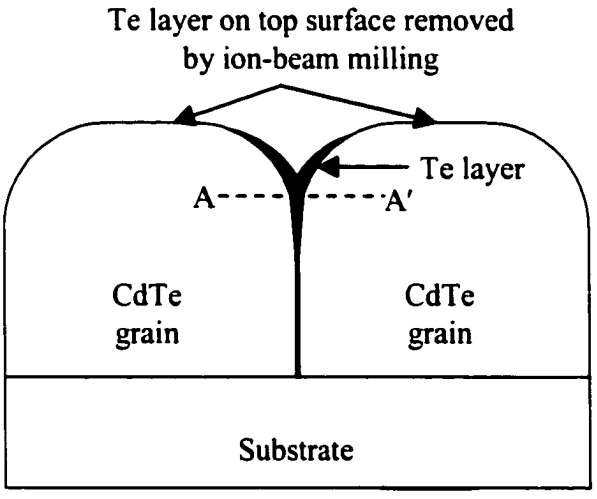

(a)

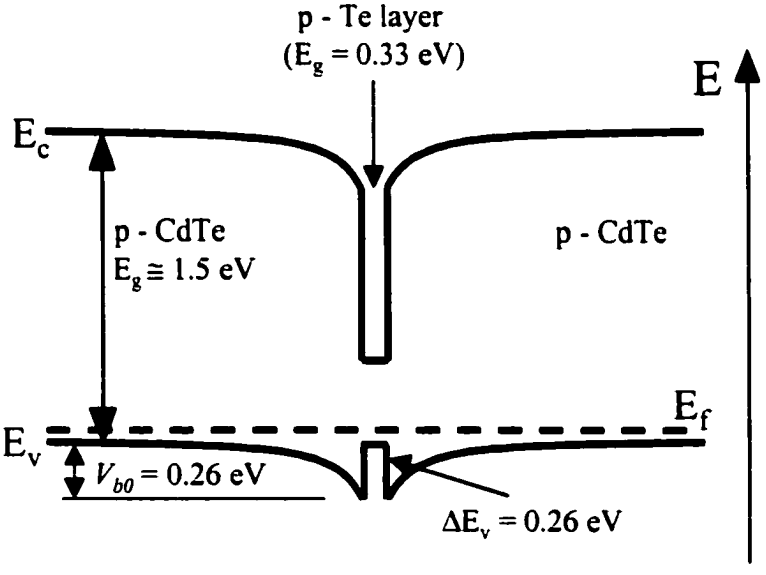

(b)

Figure 5.6 **(a) Conceptual sketch of a tellurium-rich layer left in the grain-boundaries after an NP-etch. The tellurium-rich layer on the back surface is removed by ion-beam milling. (b) Energy band diagram for the region depicted by line AA′ in (a), and as determined found by Niles et al.[40] for CdTe and thick, highly conductive tellurium (>50 Å).**

5.5 Polycrystalline Current vs. Temperature Measurements

Measurements of current versus temperature were performed on several samples of polycrystalline CdTe, which were processed differently as described in chapter 4. The polycrystalline measurements do not have the luxury of well-developed alternative techniques to measure the grain-boundary barrier properties as with bicrystal samples. Consequently, the grain-boundary density-of-states is not well defined. As discussed in chapter 3, the two-step thermally-assisted tunneling model uses an assumed energy dependence of the grain-boundary density-of-states. Thus, when fitting to current versus temperature data, the value of E_{ta} given in equation (3.17) was systematically varied while E_{td} was left as an additional fitting parameter. The effect of this assumption and its effects on V_{b0} and E_{00} are discussed in further detail in Appendix D.

5.5.1 NP-etch vs. Unetched; Barrier Heights and Doping

The current versus temperature data for unetched and NP-etched samples were fit to the different conduction models presented in chapter 3. As discussed earlier, the value of N_b was limited to 10^{17} cm^{-3} during the fitting of the thermionic emission/drift-diffusion model. Current flow in samples with N_b greater than 10^{17} cm^{-3} is dominated by thermally-assisted tunneling for a given barrier height as exemplified in Figure 3.4 in chapter 3.

An example of the best fit for each of the conduction models is shown in Fig. 5.7 for the unetched sample (a) and the NP-etched sample (b). As can be seen from the figure, the two-step thermally-assisted tunneling model gives the best fit (r^2 = 0.998) for the tunneling model was 0.81 eV, and E_{00} was about 17 meV. For comparison, the two-step thermally-assisted tunneling model yields V_{b0} = 1.092 and $E_{00} \cong 23$ meV. Good fits (r^2 >

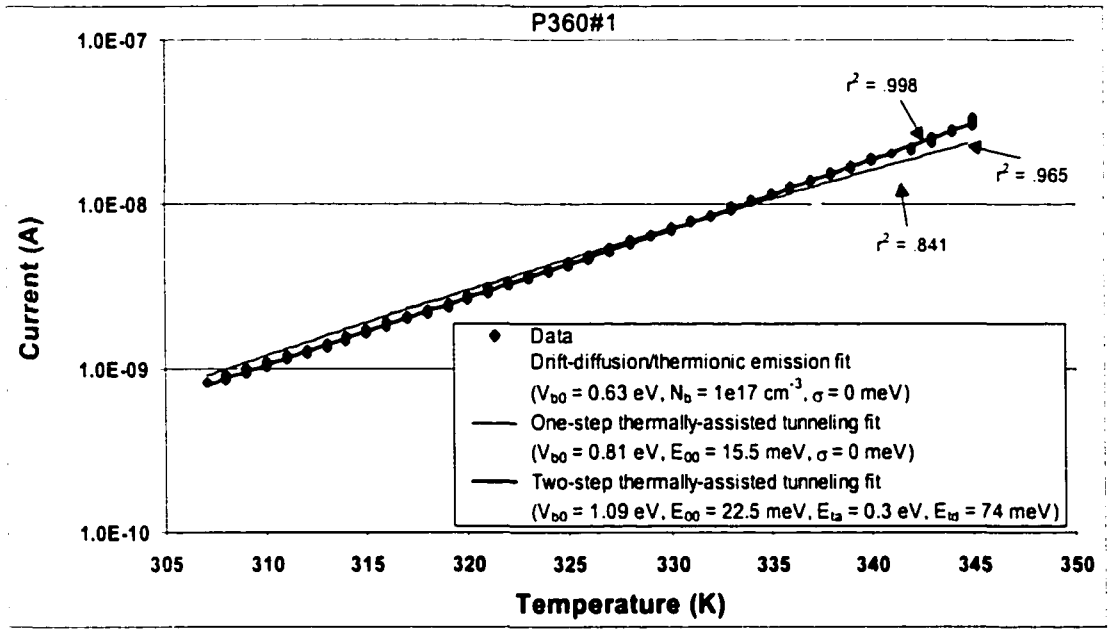

(a)

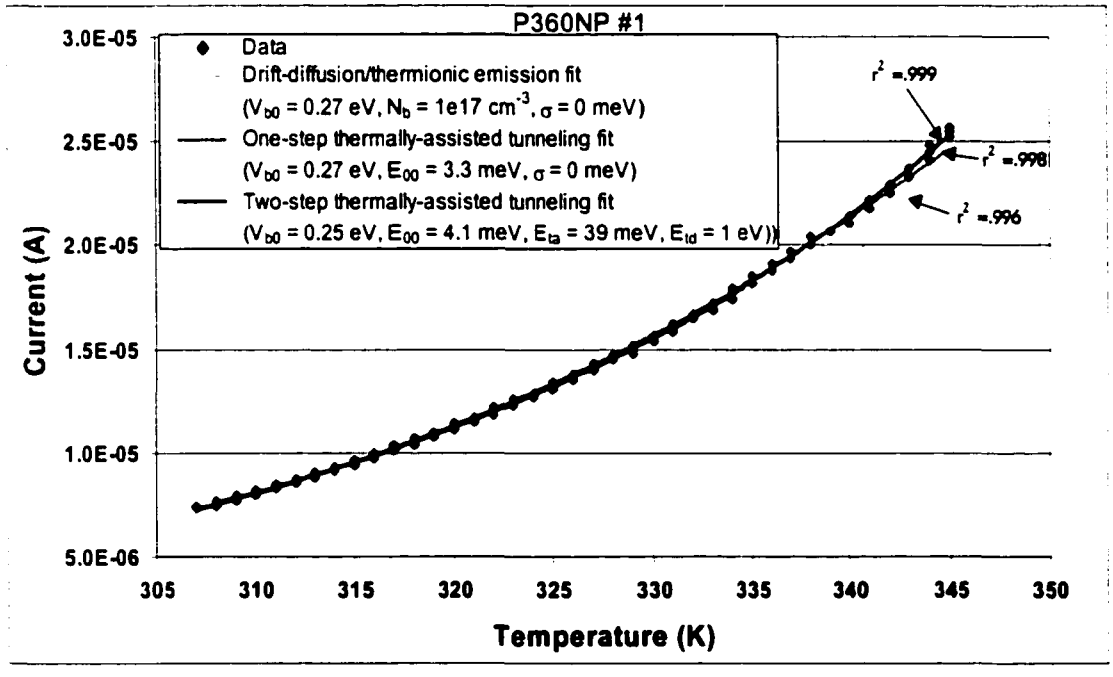

(b)

Figure 5.7 **Theoretical conduction model fits to current vs. temperature data from unetched (a), and NP-etched CdTe films (b). The full film thickness of 10 μm was used during the fitting of the unetched film, while an effective conduction thickness of 0.1 μm was used during the fitting of the NP-etched film.**

0.996) were also obtained for the NP-etched samples as shown in Fig. 5.7(b). In this case, the thermionic/drift diffusion model fits almost as well as the thermally-assisted tunneling model. However, the fits to this sample yielded large values for the grain boundary inhomogeneity, σ_s, when the full film thickness of 10 μm was used (not shown). This indicates that the NP-etch created a non-uniform grain-boundary barrier height over the film thickness. Indeed when a film thickness of 0.1 μm or less was used to simulate a thin, dominant conduction layer, then better fits could be attained with much lower barrier heights and no inhomogeneity. The lower barrier height is consistent with the four orders of magnitude lower resistivity for the NP-etched samples as shown in Table 5.2. The thickness used for the fitting of the NP-etched sample is discussed further in section 5.5.1.1. Using the smaller conduction layer thickness, a barrier height of 0.27 eV was obtained for V_{b0} using the thermionic/drift-diffusion fit, with the maximum N_b value of 10^{17} cm^{-3}. This value of N_b indicates that thermionic emission dominates over drift-diffusion. Similarly, the one-step thermally-assisted tunneling fit found V_{b0} = 0.27 eV and E_{00} = 3.3 meV (N_b = 1.2x10^{17} cm^{-3}). This good correlation between models is to be expected, since the fit value of N_b is about 10^{17} cm^{-3}, which is the doping value where a thermionic emission conduction mechanism begins to be dominated by thermally-assisted tunneling. The reduced doping level in the vicinity of the grain-boundary may be a result of the etching away of a highly doped outer region of the grain. Finally, the two-step thermally-assisted tunneling model was used to fit the NP-etch samples. In order to simulate the p-type, Te semiconductor in the grain boundary with the two-step model, some modifications were made with the normal fitting procedure. In this case the value of E_{td} was set to 1 eV, which effectively sets N_{td} = N_{ti} in equation (3.17) and

simulates a low density-of-states in the forbidden gap. The value of E_{ta} was left as a fitting parameter, and simulates the $E^{1/2}$ dependence of the valence band density-of-states with an exponentially increasing grain-boundary density-of-states. A conduction thickness of 0.1 μm was also used for this case and as discussed earlier. This resulted in an excellent fit ($r^2 > 0.999$) as shown in Figure 5.7, and yielded the following fitting parameters; $V_{b0} = 0.25$ eV, $E_{00} = 4.1$ meV, and $E_{ta} = 39$ meV. Thus the barrier height is slightly lower and the doping is slightly higher than the values as obtained from the one-step thermally-assisted tunneling model and drift-diffusion/thermionic emission model. However, the difference between the models may be related to the poor simulation of the Te valence band density-of-states used in the two-step thermally-assisted tunneling model.

To better understand the nature of grain-boundary changes due to the NP-etch, grain boundary measurements were also performed under 1-sun illumination. While the fit is not shown, the barrier height of the NP-etched sample during illumination was reduced to $V_{b0} \cong 0.18$ eV using the one-step model, compared to 0.27 eV in the dark, while the unetched barrier height went to zero compared to 0.81 eV in the dark. The relatively unchanged barrier height between the light and dark for the NP-etched sample is an indication of a more passivated grain boundary, which means that there are less electrically active defect states at the grain boundary. The effect of illumination on a grain boundary was discussed previously in section 5.4. Again, this relative independence from illumination can be explained by the presence of a different material (tellurium) in the grain boundaries after the NP-etch. It was discussed previously that the NP-etch preferentially etches Cd from the grain boundaries and creates Te-rich grain

boundaries.[40] As postulated earlier in section 5.4 and Figure 5.6, this material forms a heterojunction barrier for holes due to type I band offsets between the new material and the CdTe. Thus, the heterojunction barrier between CdTe and Te should not have as much dependence on illumination as the defect-rich grain-boundaries.

5.5.1.1 NP-etch Effects vs. Film Thickness

Using the same technique as in section 5.5.1 above, several samples were analyzed to determine the effects of the NP-etch versus depth or post ion-beam-milled CdTe thickness. Recall the impetus for this study versus depth was to help clarify the effects of the backside NP-etch on the front-side grain boundaries and PL, as discussed in chapter 1. Figure 5.8 plots the value of V_{bo} as determined using the one-step thermally-assisted tunneling model for each of the NP-etched samples that have been ion-beam-milled down to various depths. Ion-beam-milled companion samples that were not etched were measured for comparison. Four samples were processed at each film thickness: two unetched and two NP-etched as described in chapter 4, and are identified by single data points for each sample. From this plot, we see that the NP-etch losses its effects on the barrier height after 5 μm of film have been removed.

A conduction layer thickness of 0.1 μm was used during the fitting of the NP-etched samples with film thicknesses of 10 μm and 7.5 μm. The conduction thickness used for the fitting of the NP-etched samples was determined as follows. The measured film thickness of sample P360NP is about 10 μm, however various film thicknesses were tried during the fitting of this sample to simulate a thin, but highly conductive layer. When a film thickness of 10 μm was used, the best fits were obtained with large values of σ_s (>

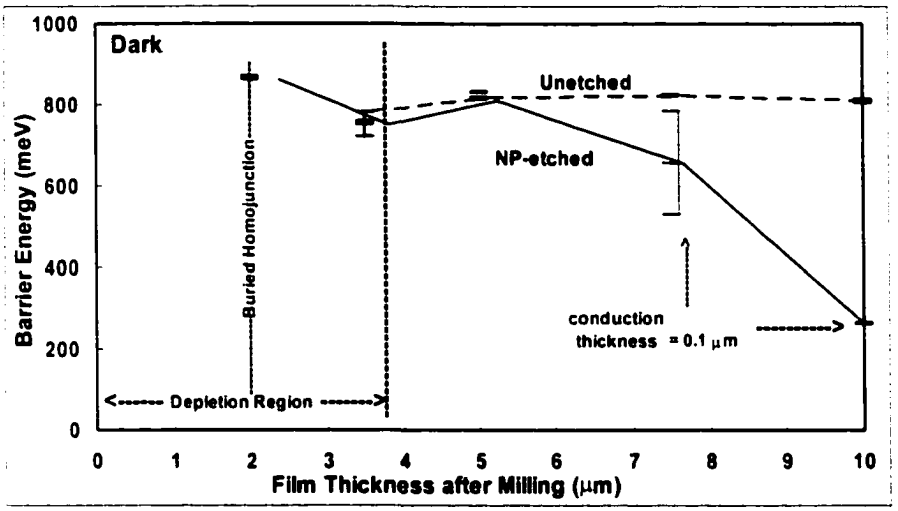

Figure 5.8 **Grain-boundary barrier height versus film thickness after ion-beam-milling for unetched and NP-etched films. Lines are drawn through the average of two values as indicated by the error bars.**

Position 0 in Figure 5.8 above.

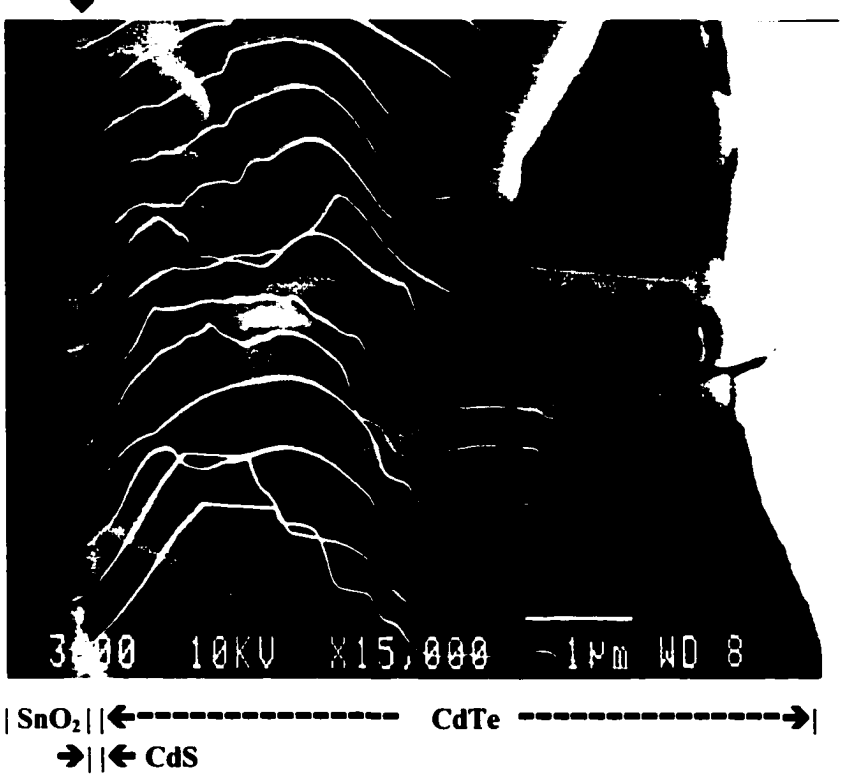

Figure 5.9 **EBIC line scans superimposed on an SEM image of a NP-etched film in cross-section. The peak in the induced current line scans indicates a buried homojunction. The EBIC was performed by Rick Matson at the NREL.**

100 meV) and yielded similar barrier heights as unetched samples. However, the unetched samples do not show any barrier height inhomogeneity. This result is consistent with the fact that the NP-etch only etched part way down the grain boundaries. Thus, a large variation in the barrier height is expected. When using a 0.1 μm thickness to simulate a thin conductive layer, no inhomogeneity was observed, $\sigma_s = 0$, and the fits were better then when using the full 10 μm film thickness.* The better fitting film thickness of 0.1 μm was used for the 10 μm thick sample in Figure 5.8 and for the determination of the NP-etched barrier height. Only one of the two samples showed this effect at the milled down thickness of 7.5 μm, and the effect was not observed for samples milled down more than this.

The barrier height results for the NP-etched samples are consistent with a model of a elemental Te on the CdTe surface as portrayed by Niles et al.[40] and as shown in Figure 5.6. In the study by Niles, he found that the band-bending (V_{b0} herein) between CdTe and Te was 0.26 eV for a thick tellurium layer, and 0.59 for a thin tellurium layer (<50Å). In addition, based on a compositional depth profile of polycrystalline CdTe, Niles et al. found that the Te-rich signal (above 50% [Te]/[Cd+Te]) quickly decreased from the surface for about 0.2 μm. At this point the signal decreased more slowly, and extended down to 1.2 μm before it was no longer detectable. Thus, if the band-bending between CdTe and the tellurium at the grain-boundary form the barrier for the NP-etched sample, this would indicate a smaller barrier height at the surface (0.26 eV) and increasing to 0.59

* This treatment is not inconsistent with the applied inhomogeneity theory, as the distribution of barrier heights is assumed to be Gaussian in shape. Thus, a thin but dominant conduction layer with lower values of the barrier height would violate this assumption, and require a separate analysis for the dominant conduction layer.

as the tellurium layer becomes thinner with depth. This result is consistent with the results of Figure 5.8 herein, except here we have shown evidence that a thin layer of tellurium (NP-etch) extends down for a minimum of 2.5 μm.

To better understand the results of Figure 5.8 for films milled down below 5 μm, cross-sectional electron-beam-induced-current (EBIC) measurements were performed on unmilled, NP-etched devices (no lift-off). This is shown in Figure 5.9, where several EBIC line-scans at different positions are superimposed onto the SEM image of the film cross-section. The theory of EBIC on pn-junctions indicates that the peak in the cross-sectional line-scans occurs at the electrical junction.[85] Assuming that this is correct, then the electrical junction occurs about 2.5 μm into the CdTe film and is therefore a buried homojunction as shown by the peak in the EBIC line-scans. The n-type region in the CdTe may develop as a result of diffusion from the underlying layers during the cell processing. Thus, even after the CdTe lift-off, the buried homojunction would remain. A buried homojunction would deplete the adjacent 1-2 μm, again as evidenced in the EBIC line-scans, and possibly affect the in-plane electrical measurements up to a film thickness of 5 μm. The in-plane electrical results below 5 μm are therefore difficult to interpret. Thus the conclusions from this section of this dissertation will be based on results for film thicknesses greater than 5 μm.

5.5.1.2 Stability of N-P etch vs. Unetched

The 10-μm-thick samples were periodically measured over 9 months to determine the stability of the barrier-reducing etch. The unetched 10 μm samples were also measured over time for comparison, and the results are plotted in Figure 5.10. All samples were

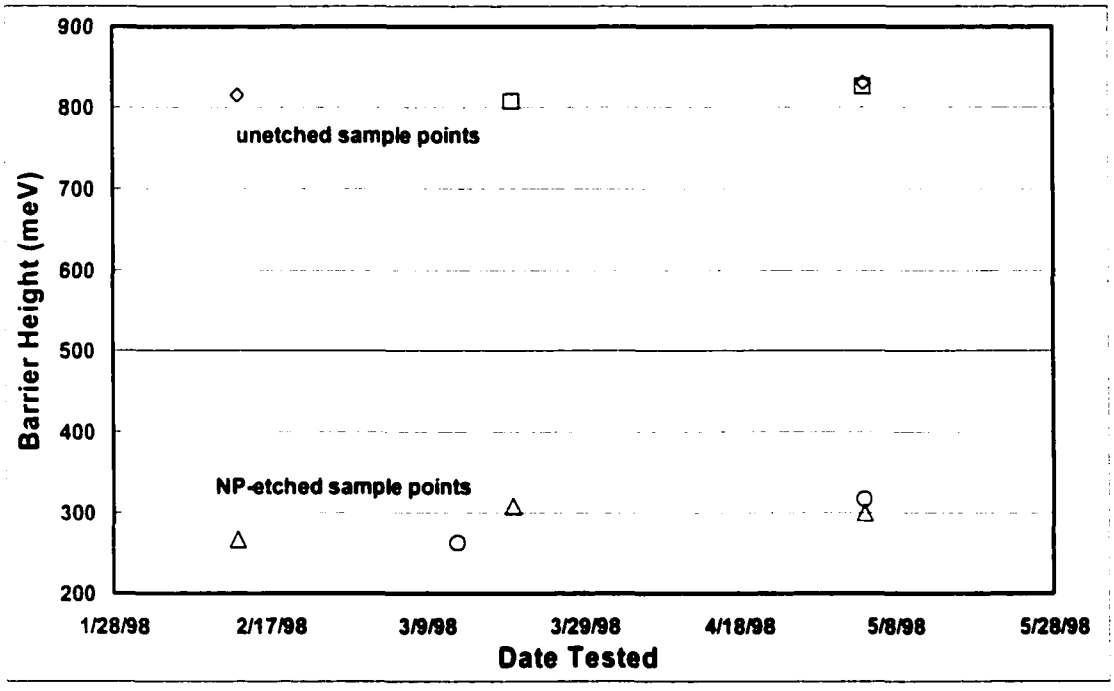

Figure 5.10 Stability of unetched and NP-etched samples over a period of three months.

left in room atmosphere during this time. The different symbols correspond to different samples. Looking at the first three points in time, it can be seen that the unetched samples remained relatively stable, whereas the NP-etched samples changed. This change is most likely due to oxidation of the tellurium in the grain boundaries. The oxidation of tellurium has been shown in a previous study using X-ray photoelectron spectroscopy.[40] In that study, the $TeO_2/[Te+TeO_2]$ ratio went from about 0 to 0.3 in a few hours. Thus, it is likely that the NP-etched samples underwent some oxidation before the first samples were measured. However, the results show that the grain-boundary barrier height was still changing even after several months. The results of figure 5.10 also indicate that the barrier height appears to be stabilizing to a lower value than unetched samples, despite the initial increases. It is possible that the same instability that affects the grain boundaries found here would also affect the Schottky barrier back

contacts relying on the tellurium-rich back-surface interface layer of the NP-etch. A change in the dark barrier height from 0.27 eV to 0.35 eV can increase the barrier resistance by an order of magnitude. Thus the instability found here may be important for devices relying on the NP-etch to create a stable, low resistance back contact.

Finally, during the measurements of samples in the NP-etched study just presented, the applied voltage was an order of magnitude higher, and the temperature range was about half that of the later samples used for the source plate usage study and the $CdCl_2$ study. Thus, the grain boundary values for the unetched samples in this study are likely to be slightly different than that of similarly treated samples measured later for the other studies.

5.5.2 Effect of $CdCl_2$ Treatment

Most of the samples studied in this dissertation received the $CdCl_2$ treatment as a normal part of their processing. As stated earlier in chapter 1, this $CdCl_2$ treatment is essential for the creation of high-efficiency solar cells. To determine the effects of this treatment on the in-plane electrical properties, several CdTe films were lifted-off without the $CdCl_2$ treatment. As shown in section 5.1.1, the grain size and number of grain boundaries per unit distance did not noticeably change as a result of the $CdCl_2$ treatment. In each case, the one-step and two-step thermally-assisted tunneling conduction models both yielded excellent fits to the current vs. temperature data. In the case of the one-step thermally-assisted tunneling model fits, the best fit for both untreated and $CdCl_2$ treated samples was achieved with no detectable inhomogeneity, $\sigma_s = 0$ meV. The effect of σ_s on the one-step thermally-assisted tunneling model fitting is discussed further in Appendix C. Examples of the thermally-assisted tunneling theoretical fits to the

untreated sample data and $CdCl_2$ treated sample data are given in Fig. 5.11 a and b, respectively. The V_{b0} and E_{00} values averaged for all samples and contact spacings are shown in Table 5.4. Recall that each of three different samples were cut, with one-half being $CdCl_2$ treated, and the other half left untreated. A total of seven contact spacings were tested from the three halves of each condition. The data from the fits to both models indicate that the untreated samples have a significantly lower barrier height and doping in the vicinity of the grain boundary. For the two-step thermally-assisted tunneling model, the average barrier height for the untreated samples was 788 meV, which can be compared to 1090 meV for the $CdCl_2$ treated samples. This difference is greater than three standard deviations, which is based on the variation of all like-treated samples. For the one-step thermally-assisted tunneling fits, the average barrier height was 752 meV for the untreated samples, and 952 meV for the $CdCl_2$ treated samples. In this case, the difference between treatments is over two standard deviations. Referring to the E_{00} values in Table 5.4, the two-step thermally-assisted tunneling fits yielded an average E_{00} value of 10.4 meV for the two untreated samples, and 23.8 meV for the $CdCl_2$ treated samples. This corresponds to a doping of 1.2×10^{18} and 6.3×10^{18} cm^{-3}, respectively. The difference between the two E_{00} values is greater than three standard deviations. For the one-step thermally-assisted tunneling, the average E_{00} value was about 11 meV for the two untreated samples, and about 30.6 meV for the $CdCl_2$ treated samples. This corresponds to a doping of 1.3×10^{18} and 1.0×10^{19} cm^{-3}, respectively. The difference is slightly less than three standard deviations for the sample-to-sample variability.

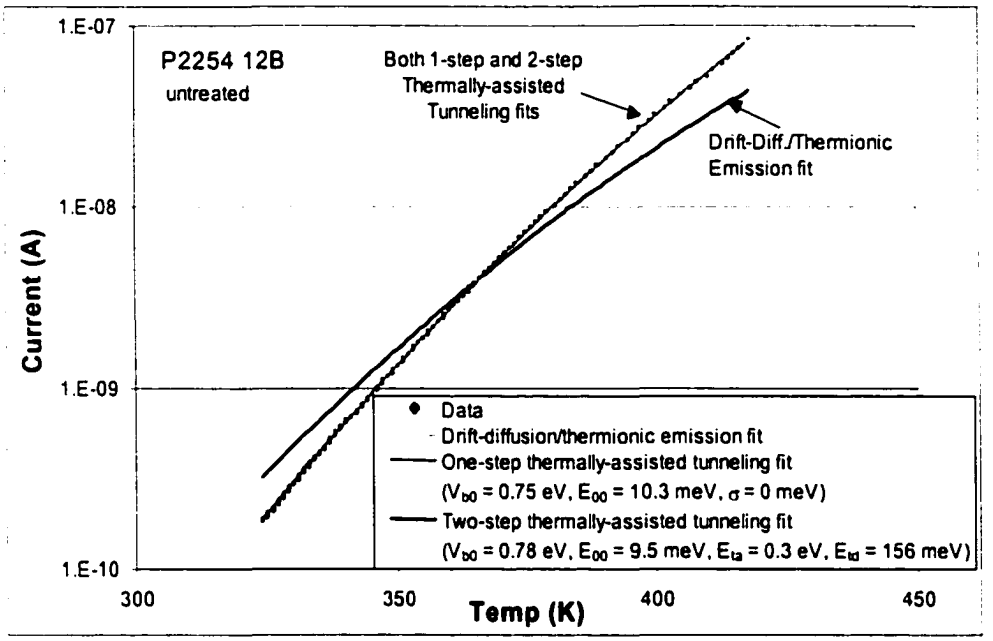

(a)

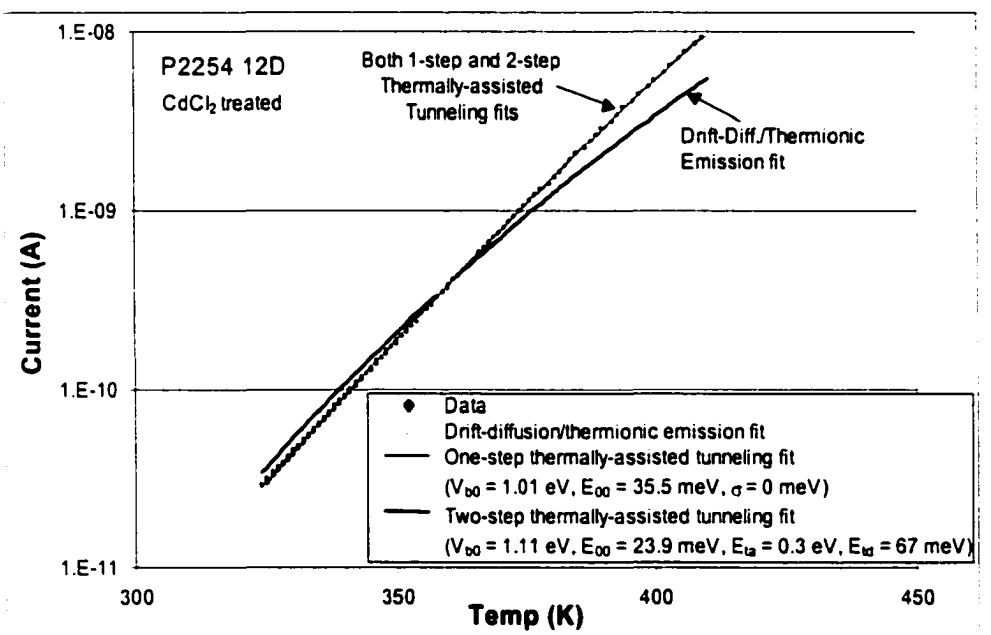

(b)

Figure 5.11 Theoretical conduction model fits to current vs. temperature data from untreated (a), and $CdCl_2$ treated CdTe films (b).

Table 5.4 **V_{bo} and E_{oo} as determined by the one-step and two-step thermally assisted tunneling models, for untreated and companion $CdCl_2$ treated samples. Also, shown is $qV_{bo} - E_m$, or the energy below the top of the barrier where the tunneling current peaks.**

		qV_{bo} (meV)		E_{oo} (meV)		$qV_{bo} - E_m$ (meV)	
		One-step	Two-step	One-step	Two-step	One-step	Two-step
untreated	Avg.	752	788	11.0	10.4	32	95
	Std. Dev.	18	27	2.7	1.6		
$CdCl_2$ treated	Avg.	952	1090	30.6	23.8	266	510
	Std. Dev.	62	73	5.0	2.3		

The average value of E_{oo} was found to be 30.6 meV for the $CdCl_2$ treated samples from the one-step thermally-assisted tunneling model. Although this value of E_{oo} is large, it is less than 56 meV, corresponding to the minimum $2kT$ (minimum temperature of 50 °C) during the current versus temperature measurement. Thus, the high values do not to violate the approximations of $E_{oo} < 2kT$, which were made in the development of the theory. For the two-step thermally-assisted tunneling, $E_{oo} < 28$ meV, corresponding to the minimum kT during the current versus temperature measurement. Thus, approximations of $E_{oo} < kT$, which were made in the development of the theory, are not violated here either. Also included in Table 5.4 is the value of $qV_{bo} - E_m$, which corresponds to the energy at which the tunneling current peaks below the top of the barrier. This is calculated for both the one-step and the two-step thermally-assisted tunneling models using equation (3.24a) and (3.24b), respectively. None of these values approach $\frac{1}{2}E_g$ or 0.75 eV for CdTe, which would invalidate the approximation used in the theoretical development (chapter 3) of using a single band model and no mixing of conduction and valence band states. In addition, the peak in the tunneling current is not

near the bottom of the barrier, which would invalidate the approximation of using a constant density of valence band states.

In summary, the model fitting from this study indicates an increased barrier height and doping in the vicinity of the grain boundary from the $CdCl_2$ treatment, and that the in-plane transport occurs via thermally-assisted tunneling. While both thermally-assisted tunneling models predict the same trends with the $CdCl_2$ treatment, the two-step model predicts 4 – 10 % higher V_{b0} values and 10 – 30 % lower E_{00} values than the one-step model. Finally, the one-step model does not predict any barrier height inhomogeneity from either untreated or $CdCl_2$ treated samples.

5.5.3 Effect of Source Plate Usage

As discussed in chapter 4, the CdTe source plate has been shown to oxidize with usage. The purpose of this study was to determine the effect of this source plate oxidation on the in-plane electrical properties of films after the $CdCl_2$ treatment. The effect of the $CdCl_2$ treatment was discussed in the previous section. One difference in the analysis of these samples compared to others in this dissertation is that these samples were potentially contaminated during the ion-beam-milling of the surface before lift-off. Apparently, the ion-beam was not aligned correctly which resulted in sputtering of the stainless steel (Ni and Mo) from the ion gun walls. However, after the ion-beam was realigned, other samples (P2254, P2257 & P2258 discussed in the $CdCl_2$ study) were processed, and measured to have grain boundary parameters that differ by less than one standard deviation than the samples in this study. This can be seen by comparing the $CdCl_2$ treated values shown in Table 5.4 (previous page), with the results given in Figure 5.12. Thus, we conclude that effects of the potential contamination are not significant.

As in the previous samples, the thermally-assisted tunneling conduction models fit the current vs. temperature data best for all the samples irrespective of the source plate usage. Again, the two-step thermally-assisted tunneling model (avg. r^2 = 0.997) tended to fit better than the one-step thermally-assisted tunneling model (avg. r^2 = 0.982). And again, the best fits for the one-step thermally-assisted tunneling model indicate that there is no detectable inhomogeneity, or $\sigma_s = 0$. The effect of σ_s on the one-step thermally-assisted tunneling model fitting is discussed further in Appendix C.

Figure 5.12 (a) shows the barrier height as determined from the one-step thermally-assisted tunneling fit, and (b) shows the barrier height as determined from the two-step thermally-assisted tunneling fit. Each point on the graph represents the average barrier height as determined from several contact spacings on the sample, and each side of the error bar represents one standard deviation. The vertical y-axis separates the two different runs (source plates), and the x-axis is labeled according to that sample's position in the sequential run of samples grown with a particular source plate. For example, a sample labeled #2 was the second sample grown from a particular source plate. The graphs show that the average grain-boundary barrier height varies from 800 meV to just over 1000 meV, however there is no systematic barrier height dependence on the source plate usage. In addition, there does not appear to be a run-to-run dependence either. This lack of systematic dependence may be in part due to the considerable variation found in some samples. In particular, the standard deviation observed in sample p1019, #2 in run $(8/25)_b$, and sample p902, #2 in run $(8/25)_c$, was much larger than other like-treated samples. The large variation may be due to the relatively new source plate for these

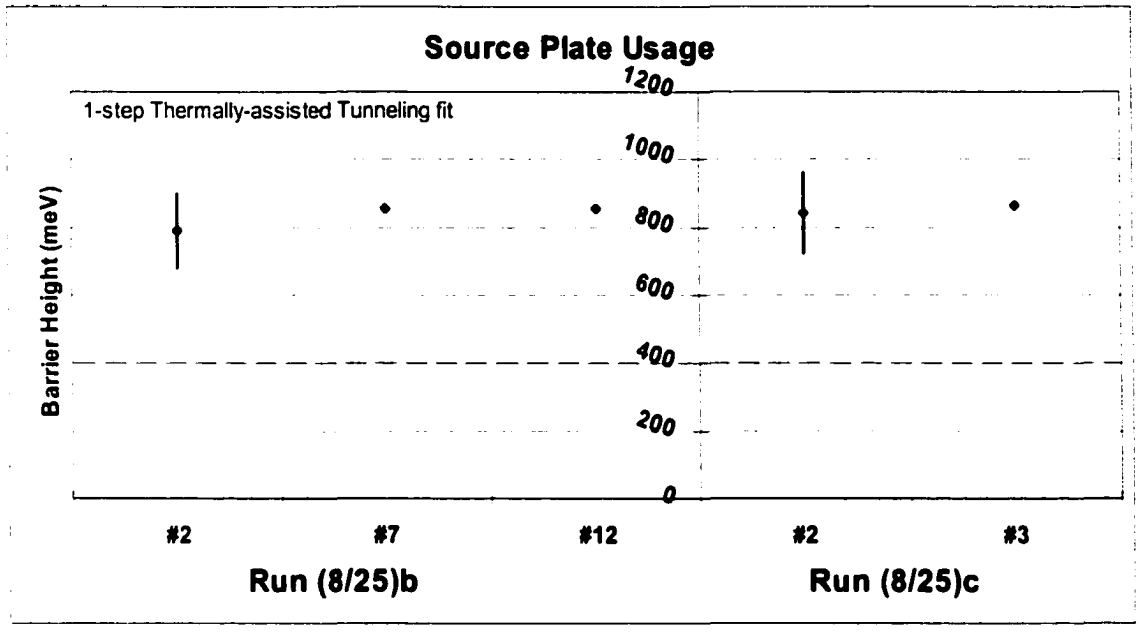

(a)

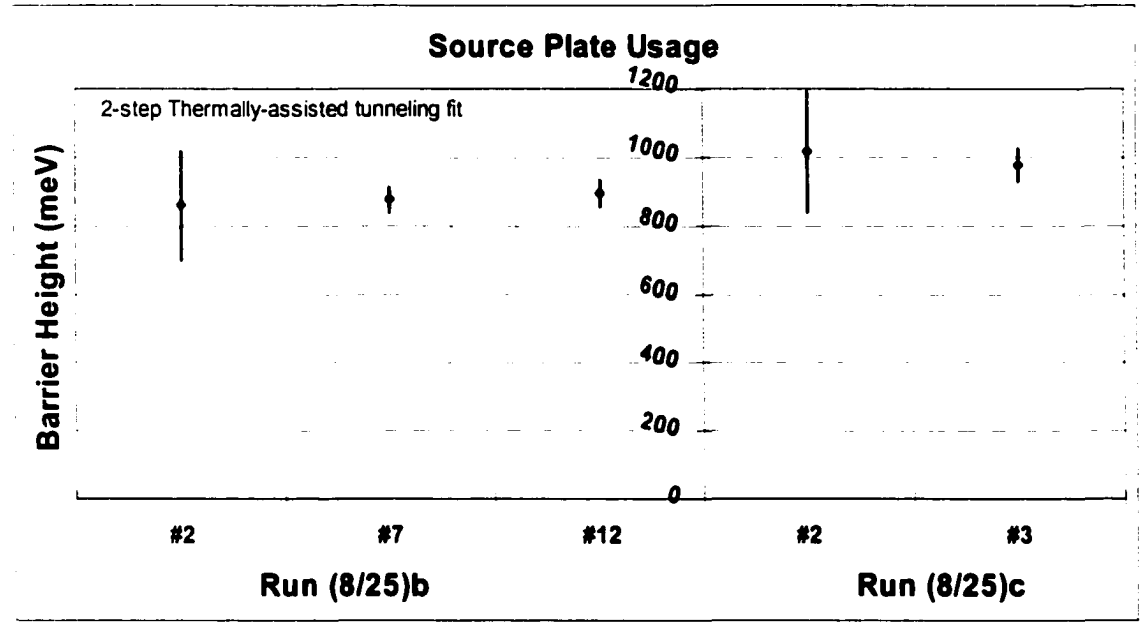

(b)

Figure 5.12 **Grain boundary barrier height (V_{bo}) as a function of source plate usage, and as determined from fitting current vs. temperature data with the 1-step thermally-assisted tunneling model (a), and the 2-step thermally-assisted tunneling model (b). Two source plate runs are shown with 3 samples from run $(8/25)_b$ on the left of the vertical axis and two samples from run $(8/25)_c$ on the right. Each point on the graph represents the average from several contact spacings on the sample, and each side of the error bar represents one standard deviation.**

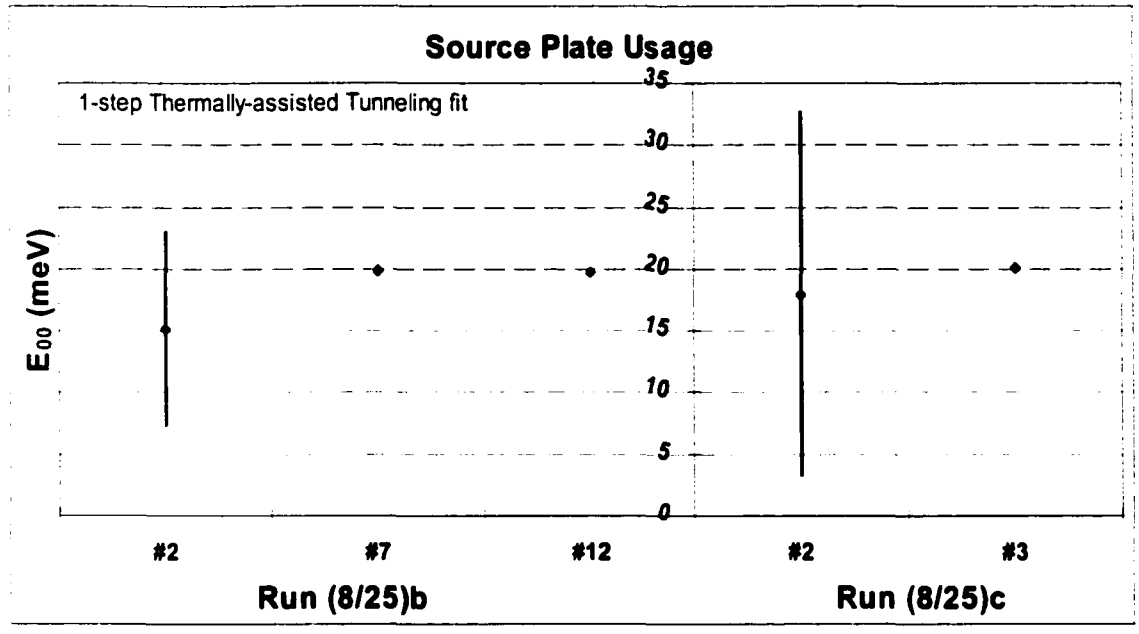

(a)

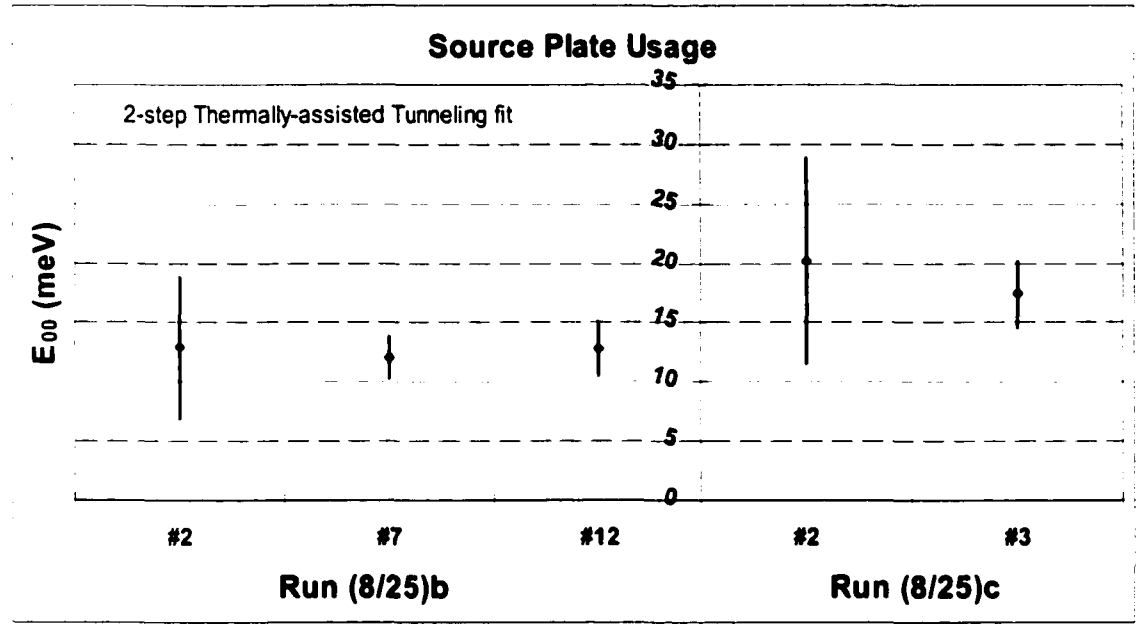

(b)

Figure 5.13 **E_{00} as a function of source plate usage, and as determined from fitting current vs. temperature data with the 1-step thermally-assisted tunneling model (a), and the 2-step thermally-assisted tunneling model (b). Two source plate runs are shown with 3 samples from run $(8/25)_b$ on the left of the vertical axis and two samples from run $(8/25)_c$ on the right. Each point on the graph represents the average of several contact spacings on the sample, and each side of the error bar represents one standard deviation.**

samples. It has been previously observed that there is a large variation in solar cell performance with the first few samples grown from a new source plate.[86]

Similar results were found for E_{00} as shown in Figure 5.13. Again, no trends were observable with source plate usage due to the variability found in the number 2 sample. The average value of E_{00} varied from 15 meV to 20 meV for the one-step fit, and from 12 meV to 20 meV for the two-step fit. A E_{00} value of 10 meV corresponds to a doping level of $N_b = 10^{18}$ cm^{-3}, and a E_{00} value of 20 meV corresponds to $N_b = 4\text{x}10^{18}$ cm^{-3}.

The results from this study show that there is no observable trend in the in-plane electrical properties of $CdCl_2$ treated films due to source plate usage.

5.6 Polycrystalline Dark Band Diagram – The Big Picture

The results of the current versus temperature fitting, and the high-frequency resistance measurements allow the grain-boundary dark band diagram to be determined. As an example, this was done for the untreated and unetched sample using values from the one-step thermally-assisted tunneling fit, as shown by the solid line in Figure 5.14(a). The bulk, p-type doping level, N_a, was estimated to be about $7\text{x}10^{14}$ cm^{-3} and was determined from the equation (5.2) using the value of the high-frequency resistance, device geometry, and a nominal value of 60 cm^2/v-s as the hole bulk mobility in crystalline CdTe. Thus, the separation in energy between the Fermi level and valence band in the bulk, E_{vf}, is approximately 0.25 eV. This bulk doping level is more than three orders of magnitude less than the doping in the vicinity of the grain boundary, $N_b = 1.3\text{x}10^{18}$ cm^{-3}, as determined from E_{00}. This non-uniform p-type doping bends the valence bands, which is reflected in the conduction band and gives rise to a minority-carrier barrier, V_{eb}:[66]

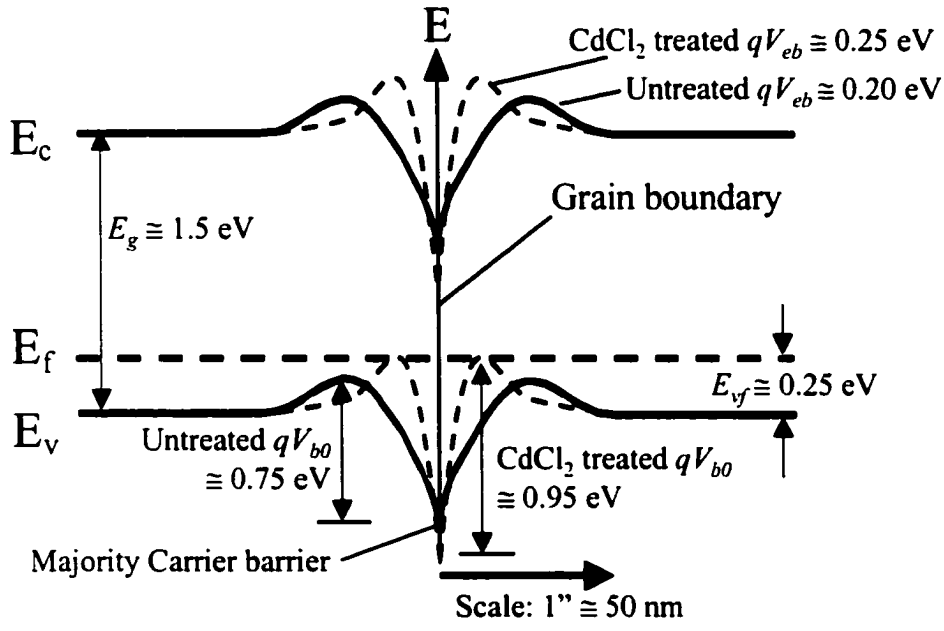

(a)

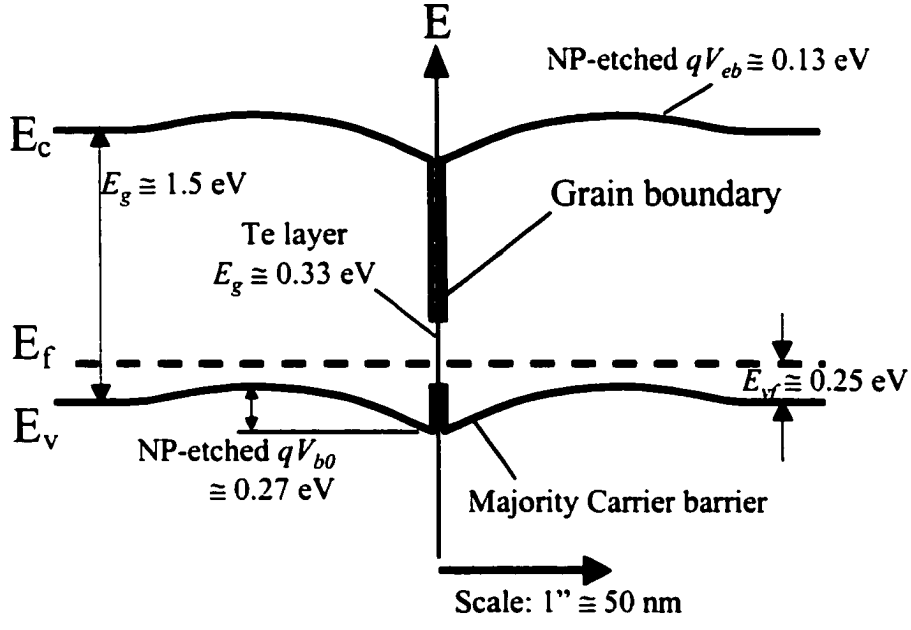

(b)

Figure 5.14 **Polycrystalline CdTe dark band diagram for (a) untreated (solid line) and $CdCl_2$-treated (dashed line) thin films, and (b) NP-etched (and $CdCl_2$-treated). The band diagrams was determined from the one-step thermally-assisted tunneling model fit to current versus temperature data and the high frequency Re(Z) data.**

$$V_{eb} = \left(\frac{kT}{q}\right)\ln\left(\frac{N_b}{N_a}\right) \quad \text{eV} \tag{5.3}$$

Thus, V_{eb} is about 0.20 eV using the above stated values for N_a and N_b giving E_{vf} at the peak of this barrier of 0.05 eV. The exact spatial extent of the highly doped region is unknown. However, the grain-boundary depletion region is about 26 nm, as determined from equation (3.9). The majority carrier barrier height is about 0.75 eV as determined from V_{b0} using the one-step thermally-assisted tunneling model, and the position of the Fermi level at the grain boundary, Φ_{gb}, is calculated to be 0.80 eV. The areal density of net positive charge at the grain boundary can also be found by using the principal of conservation of charge at the grain-boundary and in the surrounding fields of the depletion regions. Thus, the total negative charge or ionized acceptors in the surrounding depletion regions approximately equals the positive charge at the grain-boundary, or:

$$N_{gb} \cong 2x_d N_b \quad \text{cm}^{-2} \tag{5.4}$$

Thus, $N_{gb} \cong 6.8\text{x}10^{12}$ cm^{-2} using the one-step thermally-assisted tunneling model. A similar band diagram can be drawn from the two-step thermally-assisted tunneling model (not shown), but in this case the values for V_{b0}, Φ_{gb} and V_{eb} are 0.79 eV, 0.85 eV and 0.19 eV, respectively, and $x_d \cong 28$ nm.

The band diagram for the $CdCl_2$ treated sample is given as the dashed line in Figure 5.14(a) and is calculated in the same manner as described above. Here $\Phi_{gb} \cong V_{b0} = 0.95$ eV with a grain boundary depletion region of only 11 nm, and $V_{eb} = 0.25$ eV. Also, $N_{gb} \cong 1\text{x}10^{12}$ cm^{-2}. Again, a similar band diagram can be drawn from the two-step thermally-assisted tunneling model, but in this case the values for V_{b0}, Φ_{gb} and V_{eb} will be 1.09 eV, 1.10 eV and 0.24 eV, respectively, and $x_d \cong 14$ nm.

The minority carrier barrier, V_{eb}, from the variable grain doping has advantages for solar cell devices. If the minority carrier barrier is wider than electron mean-free-path length, then this layer could act to reflect the minority carriers from the grain boundary and effectively separate the oppositely charged free carriers. Thus, the minority carrier barrier could temper the grain-boundary (majority carrier) barrier effects on minority-carrier recombination. The vapor $CdCl_2$ treatment, which increases the doping in the vicinity of the grain boundary, would therefore act to increase the minority carrier lifetime. This would be consistent with longer minority carrier lifetimes as measured by time-resolved photoluminescence,[87] and increased solar cell open circuit voltage after $CdCl_2$ treatments, which also imply longer lifetimes.

The dark band diagram can also be drawn for the NP-etched grain boundary at the back of the device, and is shown in Figure 5.14(b). Here the grain boundary is shown with thick (>50Å) p-type tellurium layer. This layer forms a heterojunction barrier with the adjacent CdTe as discussed in sections 5.4, 5.5.1.1 and Figure 5.6. Thus, the position of the Fermi level is no longer dependent on the pinning at the grain boundary, as the tellurium unpins it.[40] Again, the grain-boundary parameters as determined by the one-step thermally-assisted model fits are shown in the figure. Thus, the values for V_{b0}, Φ_{gb}, and V_{eb}, are 0.27 eV, 0.39 eV and 0.13 eV, respectively, and $x_d \cong 57$ nm. In this case, the drift-diffusion/thermionic emission model yielded nearly identical fitted values due to the lower barrier height and near grain boundary doping. The values from the two-step thermally-assisted tunneling model are also similar, but are based on an approximation to the Te-layer density of valence band states.

The NP-etched band diagram changes gradually back to the $CdCl_2$ treated diagram with depth into the CdTe film (thickness of Te layer) as discussed in section 5.5.1.1. This indicates that the Te-rich grain boundaries, extend like tails down toward the depletion region of the CdTe film. These "tails" are believed to be beneficial to the solar cell device as the low barrier height and high conductivity in the Te-rich boundary may effectively extend a low resistance back contact toward the depletion region.[39]

Chapter 5 references

[80] D.L. Levi, H.R. Moutinho, F.A. Hasoon, B.M. Keyes, R.K. Ahrenkiel, M. Al-Jassim, L.L. Kazmerski, and R.W. Birkmire, First WCPEC, pp. 127-131, (1994).

[81] A. Swartzlander, personal communication, April, (2000).

[82] D. Albin, personnal communication, February, (2000).

[83] D. Albin, personnal communication, October, (2000).

[84] H. C. Card and E. S. Yang, *IEEE Trans. on Electron Devices*, **24**(4), p397, (1977).

[85] D.B. Holt, "SEM Microcharacterization of Semiconductors," edited by D. B. Holt and D. C. Joy, Academic Press, San Diego, (1989).

[86] D. Albin, personal communication, March, (2000).

[87] D. Levi, personal communication, March (2000).

Chapter 6

SUMMARY and CONCLUSIONS

The in-plane electrical properties of the polycrystalline CdTe films, as processed for CdS/CdTe solar cells, were evaluated at various stages in the solar cell processing. The in-plane electrical characterization was made possible using a new technique that enables the CdTe layer to be lifted-off and electrically isolated after the deposition and any subsequent processing of the CdTe. It was found that the dark, DC electrical conduction is dominated by grain-boundary scattering at all stages of the CdTe processing. This was determined from room temperature measurements of the real part of the impedance versus frequency, and comparison with a simple electrical model for the polycrystalline thin film. Several theoretical models for the DC conduction across grain-boundaries were examined, and an analytical solution was developed for both a one-step and a two-step, thermally-assisted tunneling mechanism. These analytical solutions enabled quick and unproblematic curve fitting of the in-plane current versus temperature data. When compared to other conduction mechanisms, it was found that conduction mechanisms using thermally-assisted tunneling transport gave the best fit to the current vs. temperature data from nearly all of the lift-off CdTe samples tested herein. From these fits, several grain boundary parameters were determined. These parameters are: the grain-boundary barrier height and its inhomogeneity, and the doping in the vicinity of the grain boundary. From these fitted parameters, the grain-boundary depletion width can be

calculated. The sensitivity of the fitted parameters to other model variables such as the voltage per grain-boundary, cross-sectional area, effective mass, and grain boundary capture coefficient was found to be minimal. Order of magnitude changes to a model variable usually resulted in changes to the grain-boundary parameters of much less than 10%. This insensitivity is an advantage over capacitance techniques in which the grain-boundary parameters are either directly proportional to a model variable or proportional to the square-root of a model variable.

Several processing effects were evaluated using the in-plane electrical characterization. When using the one-step thermally-assisted tunneling model, it was found that the NP-etch reduced the dark grain-boundary barrier height from about 0.8 eV to 0.27 eV. The NP-etched barrier height correlates with measurements of the Te to CdTe valence-band offsets found in a previous study.[40] This previous study showed that the NP-etch preferentially etched down grain-boundaries and created a thin p-type tellurium layer on CdTe surfaces. The barrier height reduction from the NP-etch was measured to extend down a minimum of 2.5 μm. Thus, the etch could act to extend the effective back contact of the solar cell devices down the grain-boundaries. This would have implications on the device performance.[39] It was also found that the effects of the NP-etch are initially unstable as evidenced by increases in the barrier height over a period of three months. The instability of the etched grain boundary may be indicative of unstable Schottky barrier back contacts that were formed using the NP-etch. An increased Schottky barrier height from the NP-etched back contact could result in severe increases in the back-contact series resistance of devices.

The effect of the vapor $CdCl_2$ treatment on the grain-boundary parameters was also determined. The vapor $CdCl_2$ treatment was found to increase the as-processed CdTe barrier height by about 0.2 eV, and increase the doping in the vicinity of the grain-boundary from about 1 x 10^{18} cm^{-3} to 6 – 10 x 10^{18} cm^{-3}. The change in barrier height and doping was similar in both the one-step and two-step thermally-assisted tunneling model fits. The effect of the increased doping from the $CdCl_2$ treatment may actually "passivate" the grain-boundary by increasing the *minority* carrier barrier height.

Lastly, the effects of the source plate usage on the CdTe deposition was examined. It was found that the first couple of samples with a new source plate gave widely variable results. Otherwise, there did not appear to be any trends in the grain-boundary parameters with the source plate usage, despite a well-documented oxidation of the source with source plate usage.

One of the most significant findings of this research is the very high acceptor doping levels in the vicinity of the grain-boundary. This implies that a variable doping level exists in the grains of all samples, with doping near the grain boundary that is several orders of magnitude higher than the bulk concentration. This information has allowed a detailed development of the grain-boundary band diagram, which predicts a minority-carrier (conduction-band) barrier due to the variable doping. We postulate that if the minority carrier barrier is wider than electron mean-free-path length, then this layer could act to reflect the minority carriers from the grain boundary and temper the grain-boundary barrier effects on minority-carrier recombination. Thus, the vapor $CdCl_2$ treatment, which increases the doping in the vicinity of the grain-boundary, should act to increase the minority carrier lifetime. This has been corroborated with longer minority

carrier lifetimes as measured by time-resolved photoluminescence, and increased solar cell open circuit voltage after $CdCl_2$ treatments, which imply longer lifetimes.

Finally, a new technique has been established for the electrical characterization of polycrystalline thin films. This technique of fitting in-plane current versus temperature data to analytical models of conduction across grain-boundaries, enables the quantification of several electrical parameters associated with the grain boundary. The methods developed herein are not limited to polycrystalline CdTe, the grain-boundary parameters of other promising thin film photovoltaic materials, such as $CuInSe_2$ based alloys, can also be studied as a function of variable processing. In addition, the technique established here can be used for future CdTe studies. Future work should include studying the effects of post deposition heat treatments in air, the effect of humidity, and the influence of variable CdS deposition parameters on the CdTe grain-boundary parameters. The grain-boundary parameters found herein, and in future studies, can be used in newly emerging two-dimensional device emulation programs. This should aid in the development of accurate models of the thin film solar cell device operation.

Appendix A

Derivation of the Current-Voltage Relation for Two-Step, Thermally-Assisted Tunneling across Grain Boundaries

In this Appendix the current-voltage relation describing the current crossing a grain boundary or back-to-back parabolic energy barriers, will be derived using the band-state to defect-state thermally-assisted tunneling model. This model is described in section 3.2.2.2 and Appendix B.

The derivation starts with the current-voltage relation for one side of the boundary barrier as derived in Appendix B. Thus, the **net** thermally-assisted tunneling current for carriers tunneling from the band-states on one side of grain boundary barrier to the defect-states at the grain boundary, can be written as:

$$J^{2s} = J_0^{2s}\left[\exp\left(\frac{qV_1}{E_{02}}\right) - 1\right] \qquad A/cm^2 \qquad \text{(A.1)}$$

where V_1 is the voltage applied across one side of the grain boundary. J_0^{2s} and E_{02} are given in equations (3.21a) and (3.21b) respectively. A high density of grain boundary defect states allows the variation of the Fermi level at the grain boundary to be neglected for small applied biases.[54,57] Thus, the current from the grain boundary to either side of the barrier is independent of the small applied bias to a first order approximation and is

equal to zero bias current or J_0^{2s}. With equation (A.1), the current from one side of the grain boundary to the grain boundary can then be written as:

$$J_f^{2s} = J_0^{2s}\left[\exp\left(\frac{qV_f}{E_{02}}\right)\right] \quad A/cm^2 \tag{A.2}$$

for the forward biased side, and

$$J_r^{2s} = J_0^{2s}\left[\exp\left(-\frac{qV_r}{E_{02}}\right)\right] \quad A/cm^2 \tag{A.3}$$

for the reverse biased side. The different voltages and currents are illustrated in the grain boundary band diagram as shown in Figure A.1. Also, included in the figure are currents for the one step thermally-assisted tunneling process.

In steady-state, there is no accumulation of charge at the grain boundary. Thus, a relation for the voltage distribution across the grain boundary can be found by equating current from both forward and the reverse biased sides to the grain boundary with those exiting the grain boundary, or

$$J_f^{2s} + J_r^{2s} = 2J_0^{2s} \tag{A.4}$$

Using equations (A.2) and (A.3) this yields the following expression:

$$\exp\left(\frac{qV_f}{E_{02}}\right) + \exp\left(-\frac{qV_r}{E_{02}}\right) = 2 \tag{A.5}$$

Combining equation (A.5) with $V = V_f + V_r$, gives the relation for the voltage distribution across the grain boundary:

$$\exp\left(\frac{qV_f}{E_{02}}\right) = 2\left[1 + \exp\left(-\frac{qV}{E_{02}}\right)\right]^{-1} \tag{A.6}$$

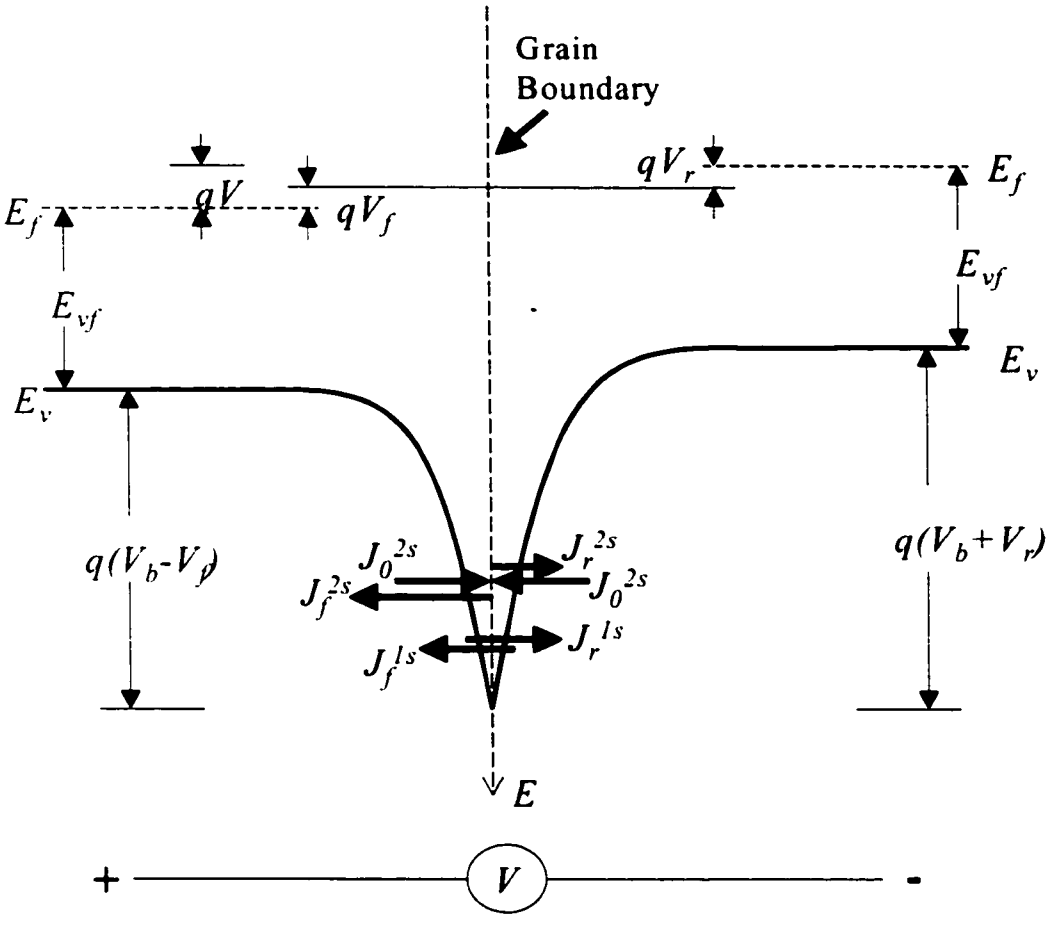

Figure A.1 **Illustration of the grain boundary energy band diagram with p-type bulk showing the different voltages and currents for thermally-assisted tunneling (two step with *2s* superscript and one step with *1s* superscript).**

To determine the current-voltage relation, an equation for the current across the grain boundary is written. For a dominant two step process, the total current is the same as the current across one side of the grain boundary as given in equation (A.1), or $J^{2s} = J_f^{2s} - J_0^{2s} = -(J_r^{2s} - J_0^{2s})$. Thus for the forward biased side:

$$J^{2s} = J_0^{2s}\left[\exp\left(\frac{qV_f}{E_{02}}\right) - 1\right] \quad A/cm^2 \tag{A.7}$$

Combining equation (A.6) with (A.7), finally yields the current-voltage relation for current crossing the grain boundary, or

$$J = 2J_0^{2s} \tanh\left(\frac{qV}{2E_{02}}\right) \quad A/cm^2 \tag{A.8}$$

In the likely event that $E_t >> kT$ and $E_{00} < kT$ for the 300°K - 400°K measurement, where E_t is defined in equation (3.16), and E_{00} is defined in equation (3.14), then from equation (3.18b), $E_{02} \approx kT$. Thus in the limit of small applied bias kT can be substituted for E_{02} in equations (A.7) and (A.8), which yields equations (3.2) and (3.1), respectively. Recall γ in equation (3.1) has no meaning for the two step process and is therefore set to 0.

A similar analysis can be done for drift-diffusion and thermionic emission and was first done by Mueller.[63] Mueller's analysis takes into account the grain boundary capture coefficient, γ. The analysis can also be extended to the one step thermally-assisted tunneling process by considering the fact that at least some negligible but finite *two-step* thermally-assisted tunneling is occurring (γ is finite). The voltage distribution across the two sides of the grain boundary can then be defined according to equation (A.7). Thus, using $J^{1s} = J_f^{1s} - J_r^{1s}$ and the one step expressions for J_f^{1s} and J_r^{1s}, then equation (3.1) can again be derived. This approach also requires $E_{01} \approx 2kT$, which occurs for $E_{00} < 2kT$ in a similar manner as described above.

Appendix B

Analytical Solution for Band-State to Grain Boundary Defect-State Thermally-Assisted Tunneling Current

This appendix will derive an analytical solution for the thermally-assisted tunneling current between the band-states and the grain boundary defect-states. This current is given in integral form for an as:

$$J = \frac{4\pi q N_{ti}}{h}\left(\frac{1}{kT} - \frac{1}{E_{ta}}\right)^{-1}\int_0^{\infty} T_d(E_p)\{f_1(E_p) - f_2(E_p)\}\exp\left(\frac{E_p}{E_{ta}}\right)dE_p \quad A/cm^2 \quad \text{(B.1)}$$

which is the same as equation (3.20) given in Chapter 3. In equation (B.1), E_p is the carrier energy in the direction perpendicular to the barrier, and the integration over tranverse momentum has already been performed. N_{ti} and E_{ta} characterize the exponentially increasing density of grain boundary states as given in equation (3.17), and $T_d(E_p)$ is the transmission probability for the band-state to defect-state transition as given in equation (3.19).

The applied voltage (V_1) dependence can be factored out of $\{f_1(E_p)-f_2(E_p)\}$ by assuming Boltzmann occupancy functions for $f_1(E_p)$ and $f_2(E_p)$ for the high-energy process, and by using $qV = E_{f2} - E_{f1}$, where E_{f1} and E_{f2} are the Fermi levels on side 1 and side 2 of the barrier, respectively. Thus,

$$f_1(E_p) - f_2(E_p) = f_1(E_p)\left[1 - \exp\left(-\frac{qV_1}{kT}\right)\right]\exp\left(\frac{E_{vf}}{kT}\right) \qquad \text{(B.2)}$$

where E_p is relative to the band edge and E_{vf} is as defined in Figure A.1. With the voltage dependence factored out of the occupancy functions, equation (B.1) can be written as:

$$J = \frac{4\pi q N_{ti}}{h}\left(\frac{1}{kT} - \frac{1}{E_{ta}}\right)^{-1} \exp\left(\frac{E_{vf}}{kT}\right)\int_0^{\infty} T_d(E_p) f_1(E_p)\exp\left(\frac{E_p}{E_{ta}}\right)dE_p\left[1 - \exp\left(-\frac{qV_1}{kT}\right)\right]$$

A/cm2 (B.3)

The product $T_d(E_p)f_1(E_p)\exp(E_p/E_t)$ in equation (B.2) will be hereafter referred to as $P(E_p)$. If $P(E_p)$ is approximated by a Gaussian distribution, $G(E_p)$, with the same curvature and peak at energy, E_m, then an analytical solution to equation (B.1) can be obtained. The approximation of total energy $E \cong E_p$ in $T_d(E_p)$ is not necessary for this approach, and an analytical solution can still be obtained by performing a binomial expansion on the pre-exponential factor of equation (3.19). However, the binomial expansion will not be carried through in the fit to the Gaussian distribution for this Appendix. When using the Gaussian distribution, the approximation of $E \cong E_p$ results in an error of about 7% in the magnitude of J at 300°K and 10% at 400°K when using nominal values of qV_{b0} = 0.75 eV and E_{00} = 0.01 eV. The change in the magnitude of J from 300°K to 400°K due to the approximation of $E \cong E_p$ is insignificant compared to the orders of magnitude change in current observed experimentally. Thus, with $T_d(E,E_p) \cong T(E_p)$, then $P(E_p)$ can be written as:

$$P(\alpha) = \exp\left(-\frac{qV_b}{kT}\left[\alpha\left(1 - \frac{kT}{E_t}\right) + \frac{kT}{E_{00}} y(\alpha) \right] \right) \tag{B.4}$$

where the substitution $\alpha = E_p/qV_b$ has been made. The factor $y(\alpha)$ in equation (B.4) is determined from equation (3.14) modified for the band-state to defect-state tunneling, i.e. without the factor of 2 in the exponent, and is given as:

$$y(\alpha) = (1-\alpha)^{1/2} - \alpha \ln\left[\frac{1+(1-\alpha)^{1/2}}{\alpha^{1/2}} \right] \tag{B.5}$$

$P(\alpha)$ attains a maximum when the exponent in equation (B.4) attains a minimum. Finding this maximum is not trivial, but can be guessed from the maximum for the Schottky barrier,[66] which occurs when $\alpha_m = [\cosh(\phi)]^{-2}$, where $\phi = E_{00}/kT$. Thus, guessing $\alpha_m = [\cosh(\phi)]^{-2}$, where $\phi = E_{00}(1/kT - 1/E_t)$, gives the minimum as confirmed in Figure B.1 for T = 300°K and T = 400°K. Thus $P(\alpha_m)$ becomes:

$$P(\alpha_m) = \exp\left(-\frac{qV_b}{kT}\left[\frac{kT}{E_{00}} \tanh\left(E_{00}\left[\frac{1}{kT} - \frac{1}{E_t} \right] \right) \right] \right) \tag{B.6}$$

So that the shape of a Gaussian distribution may be later fit to $P(\alpha)$, the curvature of $P(\alpha)$ is determined by taking the second derivative of the exponent evaluated at α_m, or:

$$\frac{d^2}{d\alpha^2}\ln(P(\alpha))\Big|_{\alpha_m} = \frac{qV_b \cosh^2\left(E_{00}\left[\frac{1}{kT} - \frac{1}{E_t}\right]\right)}{2E_{00}\tanh\left(E_{00}\left[\frac{1}{kT} - \frac{1}{E_t}\right]\right)} \tag{B.7}$$

Equations (B.6) and (B.7) are more easily derived by substituting $\alpha = [\cosh(\phi)]^{-2}$ into equations (B.4) and (B.5). A Gaussian distribution, which is centered on α_m, is written as:

$$G(\alpha) = C\exp\left(-K[\alpha - \alpha_m]^2\right) \tag{B.8}$$

where C and K are constants. To fit $G(\alpha)$ to $P(\alpha)$, C is set to $P(\alpha_m)$ from equation (B.6), and the curvature of the $ln[G(\alpha)]$ or $-2K$ is set to the curvature of $ln[P(\alpha)]$ or equation (B.7). $P(\alpha)$ and the fitted $G(\alpha)$ are shown in Figure B.1 using assumed values of V_{b0} = 0.75 eV and E_{00} = 0.02 eV.

With $P(\alpha)$ set to a Gaussian distribution, the integral of equation (B.1) can be evaluated analytically using the definite integral for a Gaussian distribution, or:

$$\int_0^{qV_b} G(\alpha)d\alpha \cong \int_{-\infty}^{\infty} G(\alpha)d\alpha = C\left(\frac{\pi}{K}\right)^{1/2} \tag{B.9}$$

Substituting in for C and K, and using $dE_p = qV_b d\alpha$ in equation (B.1), then J can be found as:

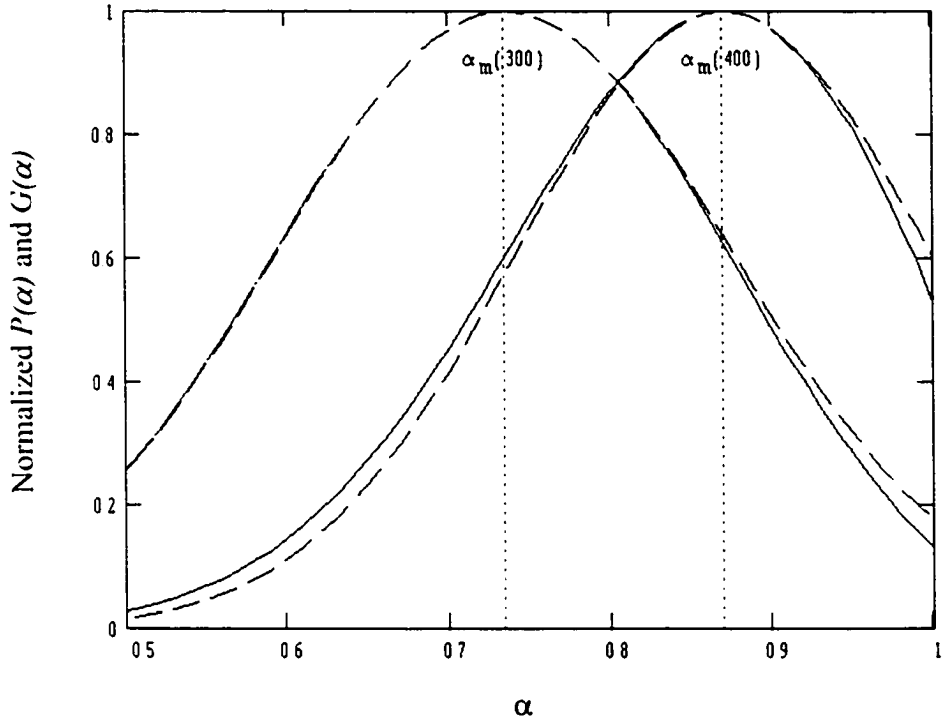

Figure B.1 ***P(α)* from equation (B.4), normalized to *P(α_m)* at 300°K and 400°K (solid lines) as a function of α or E_t/qV_b, and the corresponding fitted Gaussian Distributions, G(α), (dashed lines), normalized to G(α_m). Vertical dotted lines are α_m or E_m/qV_{b0} as determined from equation (3.22b). Values of V_{b0} = 0.75 eV and E_{00} = 0.02 eV were assumed.**

$$J = \frac{4\pi q N_{ti}}{h}\left(\frac{1}{kT}-\frac{1}{E_{ta}}\right)^{-1}\frac{E_{00}\sqrt{4\pi q V_b}}{\sqrt{E_{02}}\cosh\left(\frac{E_{00}}{kT}-\frac{E_{00}}{E_{ta}}\right)}\exp\left(\frac{E_{vf}}{kT}\right)\exp\left(-\frac{qV_b}{E_{02}}\right)\left[1-\exp\left(-\frac{qV_1}{kT}\right)\right]$$

A/cm2 (B.10)

where E_{02} is as given in equation (3.21b). The band bending V_b is a function of the applied voltage or $V_b = V_{b0} - V_1$, where V_{b0} is the zero-bias band bending. Thus, equation (B.10) becomes:

$$J = J_0^{2s}(V_1)\exp\left(\frac{qV_1}{E_{02}}\right)\left[1-\exp\left(-\frac{qV_1}{kT}\right)\right] \qquad A/cm2 \qquad (B.11)$$

where

$$J_0^{2s} = \frac{4\pi qN_{ti}}{h}\left(\frac{1}{kT}-\frac{1}{E_{ta}}\right)^{-1}\frac{E_{00}\sqrt{4\pi qV_{b0}}}{\sqrt{E_{02}}\cosh\left(\frac{E_{00}}{kT}-\frac{E_{00}}{E_{ta}}\right)}\exp\left(\frac{E_{vf}}{kT}\right)\exp\left(-\frac{qV_{b0}}{E_{02}}\right)$$

A/cm2 (B.12)

Here $J_0^{2s}(V_1)$ is a function of V_1 via the $\sqrt{V_b}$ term in equation (B.11). If $V_{b0} >> V_1$, or small applied bias, then V_1 can be neglected in the $\sqrt{V_b}$ term, or $\sqrt{V_b} \cong \sqrt{V_{b0}}$, and $J_0^{2s}(V_1) \cong J_0^{2s}$, where J_0^{2s} is as given in equation (3.21). Also, in the likely event that $E_{ta} >> kT$ and $E_{00} < kT$ for the 300°K - 400°K measurement, where E_t is defined in equation (3.17), and E_{00} is defined in equation (3.15), then from equation (3.21b), $E_{02} \approx kT$. When the substitution, $E_{02} \approx kT$ is taking place within an exponent, then this approximation is only valid in the case of small applied bias and is invalid for any exponential terms in V_b. Also, E_{00} is less than kT in the case that $N_b < 10^{18}$ cm^{-3}. Thus, using $E_{02} \approx kT$ and $V_{b0} >> V_1$, equation (B.11) can be written as:

$$J \cong J_0^{2s}\left[\exp\left(\frac{qV_1}{E_{02}}\right)-1\right] \qquad A/cm2 \qquad (B.13)$$

Thus, the thermally-assisted tunneling current from a band-state in the grain, through one half of the grain boundary energy barrier, and to the grain boundary defect states has been

determined. The current-voltage relation for current across the entire grain boundary using equation (B.13) is derived in Appendix A.

Following the same procedure as outlined in this appendix, J_0^{1s} for the one-step thermally-assisted tunneling can be found starting with the product $T(E_p)f_1(E_p)$ where $T(E_p)$ is as given in equation (3.14).

Appendix C

Grain-Boundary Barrier Height Inhomogeneity

The presence of grain-boundary barrier height inhomogeneity was analyzed for most of the samples using the one-step, thermally-assisted tunneling model. The standard deviation for the barrier height inhomogeneity, σ_s in equation (3.28), was systematically varied, and the average V_{b0}, and E_{00} values were determined from the best fit for each standard deviation value. The results for σ_s = 0, 30, and 60 meV are shown in Table C.1. An increased σ_s generally yielded fits with increased barrier height, and a slight decrease in E_{00} compared to the σ_s = 0 meV values. Values of V_{b0} and E_{00} were tabulated only from fits where the quality of the fit factor, r^2, was greater than 0.95. In general, r^2 decreased with increasing σ_s, and the best fits were attained with σ_s = 0. The exception was sample P360NP, which was not included in the table since it had a known barrier height inhomogeneity throughout its thickness due to the NP-etch. This was discussed in detail in section 5.5.1.1.

The effect of grain boundary barrier height inhomogeneities was also examined using the thermionic emission model to see if it could improve the fit of this model as demonstrated by Werner[53] and as discussed in chapter 2. The standard deviation for the barrier height inhomogeneities was varied, and the average barrier height, V_{b0}, and E_{00} values were determined from the best fit for each standard deviation value. Here again, the quality of the fit factor, or r^2, decreased with increasing σ_s. In no case did a finite

value of σ_s improve the generally poor fit of the thermionic emission model. The poor fits precluded tabulation of V_{b0} and E_{00} values for this model. Thus, conduction by thermionic emission is not likely as a conduction mechanism for the unetched films herein.

Table C.1 **Grain boundary parameters as a function of assumed barrier height inhomogeneity, σ_s, and as determined by numerical fitting using the one-step thermally-assisted tunneling model.**

Sample ID	V_{b0} (meV)			E_{00} (meV)			r^2 (Quality of fit factor)		
	σ_s = 0 meV	σ_s = 30 meV	σ_s = 60 meV	σ_s = 0 meV	σ_s = 30 meV	σ_s = 60 meV	σ_s = 0 meV	σ_s = 30 meV	σ_s = 60 meV
P2258C 12C	955	950	910	35.9	33.4	22.2	0.999	0.999	0.998
P2258C 12D	896	879	909	26.2	22	20.3	0.998	0.997	0.985
P2258C 35	848	848	883	23.5	21.6	20.7	0.994	0.993	0.976
P2257 12C	982	972	965	30.1	27	20.5	0.995	0.995	0.989
P2257 12D	951	936	949	27.7	23.9	20.1	0.997	0.996	0.988
P2254 12C	1019	1015	984	35.3	33	23.4	0.9965	0.9963	0.995
P2254 12D	1012	1008	974	35.5	33.2	23	0.9985	0.9984	0.9979
P1019D 12	620	649	737	3.8	4.4	6.8	0.998	0.997	0.947
P1019C 12	686	715	818	6.6	7.7	13.2	0.998	0.998	0.997
P1019B 12	862	877		19.7	19.7		0.958	0.944	0.892
P1019 08	882	890		21.5	20.7		0.991	0.988	0.953
P1019 32	823			19.6			0.953	0.938	0.9
P1019A 35	873	887	929	19.9	19.9	19.8	0.99	0.983	0.951
P972B 12	848	858	901	20.5	19.9	20	0.99	0.983	0.948
P972A 08	862	876		20	19.9		0.983	0.975	0.938
P972D 32	856	871	915	19.5	19.5	19.7	0.99	0.983	0.947
P972C 12	868	882		19.6	19.6		0.987	0.979	0.943
P972D 12	860	874		19.7	19.7		0.985	0.976	0.938
P972D 35	851	865		19.9	19.8		0.967	0.955	0.906
P991D 12	860	874		19.6	19.6		0.982	0.972	0.93
P991A 12	854			19.7	19.8		0.948	0.933	0.9
P991C 12	857	871		19.8	19.8		0.985	0.977	0.94
P991B 35	856	870		19.6	19.6		0.962	0.949	0.898
P991B 08	862	875		20.1	20.1		0.985	0.977	0.942
P902 12	979	970	930	34.8	31.8	20.8	0.997	0.997	0.996
P902 08	755	787	975	7.3	8.6	25.6	0.992	0.993	0.995
P902 35	798	856	927	11.8	16.9	20.7	0.994	0.995	0.991
P956 12	862	876		19.9	19.9		0.979	0.97	0.934
P956 08	866	878	920	20.5	20.2	20.1	0.987	0.981	0.954
P956 35	872	885	928	19.9	19.9	19.8	0.991	0.985	0.955
Avg.	866	878	914	21.3	20.8	19.8	0.985	0.980	0.954
Std. Dev.	83	75	61	7.8	6.7	4.2	0.014	0.019	0.034

Appendix D

Sensitivity to Cross-sectional area, voltage, effective mass, grain boundary carrier-capture coefficient, and grain boundary density of states.

A few parameters in the models for grain boundary conduction were fixed at an assumed value during the fitting. These parameters were the voltage per grain boundary, the cross-sectional area of conduction, and the bulk effective mass. The sensitivity of the fits to variation in these parameters was examined in the event that there was an error in the assumption or determination of their values. This was accomplished by individually varying each parameter by a fixed amount and evaluating the subsequent change in V_{b0}, E_{00} and quality of fit factor, r^2. These variations were done for both the one-step thermally-assisted tunneling model and the two-step thermally assisted tunneling model. The poor fits of the drift-diffusion/thermionic emission model precluded any meaningful interpretation of these variations to the samples herein. In addition to the parameters just mentioned, the sensitivity to the grain-boundary carrier capture coefficient, γ, for the one-step thermally-assisted tunneling model (not applicable to the two-step), was determined from the sensitivity to the cross-sectional area as they are linearly dependent parameters. Reducing γ from 1 to 0.5 would be the lowest value of γ before the two-step process dominates. For the two-step, the additional parameters for the characteristic energies of the grain boundary density of states E_{ta} and E_{td}, were also evaluated. When other

parameters were being evaluated the value of E_{ta} was fixed at 0.3 eV and E_{td} was allowed to float as an additional fitting parameter.

The sensitivity to cross-sectional area was determined by arbitrarily increasing and decreasing the area by a factor of 10. However, for the one-step thermally-assisted tunneling model, the cross-sectional area was decreased by a factor of 2, since decreases larger than this generally led to poor fits. Conveniently, this sensitivity can also be used for the $\gamma/2$ evaluation as mentioned earlier. For the sensitivity to voltage per grain boundary, the voltage was arbitrarily increased by a factor of 10 and decreased by a factor of 10. For the sensitivity to effective mass, m* was arbitrarily increased to 0.75 and decreased to 0.1 from its nominal value of 0.35. The results for each of the sensitivity factors using the one-step thermally-assisted tunneling model are tabulated in Tables. D.1 and D.2 for V_{b0} and E_{00} respectively. For the two-step thermally assisted tunneling model the sensitivity results are tabulated in Tables D.3 and D.4 for V_{b0} and E_{00} respectively. The average and standard deviation values of the fitted V_{b0} and E_{00} were computed for each of the sensitivity factors.

For the sensitivity to the cross-sectional area, V_{b0} decreases by –63 meV or –6.6% for the order of magnitude decrease in the area for the two-step, and –32 meV or –3.7% for the 50% decrease in area for the one-step. Similar results were found for E_{00}, as a decrease of -0.8 meV or -4.9% for the two-step, and -0.8 eV or -3.8% for the one-step for the decrease in cross-sectional area. For a factor of two increase in cross-sectional area, V_{b0} increases by 22 meV or 2.3%, and 21 meV or 2.4% for the two-step and one-step, respectively. Again, similar results were found for E_{00}, as an increase of 0.3 meV or 1.8%, and decrease of -0.4 eV or –1.9% for the two-step and one-step, respectively.

Table D.1 **Sensitivity of fitted barrier height, V_{b0}, to Cross-sectional area, voltage, and effective mass using the one-step thermally-assisted tunneling model.**

Sample ID	V_{b0} (meV)						
	Default case σ_s = 0 meV	Low Area A = A_{def}/2 cm^2	High Area A = A_{def}*2 cm^2	Low Voltage V=V_{def}/10	High Voltage V=V_{def}*10	Low m* m* = 0.1	High m* m* = 0.75
P2258C 12C	955	892		772	1115	850	1010
P2258C 12D	896	831	792	779	1078	813	791
P2258C 35	848	805	912	753	1036	788	919
P2257 12C	982	911	1036	833	1149	876	1041
P2257 12D	951	879	1009	819	1125	856	1014
P2254 12C	1019	958	1068	836	1175	919	1073
P2254 12D	1012	952	1060	826	1167	914	1065
P1019D 12	620	622	619	629	618	623	619
P1019C 12	686	690	682	729	679	696	682
P1019B 12	862	837	884		940	823	887
P1019 08	882	849	937		1068		944
P1019 32	823		843		880		846
P1019A 35	873	847	896		858	832	901
P972B 12	848	818	866		1007	804	869
P972A 08	862	836	886		865	821	888
P972D 32	856	832	877		1021	817	879
P972C 12	868	843	890		1028	829	892
P972D 12	860	835	882		1008	821	885
P972D 35	851	826	873		938		876
P991D 12	860	835	882		995	821	884
P991A 12	854		876		928		878
P991C 12	857	832	880		857	817	882
P991B 35	856	831	878		935	817	880
P991B 08	862	836	887		1015	820	889
P902 12	979	900	776		1154	833	776
P902 08	755	765	751	816	747	777	751
P902 35	798	832	784	796	775	832	783
P956 12	862	837	886		999	822	888
P956 08	866	838	898		1038	823	903
P956 35	872	846	897		1043	831	899
Avg.	866	836	875	781	972	818	883
Std. Dev.	83	66	98	61	142	57	100

		Delta V_{b0} (meV)					
	Default case σ_s = 0 meV	Low Area A = A_{def}/2 cm^2	High Area A = A_{def}*2 cm^2	Low Voltage V=V_{def}/10	High Voltage V=V_{def}*10	Low m* m* = 0.1	High m* m* = 0.75
Avg.	866	-32	21	-85	109	-50	17
Std. Dev.	83	26	31	95	74	42	52

Table D.2 **Sensitivity of fitted E_{00} to Cross-sectional area, voltage, and effective mass using the one-step thermally-assisted tunneling model.**

Sample ID	E_{00} (meV)						
	Default case σ_s = 0 meV	Low Area A = A_{def}/2 cm^2	High Area A = A_{def}*2 cm^2	Low Voltage V=V_{def}/10	High Voltage V=V_{def}*10	Low m* m* = 0.1	High m* m* = 0.75
P2258C 12C	35.9	31.3		21.7	45.2	27.6	39.5
P2258C 35	23.5	21.4	29.2	21.3	37.9	21.2	29.7
P2257 12D	27.7	21.7	32.2	20.6	39.3	20.8	32.5
P2254 12D	35.5	31.4	38.4	21.2	43.9	28.3	38.7
P1019D 12	3.8	5	3	8.6	1.7	5.9	2.9
P1019C 12	6.6	8.9	5.1	18.7	2.9	10.8	5
P1019B 12	19.7	19.9	19.5		19.6		19.5
P1019 08	21.5	20.7	25.7		35.4		26.3
P1019 32	19.6		19.3		16.9		19.2
P1019A 35	19.9	20	19.9		9.5		20.1
P972B 12	20.5	20.1	19.8		31.3	20.3	19.8
P972A 08	20	20.1	20		11.3	20.2	20.1
P972D 32	19.5	19.8	19.2		30.7	19.9	19.1
P972C 12	19.6	19.8	19.4		30.2	20	19.3
P972D 12	19.7	20	19.5		28.8	20	19.5
P972D 35	19.9	20	19.7		20.9		19.7
P991D 12	19.6	19.8	19.4		27	20	19.4
P991A 12	19.7		19.6		19.3		19.5
P991C 12	19.8	20	19.8		10.9	20.1	19.8
P991B 35	19.6	19.8	19.4		19.7	20	19.8
P991B 08	20.1	20.2	20.2		29.9	20.4	20.3
P902 12	34.8	27.9	7.8	21.9	45.7	21	7.6
P902 08	7.3	10.2	5.6	22.3	3.2	13	5.5
P902 35	11.8	18.8	8.6	21.1	4.7	21.2	8.3
P956 12	19.9	20	19.2		27.5	20.1	19.9
P956 08	20.5	20.4	21.6		33	20.5	21.9
P956 35	19.9	20	20		31.9	20.1	20
Avg.	21.3	20.5	19.8	20.1	26.1	20.1	20.5
Std. Dev.	7.5	5.5	8.9	3.9	13.4	4.6	9.1

	Delta E_{00} (meV)						
	Default case σ_s = 0 meV	Low Area A = A_{def}/2 cm^2	High Area A = A_{def}*2 cm^2	Low Voltage V=V_{def}/10	High Voltage V=V_{def}*10	Low m* m* = 0.1	High m* m* = 0.75
Avg.	21.3	-0.8	-0.4	-3.2	4.8	-1.5	-0.7
Std. Dev.	7.5	3.0	5.6	10.8	7.8	5.1	6.3

Table D.3 **Sensitivity of fitted barrier height, V_{b0}, to Cross-sectional area, voltage, effective mass, and grain boundary density of states using the two-step thermally-assisted tunneling model.**

Sample ID	V_{b0} (meV)								
	Default case σ_s = 0 meV	Low E_{ts} E_{ts} = 0.1 eV	High E_{ts} E_{ts} = 0.1 eV	Low Area A = A_{def}/10 cm^2	High Area A = A_{def}*2 cm^2	Low Voltage V=V_{def}/10	High Voltage V=V_{def}*10	Low m* m* = 0.1	High m* m* = 0.75
P2258C 12C	1026	1023	1025	910	1053	915	1105	879	1172
P2258C 12D	990	991	987	848	1018	855	1083	823	1172
P2258C 35	1054	1059	1050	912	1090	919	1169	881	1182
P2257 12C	1164	1169	1159	1123	1198	1038	1273	997	1214
P2257 12D	1093	1096	1090	1052	1126	966	1197	931	1204
P2254 12C	1194		1181	1156	1218	1199	1291	1018	1233
P2254 12D	1108	1107	1107	1072	1138	996	1121	958	1196
P1019D 12	656	644	658	667	652	667	639	656	655
P1019C 12	723	712	725	723	720	723	708	711	724
P1019B 12	888	891	886	840	926	843	978	827	920
P1019 08	1098	1105	1093	956	1135	962	1216	925	1185
P1019 32	841	848	840	801	850	803	866	788	872
P1019A 35	939	945	934	845	981	843	1056	824	1067
P972B 12	848	853	847	837	858	812	887	796	887
P972A 08	940	947	934	891	981	839	1062	822	1080
P972D 32	852	852	851	842	858	820	864	805	874
P972C 12	872	873	875	834	880	836	891	820	901
P972D 12	867	868	866	827	876	829	895	814	901
P972D 35	872	885	876	884	888	820	981	813	964
P991D 12	868	872	866	829	876	830	892	815	898
P991A 12	885	898	882	836	898	838	931	822	932
P991C 12	881	899	878	828	907	830	982	814	978
P991B 35	877	878	875	832	889	834	921	820	919
P991B 08	962	969	957	910	1003	839	1082	821	1125
P902 12	815	804	817	802	814	803	804	786	823
P902 08	1144		1140	1020	1176	1025	1247	979	1237
P902 35	1085	1088	1082	955	1119	961	1099	923	1170
P956 12	964	971	958	846	1005	849	1088	830	1147
P956 08	1031	1038	1026	882	1069	888	1149	858	1150
P956 35	939	945	934	838	938	863	1052	824	1064
Avg.	949	937	947	887	971	875	1018	846	1028
Std. Dev.	131	122	129	110	142	103	164	80	163

	Delta V_{b0} (meV)								
	Default case σ_s = 0 meV	Low E_{ts} E_{ts} = 0.1 eV	High E_{ts} E_{ts} = 0.1 eV	Low Area A = A_{def}/10 cm^2	High Area A = A_{def}*2 cm^2	Low Voltage V=V_{def}/10	High Voltage V=V_{def}*10	Low m* m* = 0.1	High m* m* = 0.75
Avg.	949	3	-3	-63	22	-74	68	-103	79
Std. Dev.	131	7	3	49	16	49	49	58	54

Table D.4 **Sensitivity of fitted E_{00}, to Cross-sectional area, voltage, effective mass, and grain boundary density of states using the two-step thermally-assisted tunneling model.**

Sample ID	E_{00} (meV)								
	Default case σ_s = 0 meV	Low E_{ts} E_{ts} = 0.1 eV	High E_{ts} E_{ts} = 0.1 eV	Low Area A = A_{def}/10 cm^2	High Area A = A_{def}*2 cm^2	Low Voltage V=V_{def}/10	High Voltage V=V_{def}*10	Low m* m* = 0.1	High m* m* = 0.75
P2258C 12C	23	24.2	22.5	20	23.6	20.2	24.6	19.1	23.8
P2258C 12D	19.8	21	19.3	15	20.5	15.3	22.1	14.2	23.3
P2258C 35	24.1	25	23.4	20.1	25	20.4	26.6	19.2	23.5
P2257 12C	25.5	27.1	24.7	24.6	26.2	22.5	27.7	21.6	23.2
P2257 12D	22.8	24.1	22.1	21.8	23.5	19.3	25	18.4	23.1
P2254 12C	27.3		26.1	26.5	27.5	30.2	28.8	23.3	23.7
P2254 12D	23.9	25.2	23.3	23.1	24.5	21.2	22.8	20.4	23.5
P1019D 12	7	8.5	6.8	9.5	6.3	9.4	5	9.2	5.8
P1019C 12	8.5	10.2	8.4	10.9	7.8	10.8	6.3	10.6	7.2
P1019B 12	11.8	12.5	11.5	12.7	13	12.6	14	12.3	11.3
P1019 08	23.7	25.2	22.9	19.7	24.6	19.9	26.3	18.9	22.9
P1019 32	11.4	14.3	11.1	12.6	11	12.6	9.9	12.2	10.8
P1019A 35	15	16.1	14.4	12.9	16.4	12.6	18.6	12.2	18.8
P972B 12	11.4	14.1	11.1	11.8	11.1	12.5	11.3	12.2	11.4
P972A 08	15.5	16.7	14.8	13.8	16.9	13	19.2	12.5	19.6
P972D 32	10.8	13.3	10.5	11.3	10.3	12.1	9	11.8	10
P972C 12	11.3	11.9	11	12.4	10.9	12.4	9.9	12.1	10.8
P972D 12	11.3	11.9	11	12.4	11	12.4	10.4	12.1	11
P972D 35	11.7	15	11.7	13.5	11.7	12.1	15	12.3	14.3
P991D 12	11.2	14	10.9	12.4	10.9	12.3	10	12	10.8
P991A 12	12	15.5	11.7	12.9	11.8	12.8	11.7	12.5	12.2
P991C 12	12.3	16.4	11.9	12.7	13	12.6	15.5	12.2	15.3
P991B 35	11.6	9.6	11.2	12.5	11.3	12.5	11.2	12.2	11.5
P991B 08	16.8	18	16.2	13.1	18.1	13.1	20.3	12.6	21.3
P902 12	10.3	12.5	10.1	12.3	9.7	12.3	8.1	12	9.2
P902 08	26.4		25.6	23.6	27.1	23.8	28.3	22.8	23.7
P902 35	23.9	25.3	23.2	20.5	24.6	20.7	22.5	19.7	23.2
P956 12	16.5	17.9	15.9	13.3	17.9	13.3	20.2	12.9	21.8
P956 08	20.6	22	19.9	15.8	21.6	16	23.5	15	22.2
P956 35	15.1	16.2	14.5	13.4	15.5	13.9	18.6	12.2	18.8
Avg.	16.4	17.3	15.9	15.6	16.8	15.5	17.4	14.7	17
Std. Dev.	6.1	5.5	5.9	4.7	6.6	4.8	7.3	4.0	6

	Delta E_{00} (meV)								
	Default case σ_s = 0 meV	Low E_{ts} E_{ts} = 0.1 eV	High E_{ts} E_{ts} = 0.1 eV	Low Area A = A_{def}/10 cm^2	High Area A = A_{def}*2 cm^2	Low Voltage V=V_{def}/10	High Voltage V=V_{def}*10	Low m* m* = 0.1	High m* m* = 0.75
Avg.	16.4	-0.4	-0.5	-0.8	0.3	-0.9	0.9	-1.6	0.4
Std. Dev.	6.1	7.4	0.3	2.3	0.7	2.4	2.1	2.6	2.3

These results demonstrate that the sample fits are not very sensitive to possible errors in the determination of the sample cross-sectional area (with the exception of samples with a known inhomogeneity throughout the thickness as discussed in section 5.5.1.1 and Appendix C). This is in contrast to capacitance techniques, which are very sensitive to the sample cross-sectional area. From equation (2.4) for the capacitance technique: $V_{b0} \propto A^{2}$ and $\sqrt{N_b} \propto A^{-1}$, when used for determining V_{b0} or N_b (recall $E_{00} \propto \sqrt{N_b}$).

The sensitivity to reducing the grain-boundary carrier capture coefficient by a factor of two for the one-step model has the same effect as reducing the cross-sectional area by a factor of two as given above. Here again, this is –32 meV or –3.7% for the 50% decrease in γ for V_{b0}, and -0.8 meV or -3.8% decrease in E_{00}. Thus, the grain-boundary carrier capture coefficient has only a small effect on the fitted parameters.

For the sensitivity to the order of magnitude decrease in voltage per grain boundary, the value of V_{b0} decreased by about –74 meV or –7.8% for the two-step thermally-assisted tunneling model, while the value of E_{00} decreased by -0.8 meV or -5.5%. For the one-step thermally-assisted tunneling model, a -85 meV or –9.8% decrease was observed for V_{b0}, and for E_{00} a decrease of –3.2 meV or -15% was observed. Thus, the one-step model is more sensitive to the order of magnitude decrease in voltage, however the sensitivity is minimal.

For the order of magnitude *increase* in voltage per grain boundary, the value of V_{b0} increased by about 68 meV or 7.2% for the two-step, while the value of E_{00} increased by 0.9 meV or 5.5%. For the one-step, a 109 meV or 12.5% increase was observed for V_{b0}, while E_{00} increased by 4.8 meV or 22.5%. Thus, except for E_{00} using the one-step thermally assisted tunneling model, the voltage per grain-boundary has only a small

effect on the fitted parameters. Here again, the sensitivity of the fitted parameters to the voltage per grain boundary is minimal when compared to the capacitance techniques. From equation (2.4) again for the capacitance technique: $V_{b0} \propto V$ or $\sqrt{N_b} \propto (V_{b0} - V)^{1/2}$, when used for determining V_{b0} or N_b (recall $E_{00} \propto \sqrt{N_b}$).

For the sensitivity to the increase in effective mass of holes to 0.75, the value of V_{b0} increased by about 79 meV or 8.3% for the two-step thermally-assisted tunneling model, while the value of E_{00} increased by 0.4 meV or 2.4%. For the one-step thermally-assisted tunneling model, a 17 meV or 2.0% increase was observed for V_{b0}, while for E_{00} a decrease of –0.7 meV or –3.3% was observed. For the decrease in effective mass of holes to 0.1, the value of V_{b0} decreased by about –103 meV or 10.9% for the two-step, while the value of E_{00} decreased by –1.6 meV or –9.8%. For the one-step, a decrease of -50 meV or –5.3% was observed for V_{b0}, while for E_{00} a decrease of –1.5 or –7.0% was observed. Here also, these sensitivity results indicate only a small dependence on the effective mass.

Finally, the effect of variable characteristic energies, E_{ta} and E_{td}, for the grain boundary density of states was evaluated for the two-step thermally-assisted tunneling fits. The value of E_{ta} was systematically varied from 0.4 to 0.1 in accordance with the values as measured by Thorpe for CdTe bicrystals.[23] It should be noted that there is no reason to expect these values to be the same for the processed polycrystalline samples herein, however they serve as a starting point for evaluating the sensitivity to these factors. The value for E_{td} was left as an additional fitting parameter. Interestingly, the fitted value of E_{td} was found to fall within the range of E_{td} values (0.05 – 0.3) as also measured by Thorpe. The net effect of this variation on V_{b0} was very small, much less than 1%

variation. The effect on E_{00} was also small with a 2.4% decrease in its value for low values of E_{td} and a 3% decrease for high values of E_{ta}. Thus, the main effect appears to be on E_{td} with little effect on V_{b0} or E_{00}.